UNLV | UNIVERSITY LIBRARIES

UNLV Retrospective Theses & Dissertations

1-1-1995

Transport properties along the channel of a Hemt

Narendra B Balakrishnan
University of Nevada, Las Vegas

Follow this and additional works at: https://digitalscholarship.unlv.edu/rtds

Repository Citation

Balakrishnan, Narendra B, "Transport properties along the channel of a Hemt" (1995). *UNLV Retrospective Theses & Dissertations*. 570.
http://dx.doi.org/10.25669/e6qv-pael

This Thesis is protected by copyright and/or related rights. It has been brought to you by Digital Scholarship@UNLV with permission from the rights-holder(s). You are free to use this Thesis in any way that is permitted by the copyright and related rights legislation that applies to your use. For other uses you need to obtain permission from the rights-holder(s) directly, unless additional rights are indicated by a Creative Commons license in the record and/or on the work itself.

This Thesis has been accepted for inclusion in UNLV Retrospective Theses & Dissertations by an authorized administrator of Digital Scholarship@UNLV. For more information, please contact digitalscholarship@unlv.edu.

INFORMATION TO USERS

This manuscript has been reproduced from the microfilm master. UMI films the text directly from the original or copy submitted. Thus, some thesis and dissertation copies are in typewriter face, while others may be from any type of computer printer.

The quality of this reproduction is dependent upon the quality of the copy submitted. Broken or indistinct print, colored or poor quality illustrations and photographs, print bleedthrough, substandard margins, and improper alignment can adversely affect reproduction.

In the unlikely event that the author did not send UMI a complete manuscript and there are missing pages, these will be noted. Also, if unauthorized copyright material had to be removed, a note will indicate the deletion.

Oversize materials (e.g., maps, drawings, charts) are reproduced by sectioning the original, beginning at the upper left-hand corner and continuing from left to right in equal sections with small overlaps. Each original is also photographed in one exposure and is included in reduced form at the back of the book.

Photographs included in the original manuscript have been reproduced xerographically in this copy. Higher quality 6" x 9" black and white photographic prints are available for any photographs or illustrations appearing in this copy for an additional charge. Contact UMI directly to order.

UMI

A Bell & Howell Information Company
300 North Zeeb Road, Ann Arbor MI 48106-1346 USA
313/761-4700 800/521-0600

TRANSPORT PROPERTIES ALONG THE CHANNEL OF A HEMT

by

Narendra B. Balakrishnan

Director: R. Venkatasubramanian, Ph.D

A thesis submitted in partial fulfillment

of the requirements for the degree of

Máster of Science

in

Electrical and Computer Engineering

Department of Electrical and Computer Engineering

University of Nevada, Las Vegas

May, 1996

UMI Number: 1380494

UMI Microform 1380494
Copyright 1996, by UMI Company. All rights reserved.

This microform edition is protected against unauthorized copying under Title 17, United States Code.

UMI
300 North Zeeb Road
Ann Arbor, MI 48103

The thesis of Narendra B. Balakrishnan for the degree of Master of Science in Electrical and Computer Engineering is approved.

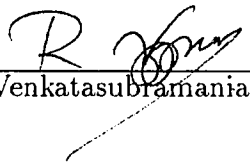

Chairperson, R. Venkatasubramanian, Ph.D

Examining Committee Member, Robert Schill, Ph.D

Examining Committee Member, Ashok Iyer, Ph.D

Graduate Faculty Representative, Tao Pang, Ph.D

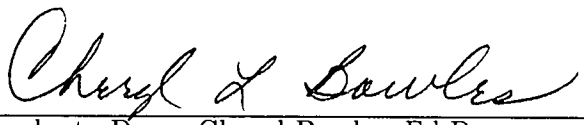

Interim Graduate Dean, Cheryl Bowles, Ed.D

University of Nevada, Las Vegas

May, 1996

ABSTRACT

In the theoretical modeling of a high electron mobility transistor (HEMT), it is inherently assumed that the variation of quantum confinement along the channel from the source to the drain is about the same and therefore, the transport properties are independent of position and only dependent on the electric field along the channel. In this study, the scattering rates for polar optical phonons (POP), acoustic phonons (AP) through deformation potential and impurity scattering are obtained theoretically based on the Fermi's golden rule as a function of position along the channel for an $Al_{0.37}Ga_{0.63}As/GaAs$ HEMT. It is observed that the POP mechanism exhibits a maximum variation of 114% in the scattering rates for both intrasubband and intersubband scattering mechanisms due to varying degrees of quantum confinement from the source to the drain. The AP mechanism shows a maximum variation of 109% and the scattering rate due to impurity scattering presents a maximum variation of 133%. If these wide variations in the scattering rates are not accounted for, in the transport parameter calculation, it will introduce an error in the I-V characteristics, irrespective of the type of device modeling.

ACKNOWLEDGMENTS

I am very grateful to my advisor, Dr. Rama Venkat for his guidance throughout this work. I would like to thank Dr. Tao Pang and Dr. Ashok Iyer for clarifying many a subject material. My thanks are also due to Dr. Robert Schill and Dr. Tao Pang for serving on my thesis committee and to all other professors under whom I studied. I am very thankful to my countless Indian friends and to my dear American friends, Joseph O'Day, Eric Anderson, Sam Suleiman, Jay Nietling, Kerry Rogers, Gideon Wober, Doug Blair, Jim Kelly and Albert Chin-A-Young for help received on innumerous occasions, and to Meera Rani, Divya Sundaram, Giray Pultar and Gennady Podolsky for their constant support and encouragement.

Contents

List of Figures

List of Tables

Chapter 1

INTRODUCTION

1.1 HEMT description

The high electron mobility transistor (HEMT), a heterostructure field effect transistor, has attracted considerable attention among device physicists due to its many advantages over conventional FETs such as excellent microwave and millimeter wave characteristics (i-e.) high gain at high frequencies and also excellent low noise characteristics. Juxtaposing an $n - AlGaAs$ layer and an undoped $GaAs$ layer, creates a conduction band edge energy level lower than the energies observed on either the $n - AlGaAs$ or the undoped $GaAs$ and this allows the conduction electrons of the $n - AlGaAs$ to move to the undoped $GaAs$ side and reside at the heterojunction interface. HEMTs derive their superior transport properties (high mobility and velocity) from the electrons that occupy the quantum well of the undoped semiconductor material.

A cross-sectional view of a conventional HEMT is shown in Figure 1.1. The source and drain contacts are ohmic, whereas the gate is a Schottky barrier. In Figure 1.1, a wide band gap semiconductor material doped n- type ($n - AlGaAs$) lies on an undoped

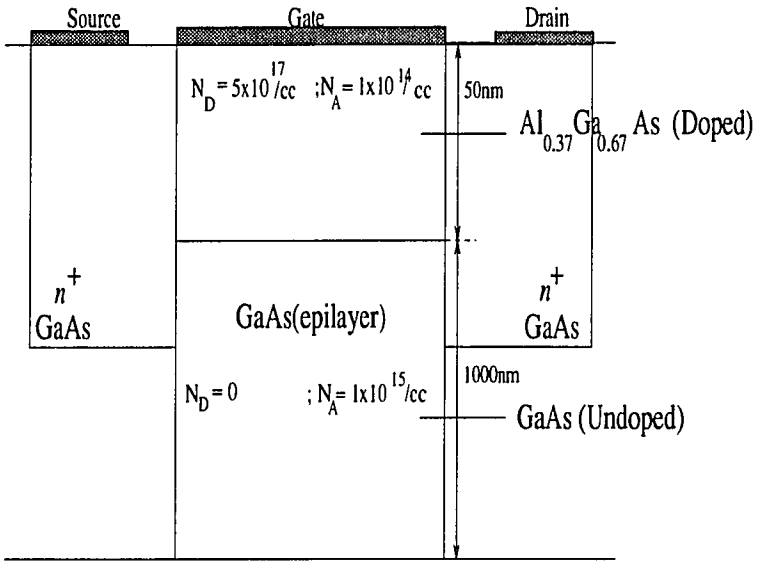

Figure 1.1: A schematic picture of a conventional HEMT device structure.

narrow band gap material ($GaAs$). A conduction band edge discontinuity occurs along the $n - AlGaAs/GaAs$ interface. This results in the electron transfer from the $n - AlGaAs$ side to the $GaAs$ side and hence a high electron concentration in a narrow region along the $GaAs$ side of the heterojunction. Because the electrons are confined along one dimension, the carriers are referred to as the two-dimensional electron gas (2-DEG) and the 2-DEG is quantified in terms of a sheet carrier density. These 2-DEG electrons traveling in this thin region do not encounter ionized donor atoms because they are now resident on the undoped $GaAs$ side. Such 2-DEG electrons in $GaAs$ side show very high mobility, due to less impurity scattering and are responsible for fast response times and high frequency operation.

The heavily doped, low resistance source and drain wells serve to make contact with the 2-DEG. The highly doped $GaAs$ present on the surface of the $n - AlGaAs$ serves to reduce the ohmic resistance of the source and drain contacts. For low drain to source voltages, a current flows from the drain to the source through the 2-DEG. In depletion mode

devices, even in the absence of an applied gate bias, a drain current flows, proportional to the applied drain to source voltage. The electron velocity and the current saturates with increase in the drain to source voltage. The 2-DEG density which determines the saturated current, is controlled by the gate bias. By applying a large negative gate bias, the depth of the quantum well at the interface can be decreased. For depletion mode devices, this reduces the sheet carrier density and hence the current conduction. For enhancement mode devices, no current conduction takes place until forward bias is applied.

Normally a spacer layer, an undoped $AlGaAs$ layer, placed between the $n-AlGaAs$ and the undoped $GaAs$ helps to separate the electrons flowing in the 2-DEG from the dopant ions in the $n-AlGaAs$ side as shown in Figure 4.1. Without such a layer, electrons residing in the interface are subjected to scattering, which reduces the electron mobility. This is undesirable, for it defeats the very purpose of our striving, to isolate the carriers at the interface, and take advantage of 2-DEG, devoid of impurity scattering.

1.2 Phonons and the scattering potential

The vibration of atoms within a lattice distort the periodicity of the crystal structure and cause small shifts in the energy bands commonly called gratings. Deviations of the bands due to these small shifts from the frozen lattice positions lead to an additional potential which causes the scattering of carriers such as electrons and holes. We treat the so called scattering potential or the deformation potential for specific cases (the term scattering potential is a general descriptor for deformation potential due to different mechanisms) by time dependent first order perturbation theory to evaluate the rate at which electrons are scattered out of an initial state $\overline{k}$ into another final state $\overline{k'}$ by either absorbing or emitting

a phonon of wave vector $\overline{q}$.

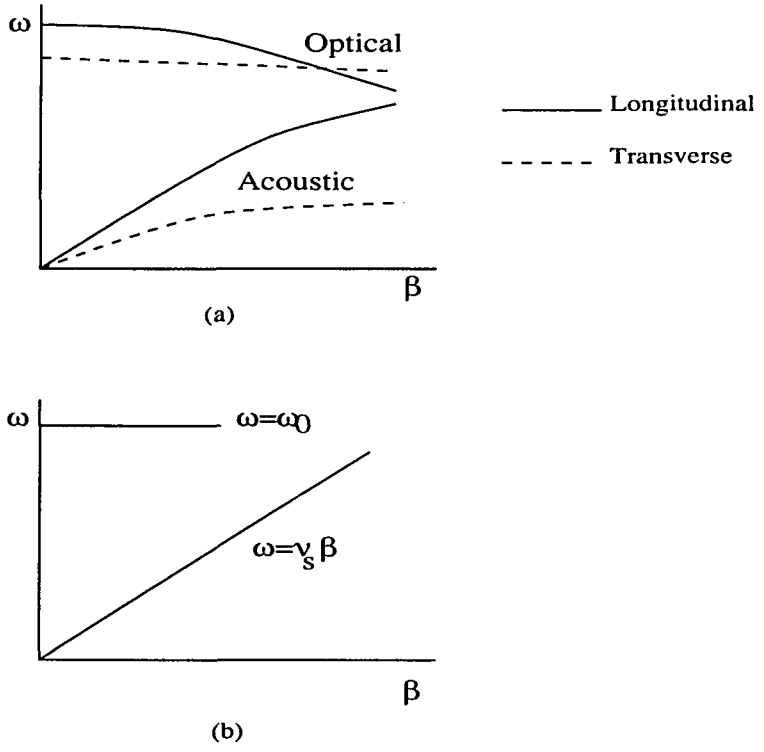

Figure 1.2: (a)Dispersion relation for lattice waves propagating along a high symmetry direction in semiconductors. (b)simplified dispersion relations

Because of thermal energy, the atoms within a crystal are constantly under oscillation about their equilibrium position. These oscillations are called lattice waves and have properties very similar to those of the Bloch waves. The frequency ω versus wave vector β dispersion plot for the six types of elastic waves that exist (three acoustic modes and three optical modes and out of each of these three, one is longitudinal (LA) and two are transverse (TA)) has been shown in Figure 1.2. Acoustic modes are like sound waves because the adjacent atoms are displaced in the same direction (only the amount of displacement varies from atom to atom). Optical modes displace adjacent atoms out of phase. The term "op-

tical" comes in the observable context of lattice vibrations interacting strongly with visible light. Atoms give rise to long-range macroscopic electric fields in addition to deformation potentials and the interaction of the electron with these fields produces additional components of scattering. Polar optical phonon scattering is indeed the dominant mechanism of scattering in pure III-VI and II-VI compounds. The major scattering mechanism in polar materials at room temperature is longitudinal optical scattering.

In reality however, the 2-DEG electrons in our HEMT structure are susceptible to polar optical phonons (POP) and acoustic phonons (AP), and to a limited extent, the ionized impurity scattering in the $AlGaAs$.

1.3 Overview of the thesis

The theoretical modeling of HEMTs fall into three categories: charge control models [13, 20], Monte Carlo approach [28, 1], and self consistent numerical solution to BTE-Poisson equations [15]. Some of these approaches require the knowledge of transport properties such as mobilities, diffusion coefficients, dissipation factor, collision, momentum relaxation and energy relaxation times. Many of these parameters are usually obtained from a combination of scattering rate calculations including the dominant scattering processes [18] and a Monte Carlo procedure [28, 1]. In the past, theoretical models inherently neglected the variation of the transport properties along the channel [28, 1, 15]. However, there are studies reported in the literature [2, 10, 12, 5] which unambiguously indicate that the scattering rate for POP depends on the effective well width. But, the theoretical works presented in [2, 10] assume an infinite rectangular potential well for their analysis. The purpose of this work is to analyze the variation of transport properties using HEMT conduction band edge profiles,

E_c, at various channel locations. These variations in E_c profiles are a result of asymmetric gate to channel potential from the source to the drain.

The scattering rates for polar optical phonons (POP) and acoustic phonons via deformation potential (AP) and impurity scattering have been studied as a function of position along the channel for a $Al_{0.37}Ga_{0.63}As/GaAs$ HEMT. The Poisson solver employed to obtain the one-dimensional (1-D) conduction band profiles at different points along the channel from the source to the drain is discussed. The energy Eigen values and their respective wave functions are obtained for each conduction band profiles by solving the time independent Schrödinger's equation by the Numerov method [3]. The two-dimensional (2-D) scattering rates for POP and AP (via deformation potential) are obtained based on the Fermi's golden rule.

A brief literature survey of HEMT and its modeling is presented in Chapter 2. The theoretical formulation of scattering rates based on the Fermi's golden rule is presented in Chapter 3. The computational procedure for obtaining E_c profiles (from gate to substrate) for various locations along the channel is discussed in Chapter 4. Results of various intrasubband and intersubband scattering mechanisms for three channel locations are also presented and discussed in Chapter 4. The thesis is concluded in Chapter 5.

Chapter 2

LITERATURE SURVEY

The HEMT, otherwise referred to as the Two-dimensional Elecron Gas Field Effect Transistor (TEGFET), Heterostructure FET (HFET), Selectively Doped Heterostructure Transistor (SDHT) or Modulation Doped FET (MODFET), at millimetric frequencies, provides a lower noise figure (in dB) than gain (also expressed in dB) and hence, is very well suited for millimeter wave integration. At lower frequencies, for example in the X and J bands, the HEMT currently finds application mainly as a discrete device in low noise hybrid amplifiers.

Although HEMTs attracted a lot of attention in the 1980s for computer applications, because of the high expense involved in its manufacture and because such devices were only a factor of 3 faster than the transistors made using Si technology (the leading computer manufacturers in the market, realized that such high speeds of operation can be achieved using RISC technology or parallel computers), the interest in these devices has waned down perceptibly. The focus is now on heterostructure optoelectronic and integrated optical devices for telecommunications. Thus for the fabrication of microwave and millimeter wave HEMTs, a conventional HEMT (with a doped $AlGaAs$, an undoped spacer and the active

GaAs layer) utilizes an additional thin layer of undoped *InGaAs*. Such strained layer or pseudomorphic *InGaAs* HEMTs demonstrate state-of-the-art millimeter-wave power performance with commendable power amplification at ultra high frequencies.

In literature, there are a number of analytical and numerical models that attempt to explain the operation of HEMTs. In some of the early linear charge control models [4, 13], a constant correction distance of the 2-DEG layer from the heterointerface is assumed. In more recent models, however, this distance which represents the quantum well width has been taken into consideration. Wang and Hess [25] reasoned that while the drift-diffusion model may be favorable for describing the overall features of the HEMT, Boltzmann transport equation is necessary to characterize the nonstationary phenomena that could be observed close to the drain, due to high electric fields. They analyzed the electron velocity distribution, hot electron effects, nonstationary effects and real space transfer (transfer of electrons over the interface barrier and into the doped *AlGaAs* layer) at high electric fields in the conducting channel of an idealized HEMT structure by using a many-particle ensemble 3-D Monte Carlo method and a self-consistent 2-D solution of the Poisson's equation.

Tomizawa et al [24] analyzed 2-DEG behavior in an *AlGaAs/GaAs* heterostructure FET using Monte Carlo method. They assumed that in the channel region, the electrons are subjected to a 2-D scattering process and hence introduced 2-D scattering rates for the induced electron gas at the heterointerface.

Park et al [16] provided the first precise comparison between theoretical analysis and experiment of the performance of a 0.35-μm pseudo-morphic $Al_{0.15}Ga_{0.85}As/In_{0.15}Ga_{0.85}As$ HEMT. Their calculations which took into account the real space transfer, full details of the 2-DEG, velocity overshoot, ballistic transport, and the effects of the 2-D electric field

profile, were made using an ensemble Monte Carlo technique. They observed that near the source, the 2-D system dominated the transport physics whereas near the pinch-off point, real space transfer manifested itself. They also determined that the pseudomorphic HEMT provided high speeds because of the high electron confinement within the 2-D system near the source as well as the high electron mobility and confinement within the gamma valley in the bulk $InGaAs$.

Yokoyama and Hess [28] studied the electronic transport in $Al_{1-x}Ga_xAs/GaAs$ single-well structures. The electronic states of the quantum well were calculated self-consistently taking the five lowest subbands into account and the numerically obtained wave functions and Eigen values were used to obtain the polar optical phonon and acoustic phonon 2-D scattering rates.

Price [17], Walukiewicz et al [26], have employed a two subband triangular well approximation for the quantum well. Walukiewicz et al provided a model for electron mobility in such a 2-DEG confined in a triangular well where, all major scattering processes such as polar optical, acoutic phonon through deformation potential, piezoelectric, ionized impurity and alloy disorder (for an $In_{0.53}Ga_{0.47}As$ based heterostructure) were included, as well as intrasubband and intersubband scattering. Their research showed that maximum channel conductivity was achieved for heterostructrues with very large spacer widths.

Tomizawa et al [23] presented a Monte Carlo method for a heterostructure MIS-like FET as well as for a submicrometer gate $AlGaAs/GaAs$ heterostructure MIS-like FET's with various gate lengths and thicknesses of the $AlGaAs$ undoped layer. Their model employed wave functions for the first three subbands for determining the electron transport. It was observed that the electric potential in the channel of the MIS-like FET substan-

tially affected the potential of the gate, and showed a nonuniform high electric field to be present in the submicrometer channel (resulting in nonstationary and hot-electron transport). Yokoyama and Hess [28] used the first five lowest subbands to evaluate transport properties.

Shey et al [20] provided a simple charge control model of the 2-DEG, taking into account the effective distance of the 2-DEG from the heterointerface. They derived a simple yet accurate expression for Fermi energy, derived from a triangular potential well approximation and their work showed the inaccuracy of previous linear charge control models, wherein the variation of the Fermi potential with the gate bias had been neglected.

The second type of modeling involves using 2-D numerical models in which the Boltzmann transport and Poisson equations are solved numerically. Widiger et al, [27] by assuming that the electric field in the quantum well is a constant and that the electrons reside right at the heterojunction, have attempted to use the hydro-dynamic-like transport equations, which include the two higher moments of the Boltzmann equation. Their model included both the hot-electron effects and conduction outside the quantum subband system and they showed that the hot-electron effects are of considerable importance for the HEMT operation. They found that at the pinchoff point, velocity overshoot, high electron energies and real space transfer are significant and that these effects are less pronounced at the source.

Several self-consistent models have also been proposed. Yokoyama and Hess [28] and Stern and Das Sharma [21] have calculated the electron states in the quantum well by trying to solve the Schrödinger's and Poisson's equations consistently.

Ng et al [15] have extended Widiger's work to include the spatial spreading of the

electron concentration of the 2-DEG in the quantum well normal to the heterojunction by means of a self-consistent treatment of Schrödinger's and Poisson's equations. Their model is capable of predicting the Eigen functions and Eigen values of the higher subbands.

Chapter 3

SCATTERING THEORY

3.1 Introduction

The Schrödinger's equation, which is the basis of quantum physics and which is useful for studying the dynamics of elementary particles such as electrons, is given by [14]:

$$i\hbar\frac{\partial\Psi(r,t)}{\partial t} = -\frac{\hbar^2}{2m_0}\nabla^2\Psi(r,t) + [V(r) + U_C(r) + U_S(r,t)]\Psi(r,t) \tag{3.1}$$

where $V(r)$ is the potential energy applied to or built in the device under consideration, $U_C(r)$ is the crystal potential energy (due to electrostatic potential experienced, by the carriers due to the presence of atoms), $U_S(r,t)$ is the scattering potential energy because of the presence of ionized impurities or lattice vibrations which give rise to polar optical phonon and acoustic phonon scattering mechanisms, $\hbar$ is the Planck's constant divided by 2π, m_0 is the electron's rest mass. Ψ is the wave function, a parameter invented to describe the wave nature of electrons (or any particle under consideration). Ψ is a complex quantity with some magnitude and phase factor. $\Psi\Psi^* dr$ is the probability of finding the electron in

the infinitesimally small interval dr between r and $r+dr$, where Ψ^* is the complex conjugate of Ψ. Thus, if we introduce an electron in a device, there must be a finite probability of locating that electron within that device. This idea is explained by Max Born's equation that $\int_{-\infty}^{+\infty} \Psi\Psi^* dr = 1$.

The crystal potential energy $U_C(r)$ can be "absorbed" into the mass and an effective mass, instead of the rest mass can be used. Thus the new wave equation can be written as

$$[H_0 + U_S(r,t)]\Psi(r,t) = i\hbar\frac{\partial\Psi(z,t)}{\partial t} \tag{3.2}$$

where H_0 is the Hamiltonian operator, an operator for the problem without a scattering potential. In other words, H_0 is the operator for the "unperturbed" problem, an Eigen value problem.

This Eigen value problem can be described by the equation $H_0\Psi_{\overline{k}} = E(\overline{k})\Psi_{\overline{k}}$ where $E(\overline{k})$ refers to the Eigen values. The solution to this problem is obtained by the method of separation of variables and we can easily show that the wave function solution would be of the form:

$$\Psi^0_{\overline{k}}(z,t) = \Psi_{\overline{k}}(z)e^{-\frac{iE(\overline{k})t}{\hbar}} \tag{3.3}$$

For the problem which we need to solve including the scattering potential $U_S(z,t)$, the solution does not look very different from the solution for the perturbed case. Expressing the solution for the case including the scattering potential, as a linear combination of the solution for the unperturbed case, we get

$$\Psi(z,t) = \sum_{\overline{k}} C_{\overline{k}}(t)\Psi^0_{\overline{k}}(z,t) = \sum_{\overline{k}} C_{\overline{k}}(t)\Psi_{\overline{k}}(z)e^{-\frac{iE(\overline{k})t}{\hbar}} \tag{3.4}$$

3.2 Definition of scattering rate

Let an electron wave packet centered at $\overline{k} = \overline{k_0}$ (or average momentum of $\hbar\overline{k_0}$ be scattered to a final state with an average wave vector centered at $\overline{k} = \overline{k_0'}$ (or average momentum of $\hbar\overline{k_0'}$, by a scattering potential $U_S(z,t)$. At $t = 0$, $C_{\overline{k_0}}(t = 0) = 1$ and $C_{\overline{k}}(t = 0) = 0$ for all $\overline{k}$ not equal to $\overline{k_0}$. The probability of finding the electron with wave vector $\overline{k_0'}$ is

$$P(\overline{k} = \overline{k_0'}) = \lim_{t\to\infty} |C_{\overline{k_0'}}(t)|^2 \tag{3.5}$$

The above equation was obtained as follows: We remember from equation (3.4) that $\Psi(z,t)$ is of the form, some magnitude times some phase (described by $e^{-\frac{iE(\overline{k})t}{\hbar}}$). To find the probability, we use Born's equation which basically amounts to integrating $C_{\overline{k}}\Psi_{\overline{k}}$ and its conjugate $C^*_{\overline{k}}\Psi^*_{\overline{k}}$ over z, yielding the above expression.

The transition rate from $\overline{k_0}$ to $\overline{k_0'}$ is then given by

$$S(\overline{k_0}, \overline{k_0'}) = \lim_{t\to\infty} \frac{|C_{\overline{k_0'}}(t)|^2}{t} \tag{3.6}$$

This is the definition of scattering rate due to a scattering potential $U_S(z,t)$.

To find the linear constants $C_{\overline{k}}$, we substitute equation (3.4) into equation (3.2) to get

$$U_S(z,t)\sum_{\overline{k}} C_{\overline{k}}(t)\Psi_{\overline{k}}e^{-\frac{iE(\overline{k})t}{\hbar}} = i\hbar\sum_{\overline{k}} \frac{\partial C_{\overline{k}}}{\partial t}\Psi_{\overline{k}}e^{-\frac{iE(\overline{k})t}{\hbar}} \tag{3.7}$$

because

$$H_0\Psi(z,t) = i\hbar[\frac{E}{i\hbar}\sum_{\overline{k}} C_{\overline{k}}(t)\Psi_{\overline{k}}(z)e^{-\frac{iE(\overline{k})t}{\hbar}}]$$

$$= E\Psi(z,t)$$

Multiplying both sides of equation (3.7) with $\Psi^*_{\overline{k_0'}}e^{\frac{iE(\overline{k_0'})t}{\hbar}}$, we get

$$U_S(z,t)\sum_{\overline{k}} C_{\overline{k}}(t)\Psi_{\overline{k}}\Psi^*_{\overline{k_0'}}e^{-i\frac{[E(\overline{k})-E(\overline{k_0'})]t}{\hbar}} = i\hbar\sum_{\overline{k}}\frac{\partial C_{\overline{k}}}{\partial t}\Psi_{\overline{k}}\Psi^*_{\overline{k_0'}}e^{-i\frac{[E(\overline{k})-E(\overline{k_0'})]t}{\hbar}} \tag{3.8}$$

Integrating with respect to z, we get,

$$i\hbar\frac{\partial C_{\overline{k_0'}}}{\partial t} = \sum_{\overline{k}} H_{\overline{k_0'}\overline{k}}C_{\overline{k}}(t)e^{i\frac{[E(\overline{k_0'})-E(\overline{k})]t}{\hbar}} \tag{3.9}$$

where

$$H_{\overline{k_0'}\overline{k}} = \int_{-\infty}^{+\infty}\Psi^*_{\overline{k_0'}}(z)U_S(z,t)\Psi_{\overline{k}}(z)dz \tag{3.10}$$

is called the matrix element of the scattering potential between states $\overline{k}$ and $\overline{k_0'}$. If we assume that the scattering is weak, we take into consideration only the $C_{\overline{k_0}} = 1$ term for all time and that all other $C_{\overline{k}}$'s are small. This Born approximation makes us write equation (3.9) as:

$$i\hbar\frac{\partial C_{\overline{k_0'}}}{\partial t} = H_{\overline{k_0'}\overline{k_0}}e^{i\frac{[E(\overline{k_0'})-E(\overline{k_0})]t}{\hbar}} \tag{3.11}$$

which can be integrated to find

$$C_{\overline{k_0'}}(t) = \frac{1}{i\hbar}\int_0^t H_{\overline{k_0'}\overline{k_0}} e^{i\frac{[E(\overline{k_0'})-E(\overline{k_0})]t}{\hbar}} dt + C_{\overline{k_0'}}(0) \tag{3.12}$$

Because the final state $\overline{k_0'}$ was empty at $t = 0$, $C_{\overline{k_0'}}(0)=0$. It can be seen from equation (3.12), that the matrix element does not have time dependency. A time dependent matrix element would be of the form:

$$H_{\overline{k_0'}\overline{k_0}}(t) = H^{a,e}_{\overline{k_0'}\overline{k_0}}(w) e^{\mp i\omega t} \tag{3.13}$$

The 'a' and 'e' refer to absorption and emission of a phonon. Using equation (3.13) in equation (3.10), we get

$$C_{\overline{k_0'}} = \frac{1}{i\hbar} H^{a,e}_{\overline{k_0'}\overline{k_0}}(\omega) \left[\frac{e^{\frac{i[E(\overline{k_0'})-E(\overline{k_0})\mp\hbar\omega]t}{\hbar}}}{\frac{i[E(\overline{k_0'})-E(\overline{k_0})\mp\hbar\omega]}{\hbar}} - 1 \right] \tag{3.14}$$

Let $\Omega = [E(\overline{k_0'}) - E(\overline{k_0}) \mp \hbar\omega]/\hbar$. Then, the above equation can be written as

$$C_{\overline{k_0'}} = \frac{1}{i\hbar} H^{a,e}_{\overline{k_0'}\overline{k_0}} e^{\frac{i\Omega t}{2}} \left[\frac{sin(\frac{\Omega t}{2})}{\frac{\Omega t}{2}} \right] t \tag{3.15}$$

Using the above equation (3.15) and equation (3.6) we can find out the scattering rate to be

$$S(\overline{k_0}, \overline{k_0'}) = \lim_{t\to\infty} \frac{|H^{a,e}_{\overline{k_0'}\overline{k_0}}|^2}{t\hbar^2} \left[\frac{sin(\frac{\Omega t}{2})}{\frac{\Omega t}{2}} \right]^2 t^2 \tag{3.16}$$

For very large values of t, the sinc function is very sharply peaked near the origin and looks like a delta function. The strength of the delta function found from the area under the

curve is

$$\int_{-\infty}^{\infty} \left[\frac{sin(\frac{\Omega t}{2})}{\frac{\Omega t}{2}}\right]^2 d\Omega = \frac{2\pi\hbar}{t} \tag{3.17}$$

Substituting equation (3.17) in equation (3.16) gives

$$S(\overline{k_0}, \overline{k_0'}) = \frac{2\pi}{\hbar}|H^a_{\overline{k_0'}\overline{k_0}}|^2\delta[E(\overline{k_0'}) - E(\overline{k_0}) - \hbar\omega] + \frac{2\pi}{\hbar}|H^e_{\overline{k_0'}\overline{k_0}}|^2\delta[E(\overline{k_0'}) - E(\overline{k_0}) + \hbar\omega] \tag{3.18}$$

The delta function in the above equation actually stands for the conservation of energy and applies when the scattering is weak (so that time can approach infinity). When $E(\overline{k_0'}) = E(\overline{k_0}) + \hbar\omega$, an energy of $\hbar\omega$, representing phonon energy, has been absorbed. When $E(\overline{k_0'}) = E(\overline{k_0}) - \hbar\omega$, an energy of $\hbar\omega$ has been emitted. Thus the 'a' and 'e' stand for the absorption and emission processes. The above equation is referred to as the 'Fermi's golden rule'. Thus to apply the golden rule to a scattering problem, the scattering potential must first be quantified so that the matrix element can be evaluated, and this can be used to determine the scattering rate.

3.3 Scattering by polar optical phonons

The scattering potential due to POP can be shown to be:

$$U_{POP} = \frac{qq^*u}{i\beta V_u\epsilon_0} \tag{3.19}$$

where, q^* is the effective charge on the dipole, β is the wave vector of the phonon, V_u is the volume of the unit cell under consideration to describe the POP mechanism, u is the displacement, the separation of two equal and opposite charges, ϵ_0 is the permittivity of

free space.

If κ_0 is the low frequency dielectric constant and κ_∞ is the high frequency dielectric constant, then the strength of the polar interaction by low and high frequency dielectric constants can be measured and can be shown to be:

$$(\frac{q^*}{V_u})^2 = \frac{\epsilon_0 \rho \omega_0^2}{\kappa_0}[\frac{\kappa_0}{\kappa_\infty} - 1] \tag{3.20}$$

At low frequencies, the dielectric constant includes a contribution due to the dipole between atoms but at high frequencies, this dipole cannot respond to the signal and hence κ_∞ is less than κ_0. The factor $[\frac{\kappa_0}{\kappa_\infty} - 1]$ is a measure of the strength of the dipole. In the equation (3.20), ρ is the density and ω_0 is the frequency of the POP in radians.

Now that $U_{POP}(z,t)$ is known, one can use equation (3.10) to find $H_{\overline{k_0'}\overline{k}}$ for POP, using $\Psi_{\overline{k}}(z)$ and $\Psi^*_{\overline{k_0'}}(z)$ which are the wave function and its conjugate, obtained as a solution to Schrödinger's equation with $U_{POP}(z,t)$.

For the 3-D case, if N(Q) is the number of phonons, $|H_{\overline{k_0'}\overline{k}}|^2$ or equivalently $|H_{\overline{p'}\overline{p}}|^2$ is given by:

$$|H_{\overline{p'}\overline{p}}|^2 = \frac{q^2 \omega_0 \hbar}{2\kappa_0 \epsilon_0 \beta^2 \Omega}(\frac{\kappa_0}{\kappa_\infty} - 1)(N(Q) + \frac{1}{2} \mp \frac{1}{2})\delta(\overline{p'} - \overline{p} \mp \hbar\beta) \tag{3.21}$$

Using Equation (3.21), the 3-D scattering rate given by the Fermi's golden rule is:

$$S(\overline{p}, \overline{p'}) = \frac{\pi q^2 \omega_0}{\kappa_0 \epsilon_0 \beta^2 \Omega}(\frac{\kappa_0}{\kappa_\infty} - 1)(N(Q) + \frac{1}{2} \mp \frac{1}{2})\delta(\overline{p'} - \overline{p} \mp \hbar\beta)\delta(E' - E \mp \hbar\omega_0) \tag{3.22}$$

where Ω is the volume over which $|H_{\overline{p'}\overline{p}}|^2$ and $S(\overline{p}, \overline{p'})$ are evaluated. It is noted that the

scattering rate, essentially represents the scattering rate per unit volume.

3.3.1 From 3-D to 2-D

The 3-D matrix element using the plane wave solution (exponentials) and the POP scattering is given as [28]:

$$H_{3D}{}_{(\overline{k_0'},\overline{k_0})} = \int_x \int_y \int_z (e^{-ik_x'x} e^{-ik_y'y} e^{-ik_z'z}) U_{POP}(z,t) (e^{+ik_x x} e^{+ik_y y} e^{+ik_z z}) dx dy dz \qquad (3.23)$$

where $\overline{k_0} = \bar{i}k_x + \bar{j}k_y + \bar{k}k_z$ is the initial wave vector before scattering and $\overline{k_0'} = \bar{i}k_x' + \bar{j}k_y' + \bar{k}k_z'$ is the final wave vector after scattering.

But for the 2-D case, as observed in a HEMT, one dimension for the carrier is confined. For the confined case, (say a rectangular well of width a, with either sides at infinite potential, the wave function solution along the confined direction is of the form $Asin(\frac{n\pi z}{a})$, where A is a constant.

Hence for the general 2-D case, the matrix element can be shown to be obtained from the relation:

$$H_{2D}{}_{(\overline{k'},\overline{k})} = \int_x \int_y \int_z (F_m(z) e^{-ik_x'x} e^{-ik_y'y}) U_{POP}(z,t) (F_n(z) e^{+ik_x x} e^{+ik_y y}) dx dy dz \qquad (3.24)$$

where $F_m(z)$ and $F_n(z)$ replace $Asin\frac{n\pi z}{a}$, in the general case of arbitrary potential variation.

If $\overline{k_0}$ and $\overline{k_0'}$ are the initial and final wave vectors for the electron and if $\mathbf{Q} = \pm(\overline{k_0} - \overline{k_0'})$ with $Q = |\mathbf{Q}|$ and q are the phonon wave-vector components parallel and

perpendicular to the layer interfaces, respectively, the scattering rate for the 2-D case for POP, can then be shown to be:

$$S_{mn}^{POP} = \frac{q^2\omega_0}{8\pi\epsilon_0}\left[\frac{1}{\epsilon_\infty} - \frac{1}{\epsilon_s}\right](N(Q) + \frac{1}{2} \pm \frac{1}{2})\int \frac{H_{mn}(Q)}{Q}\delta(E(\overline{k_0'}) - E(\overline{k_0}) \pm \hbar\omega_0)d\overline{k_0'} \quad (3.25)$$

with

$$N(Q) = \left[exp\left[\frac{\hbar\omega_0}{k_B T}\right] - 1\right]^{-1} \quad (3.26)$$

where ϵ_∞ and ϵ_s are the optical and static dielectric constants, respectively, $N(Q)$ represents the number of phonons, $\hbar\omega_0$ is the polar optical phonon energy and T is the temperature in ^{o}K. $H_{mn}(Q)$ represents the multisubband coupling coefficients and is given by [28]:

$$H_{mn}(Q) = \int\int dz_1 dz_2 F_{mn}(z_1)F_{mn}(z_2)exp(-Q|z_1 - z_2|) \quad (3.27)$$

with $Q = |\mathbf{Q}|$. In equation (4.9), $F_{mn}(z) = F_m(z)F_n(z)$ where $F_m(z)$ is the wave function of the m^{th} subband.

3.4 Scattering by acoustic phonons

The interaction potential for acoustic phonons (AP) is given by [1]:

$$U_{AP}(z,t) = D_A\frac{\partial u}{\partial z} \quad (3.28)$$

where, u is the displacement, D_A is the deformation potential due to AP and can be found from experiments.

Using a similar procedure outlined for POP in section 3.3, one can find the matrix element for AP and use this matrix element to evaluate the scattering rate for the 2-D case.

AP mechanism is elastic due to the phonons' low energy. In other words, acoustic phonons do not scatter electrons from one subband to another, but scatters them within the subbands. This is because, the acoustic phonons do not impart much energy or momentum to the electrons which they scatter, to change the electrons' final energy and momentum considerably. If the energy of the incident electrons is high, these phonons merely help to deflect them. At low energies, this scattering mechanism becomes significant.

The intrasubband scattering rate for AP (via deformation potential) for the m^{th} subband for an electron with initial wave vector, $\overline{k_0}$, is given by [1]

$$S_{mm}^{AP} = \frac{D^2}{4\pi\rho S_l} \int F_m^4(z)dz \int d^2QQ \frac{\left[N(Q) + \frac{1}{2} \pm \frac{1}{2}\right]}{\epsilon^2(Q)} \delta(E(\overline{k_0}) - E(\overline{k_0'}) \pm \hbar S_l Q) \qquad (3.29)$$

where D is the deformation potential, ρ is the density of the $GaAs$, S_l is the longitudinal sound velocity in $GaAs$ and $\epsilon(Q)$ is the screening function as defined in [1]. The material constants are listed in Table II and the temperature is assumed as 300°K.

3.5 Impurity scattering

If an impurity atom were to be present in the structure either, in the active layer $GaAs$ or in the $AlGaAs$, it exerts an influence on the charges in the accumulation layer, which redistribute themselves depending upon the potential energy of the impurity atom. The carrier concentration in the accumulation layer would increase if the potential energy of the impurity is lowered and carrier concentration would decrease if the potential energy is

increased, thus screening (reducing) the charge of the impurity or the Coulomb center. Stern et al [22] have derived an expression for the scattering potential due to impurities. Yokoyama and Hess [28] have devised a method of finding the scattering rate due to impurities using the approach of Stern et al [22].

If $\Phi(r,z)$ is the scattering potential due to impurities, then,

$$\nabla^2\Phi(r,z) - 2\sum_i S_i g_i(z) \int \Phi(r,z) g_i(z_1) dz_1 = \frac{-e}{\epsilon_0 \epsilon_S}\delta(r)\delta(z-z_0) \tag{3.30}$$

where $S_i = \frac{e^2}{2\epsilon_0\epsilon_S}\frac{N_i}{E_{di}}$, with

$$E_{di} = k_B T \left[1 + exp[-\frac{E_F - E_i}{k_B T}]\right] ln \left[1 + exp[\frac{E_F - E_i}{k_B T}]\right] \tag{3.31}$$

In the above equation, S_i is the screening constant, $g_i(z)$ is the electron density function given by $F_i^2(z)$. E_{di} is the diffusion energy, E_F is the Fermi level and E_i is the energy level for the i^{th} subband. N_i is the 2-D carrier density given by the expression:

$$N_i = \frac{m^* k_B T}{\pi\hbar^2} ln \left[1 + exp[\frac{E_F - E_i}{k_B T}]\right] \tag{3.32}$$

In equation (3.30), the term $2\sum_i S_i g_i(z) \int \Phi(r,z) g_i(z_1) dz_1$ represents the charges that are induced because of the presence of impurity atoms. The term on the right hand side of that equation gives the charge density due to ionized impurities. Screening of the impurity potential through the presence of the 2-DEG is taken into account with the second term on the left hand side which involves S_i and $g_i(z)$.

By solving equation (3.30) for Φ, one can find the matrix element and the scattering

rate due to impurity scattering, by following a procedure similar to what had been discussed for POP in Section 3.3. It can be shown that the scattering rate due to impurity scattering is given by the expression:

$$S_{mn}^{IMP}(\overline{k_0}) = \frac{1}{2\pi\hbar}\int |M_{mn}(Q)|^2 \delta(E(\overline{k_0'}) - E(\overline{k_0}))d\overline{k_0'} \tag{3.33}$$

where

$$|M_{mn}(Q)|^2 = \int M_{mn}^2(z_0)N_I(z_0)dz_0 \tag{3.34}$$

with

$$M_{mn}(z_0) = \int e\Phi(Q,z)F_m(z)F_n(z)dz \tag{3.35}$$

In equations (3.33) to (3.35), $Q = 2\overline{\mathbf{k_0}}cos\theta$, where $\overline{\mathbf{k_0}}$ is the absolute value of $\overline{k_0}$ and θ is the angle between $\mathbf{Q}$ (with $\mathbf{Q} = \pm(\overline{k_0} - \overline{k_0'})$) and $\overline{k_0}$. $N_I(z_0)$ is the impurity concentration at $z = z_0$.

In the absence of the undoped *AlGaAs* spacer layer, impurity scattering is a major scattering process in the bulk material, but since a spacer is assumed in the HEMT structure, of this study, the scattering rates are very small. Because most of the electrons are in the first subband and because the scattering rates are small, only the intrasubband transitions due to ionized impurity scattering need to be considered [28]. Hence the scattering rate for intrasubband transitions due to ionized impurity scattering, from equation (3.33) is given by: [28]

$$S_{mm}^{IMP} = \frac{m^*}{\pi\hbar^3}\int_0^\pi |M_{mm}(Q)|^2 d\theta \tag{3.36}$$

Chapter 4

RESULTS AND DISCUSSION

4.1 Procedure for obtaining 1-D E_c profile cut-section along the channel

The material parameters for our HEMT device structure are presented in Table 4.1. A schematic picture of the device is shown in Figure 4.1.

Since, the analysis of this work requires that the device be in the ohmic region the applied voltages V_{GS} and V_{DS} are chosen, such that the device is operating in the ohmic region. From the realistic output characteristics of a HEMT, which had geometric parameters close to the one employed for this study, an operating point (V_{GS}, V_{DS}, I_D) was chosen in the ohmic region. The source to drain voltage, V_{DS}, and the gate to source voltage, V_{GS}, were found to be 0.6 V and 0.6 V (gate is at a higher potential than the source), respectively. As in a field effect transistor operating in the ohmic region, the potential difference between the gate and various points along the channel ($GaAs/AlGaAs$ interface) varies from V_{GS} at the source to $(V_{GS} - V_{DS})$ at the drain. It is noted that the

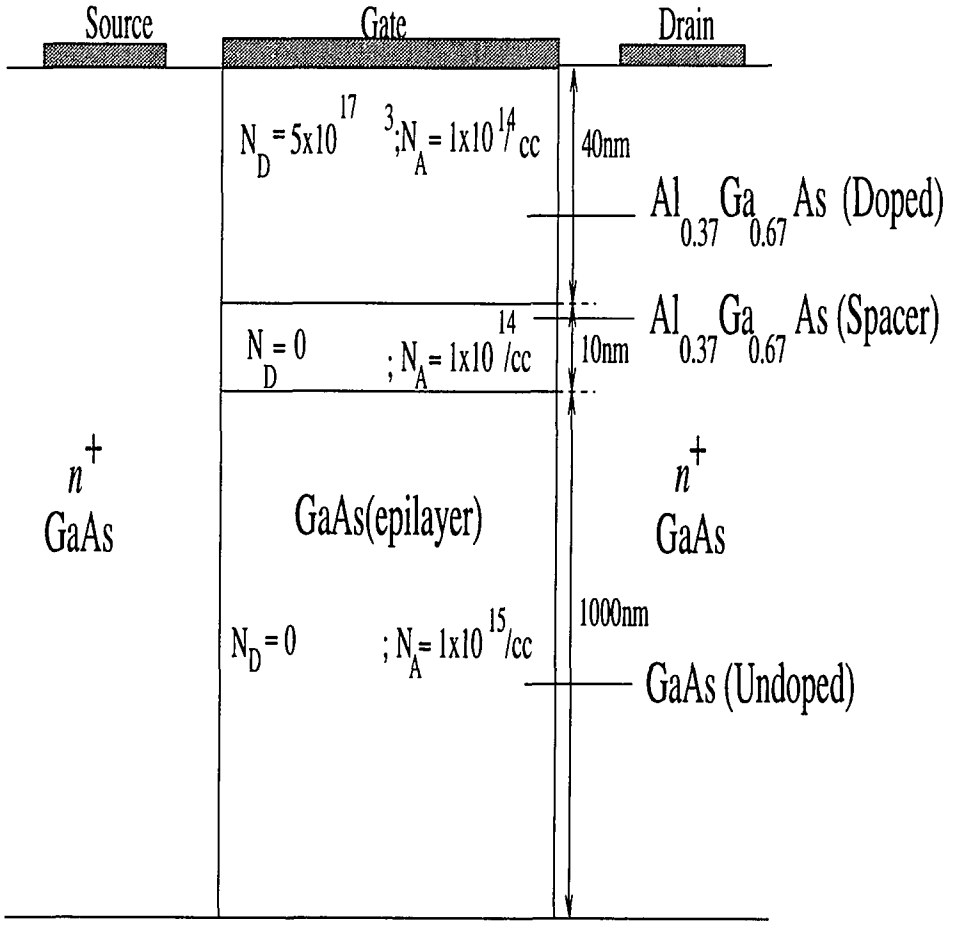

Figure 4.1: A schematic picture of the HEMT device structure.

Material	*Dopant Density* (cm^3)	*Thickness* (nm)
$GaAs$	$N_D = 0.0$; $N_A = 1$ x 10^{15}	1000
$Al_{0.37}Ga_{0.63}As$	$N_D = 0.0$; $N_A = 1$ x 10^{14}	10
$Al_{0.37}Ga_{0.63}As$	$N_D = 5.0$ x 10^{17}; N_A=1 x 10^{14}	40

Table 4.1: Material parameters for the device structure shown in Figure 4.1.

gradual channel approximation holds because the device is in the ohmic region. In other words, the 2-D Poisson's equation can be decoupled into two 1-D Poisson's equations. It is also important to note that the purpose of the analysis here does not require knowledge of the type of variation of V_{GC} along the channel as a complete device modeling is not attempted and the only goal of this work is to find out if the transport properties vary along the channel. Thus, the gate to channel voltage V_{GC} can vary in the range from 0.6 V at the source to 0.0 V at the drain. For our purpose, three points along the channel from the source to the drain, have been taken into consideration: the point closest to the source characterized by V_{GC} = +0.6 V, a point near the drain characterized by V_{GC} = +0.0 V and a point midway between these two, characterized by V_{GC} = +0.3 V. The length of the channel is 1.5 μm.

A one-dimensional Poisson solver (FISH1D 2.2) [7] was employed to obtain the one-dimensional gate to channel conduction band edge profile for three locations along the channel. The conduction band edge profiles are shown in Figure 4.2. The well width and depth are observed to be dependent on the channel location with a deeper and narrower well at the source end and a shallower and broader well at the drain end. This is indicative of 2-DEG at the source which becomes less confined along the channel towards the drain.

The conduction band edge profiles are used in the time independent Schrödinger

equation and the energy Eigen values and the corresponding wave functions are obtained using the Numerov method [3]. In this study, the energy Eigen values and wave functions are obtained for the first five subbands for three channel locations. The energy Eigen values at the source and the drain are shown in Figure 4.3 and 4.4. It can be observed that the first Eigen value occurs at a value of -4.71 eV at the source end whereas it occurs at -4.64 eV at the drain end. A similar comparison of other Eigen values occurring at the source and the drain end as well at the intermediate channel location clearly indicate that the values are not the same because of the variation in quantum confinement from the source to the drain.

The subband energies and wave functions are observed to vary from the source end to the drain end due to varying quantum confinement. The energy Eigen value difference between the m^{th} and n^{th} subbands, which is an important parameter in deciding the allowed absorption mechanisms for the POP scattering shows considerable variation from the source to the drain with lower values at the drain. It is noted that the wave function at the source end is sharper and narrower compared to that at the drain end.

The normalized wave functions for the first two subbands at the source and at the drain end are shown in Figures 4.5 through Figure 4.8.

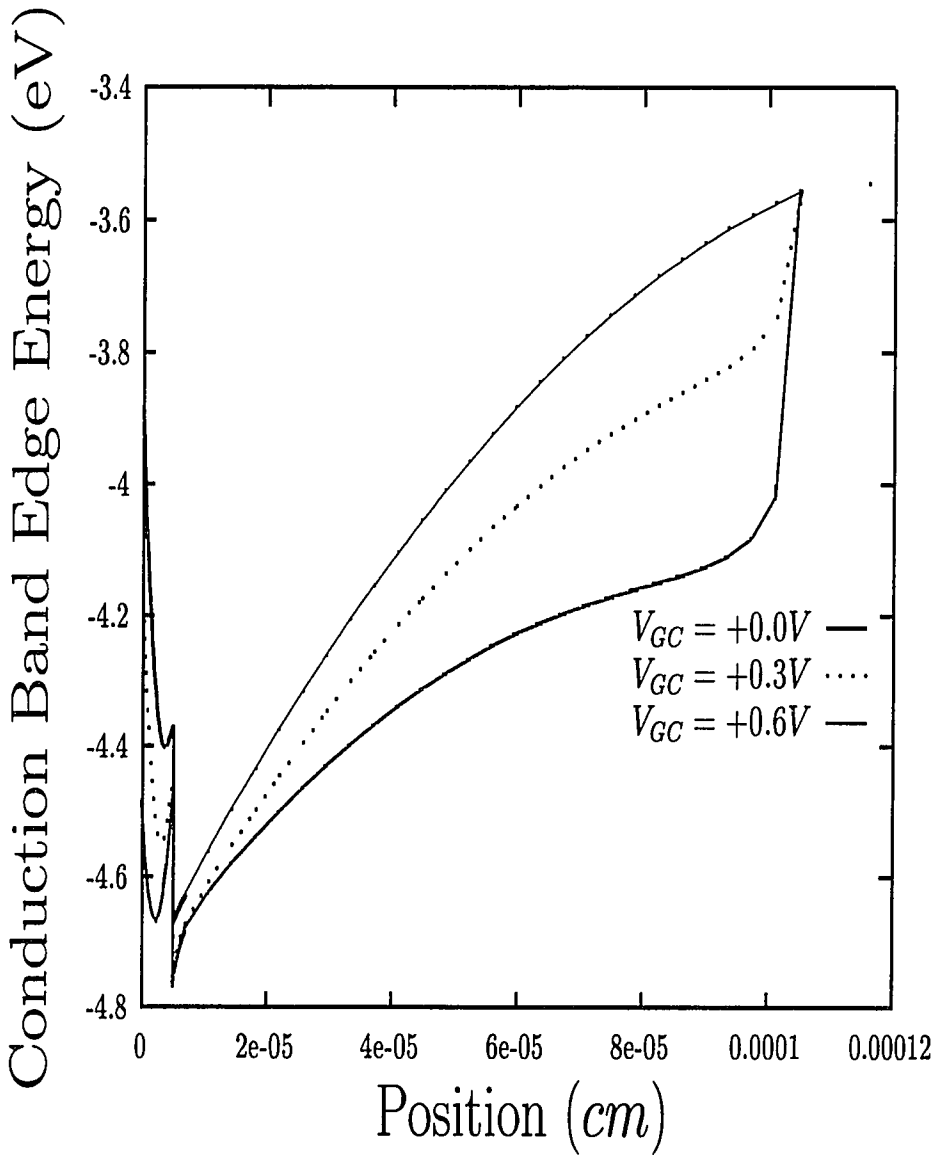

Figure 4.2: 1-D E_C profiles for various channel position corresponding to various V_{GC}'s.

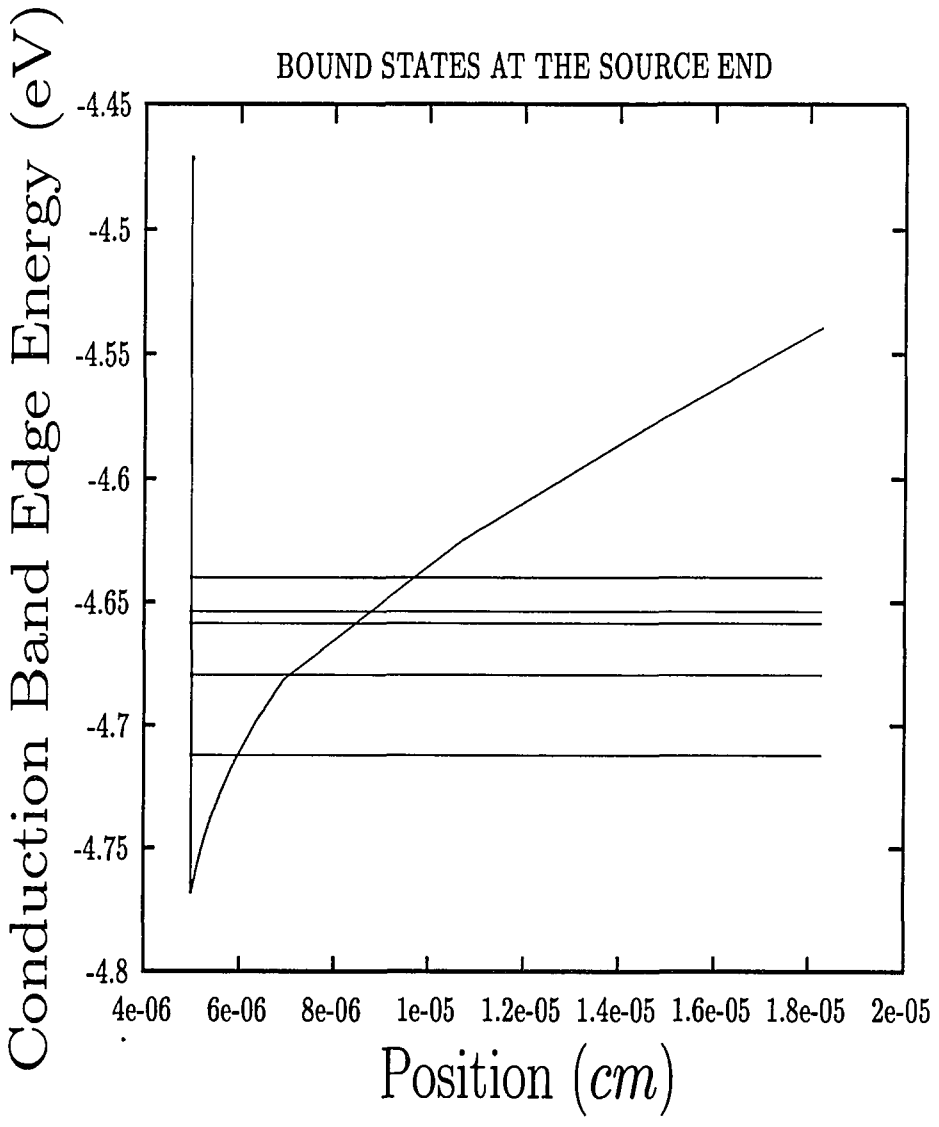

Figure 4.3: Bound state energy values for the source end

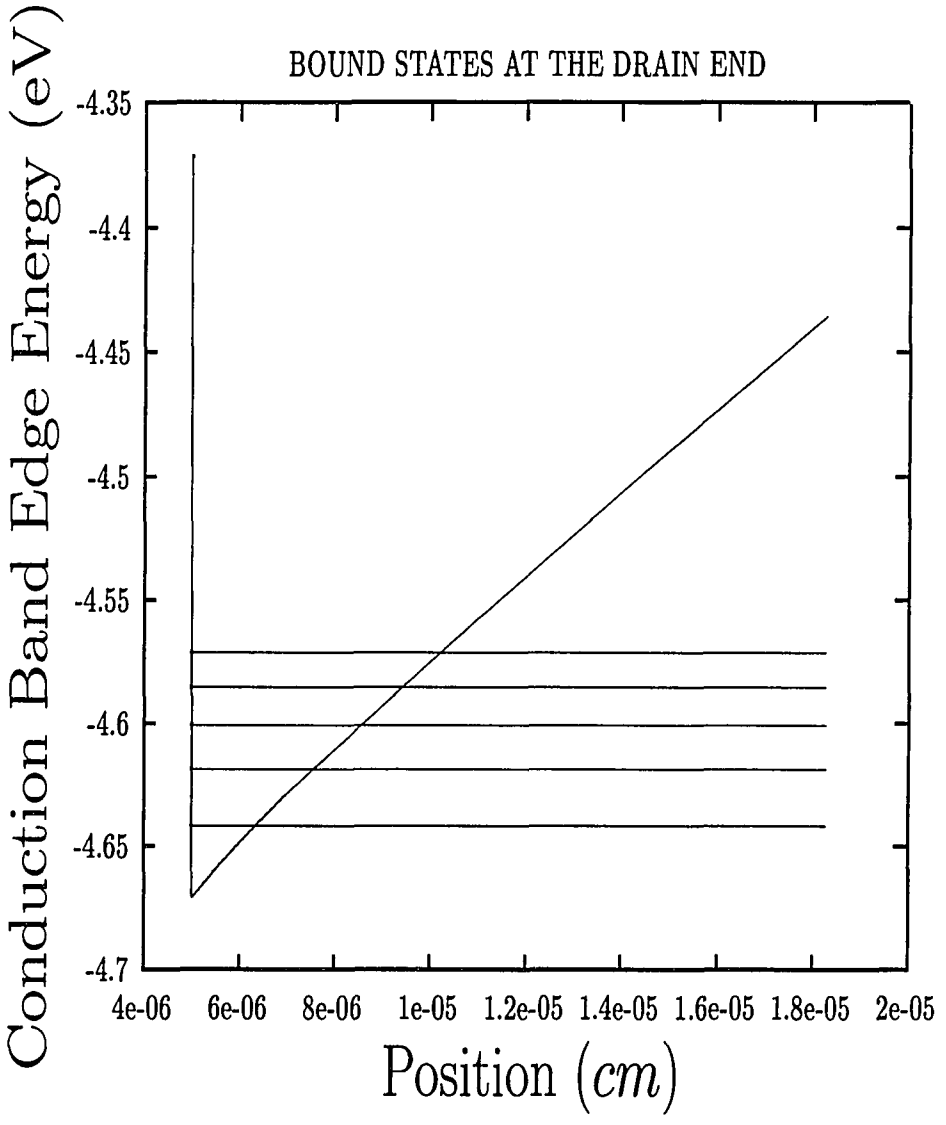

Figure 4.4: Bound state energy values for the drain end.

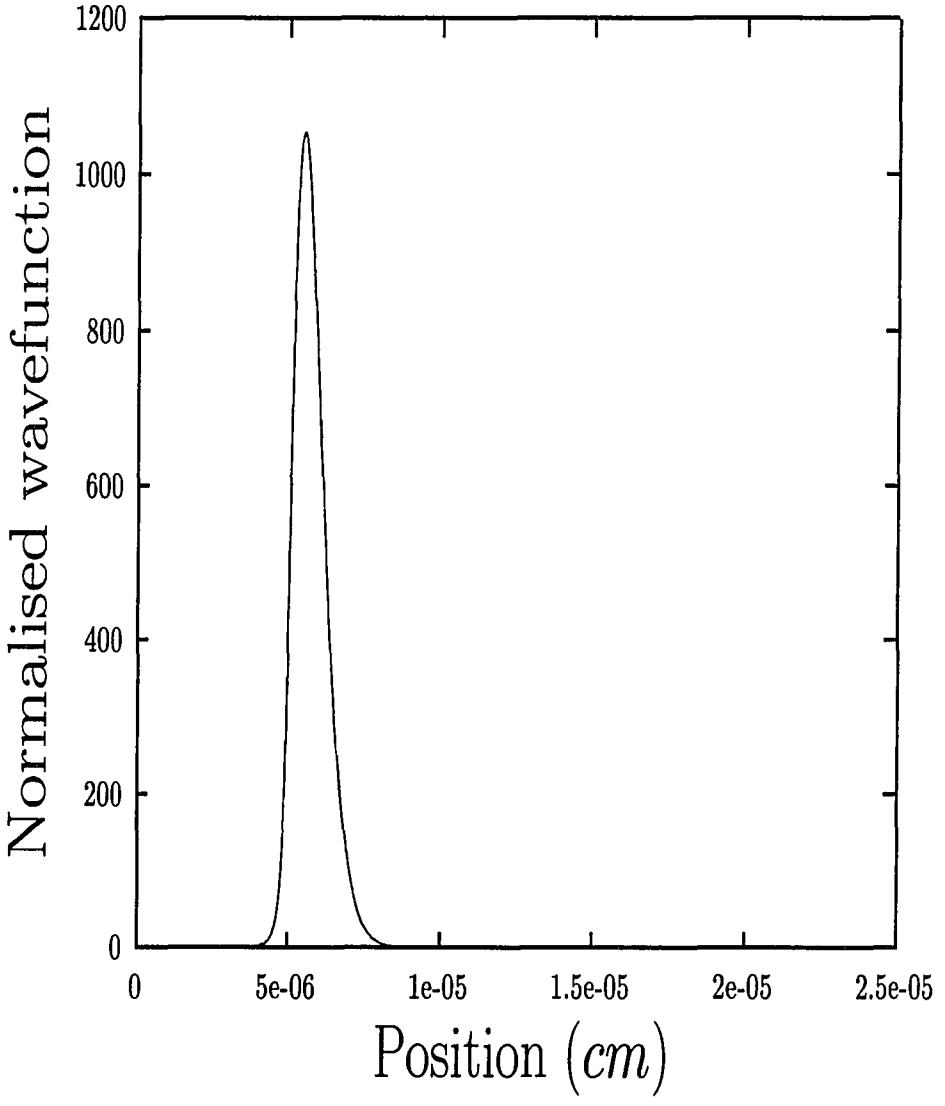

Figure 4.5: Plot of normalized wave function (first subband) versus position for the source end.

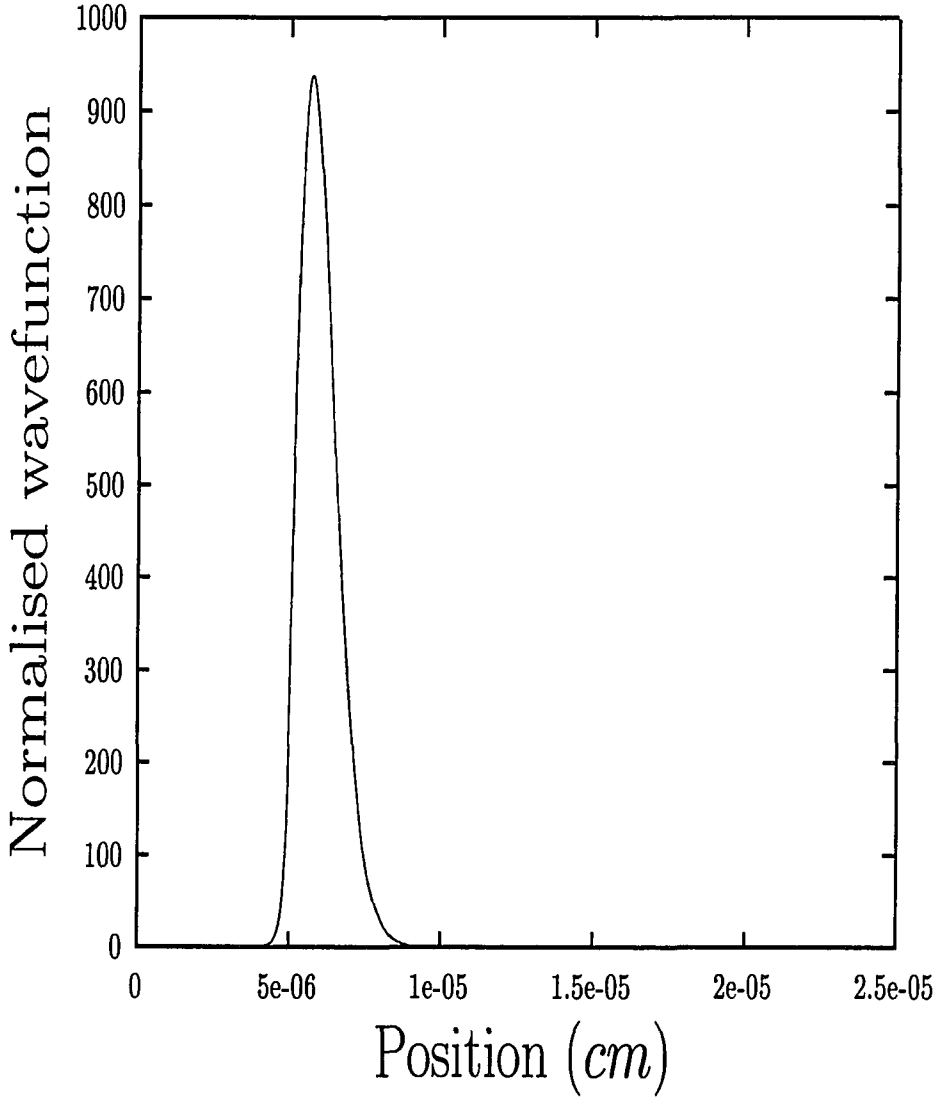

Figure 4.6: Plot of normalized wave function (first subband) versus position for the drain end.

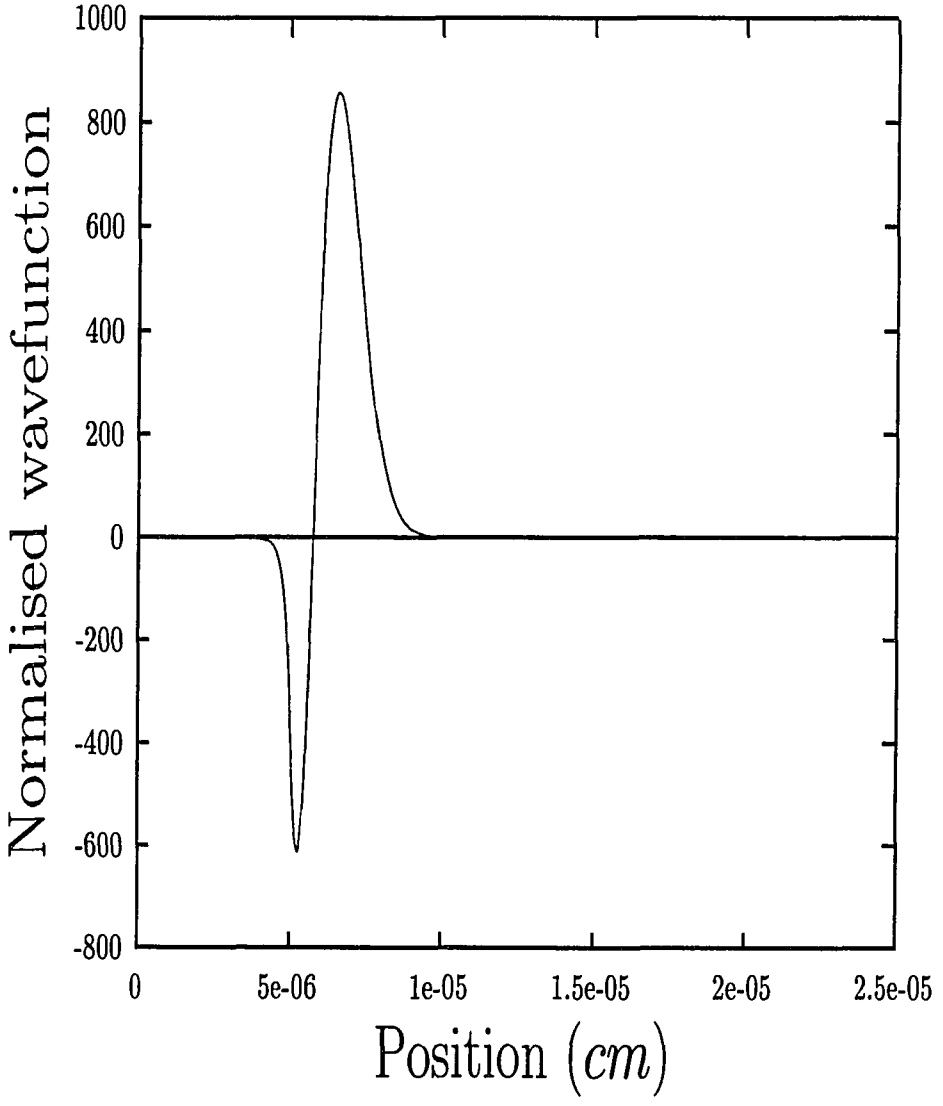

Figure 4.7: Plot of normalized wave function (second subband) versus position for the source end.

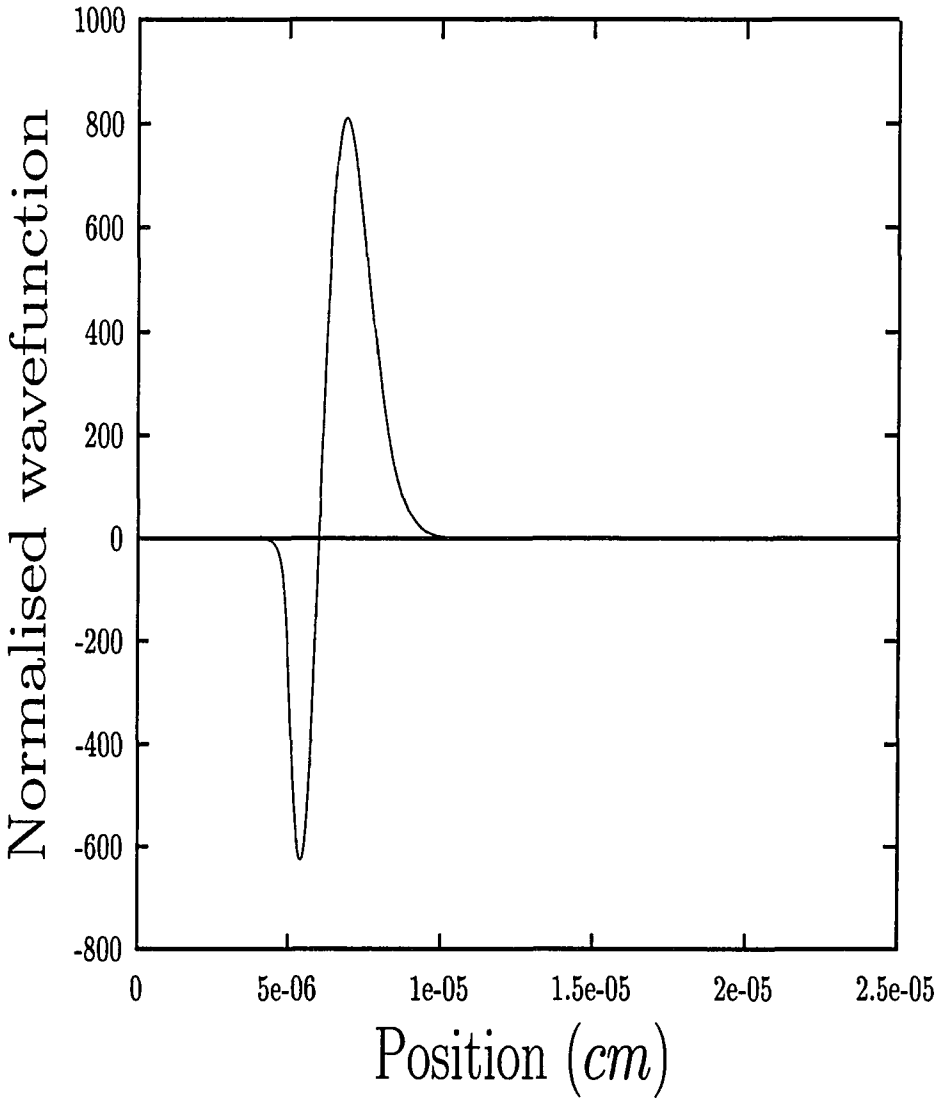

Figure 4.8: Plot of normalized wave function (second subband) versus position for the drain end.

4.2 POP scattering mechanism

In this section, the POP scattering rates are obtained as a function of the incident electron energy and the channel location for various intersubband and intrasubband scattering mechanisms. POP scattering is one of the dominant scattering mechanisms in $GaAs$ at high

Material Constant	Symbol	Value
Effective mass	m^*	0.065 m_o#
Optical dielectric constant	ϵ_∞	10.92 ϵ_0##
Static dielectric constant	ϵ_s	12.90 ϵ_0 ##
Polar optical phonon energy	$\hbar\omega_o$	0.0354 eV.
Velocity of sound in $GaAs$	S_l	5.24 x 10^5 cm/sec.
Deformation potential of $GaAs$	D	13.5 eV
Density of $GaAs$	ρ	5.36 gm/cm^3

Table 4.2: Material constants for the POP and AP scattering calculations.

temperatures such as 300°K. It can influence the room temperature transport properties and hence the performance of $GaAs/AlGaAs$ HEMTs [18, 3]. If $\overline{k_0}$ and $\overline{k_0'}$ are the initial and final wave vectors for the electron, the 2-D scattering rate for the POP mechanism can be obtained using the Fermi's golden rule as discussed in the Section 3.3.1, using equation (3.25) [28, 2, 18].

The physical and material constants employed for the device are listed in Table 4.2. Using equation (3.25), the POP scattering rates are found for various possible intrasubband and intersubband scattering mechanisms for the three channel locations. The scattering rates for various intrasubband and intersubband scattering mechanisms for POP absorption and emission for various channel locations are shown in Figures 4.9 through 4.39.

4.2.1 Qualitative observations

In general the trend expected as in [28, 1] is obtained. As the incident energy increases, the scattering rate decreases. Note that at the drain end the electrons are less confined and hence the behavior is closer to 3-D electrons. Additionally as the incident energy increases, the scattering rates for various locations along the channel converge to the same value. This is due to the fact that the electron with high energy compared to the potential well resembles

Scattering from m^{th} subband to n^{th} subband	Maximum difference in % between the source and the drain at same incident energy
1 $\longrightarrow$ 1	13
1 $\longrightarrow$ 2	21
2 $\longrightarrow$ 1	28
2 $\longrightarrow$ 2	12
3 $\longrightarrow$ 1	16
3 $\longrightarrow$ 2	4
3 $\longrightarrow$ 3	8
3 $\longrightarrow$ 5	91
4 $\longrightarrow$ 4	107
5 $\longrightarrow$ 1	31
5 $\longrightarrow$ 2	55
5 $\longrightarrow$ 3	86
5 $\longrightarrow$ 5	23

Table 4.3: Maximum difference between the source and the drain in the scattering rate for various POP intersubband and intrasubband absorption mechanisms.

a classical, unconfined electron. The maximum difference in scattering rate predominantly occurs at low energies for all mechanisms with the exception of a few. The intersubband emission mechanisms show a distinctive energy shift between the source and the drain as seen in Figures 4.22 to 4.39. This shift is due to change in E_i subband values and hence $\Delta E_{ij} = E_i - E_j$ value for the source and the drain due to varying quantum confinement. At the drain, E_i's are closer and hence ΔE_{ij}'s are small and therefore, intersubband emission mechanism begins at lower incident energy of electrons.

The maximum difference in scattering rates is computed between the source and the drain at the same energy for various POP absorption mechanisms and is reported in Table 4.3.

An analysis of the data shown in Figures 4.9 through 4.21 shows that there exists a maximum difference of 107% in the scattering rate for POP absorption between the

Scattering from m^{th} subband to n^{th} subband	Maximum difference in % between the source and the drain at the same incident energy
1 $\longrightarrow$ 1	51
1 $\longrightarrow$ 2	21
1 $\longrightarrow$ 3	10
1 $\longrightarrow$ 5	27
2 $\longrightarrow$ 2	6
2 $\longrightarrow$ 5	49
3 $\longrightarrow$ 1	51
3 $\longrightarrow$ 3	5
3 $\longrightarrow$ 5	88
4 $\longrightarrow$ 2	110
4 $\longrightarrow$ 4	51
5 $\longrightarrow$ 1	42
5 $\longrightarrow$ 2	114
5 $\longrightarrow$ 5	14

Table 4.4: Maximum difference between the source and the drain in the scattering rate for various POP intersubband and intrasubband emission mechanisms.

source and the drain, for the intrasubband scattering mechanism 4 $\longrightarrow$ 4 and the smallest maximum difference of 4%, for intersubband scattering 3 $\longrightarrow$ 2.

The maximum difference in scattering rate for emission mechanism between the source and the drain is computed from Figures 4.22 through 4.39 and is reported in Table 4.4. For POP emission, there exists a maximum difference of 114% for 5 $\longrightarrow$ 2 and the smallest maximum difference of 5% occurs for 3 $\longrightarrow$ 3. The other mechanisms, for which the % variation have not been shown in Tables 4.3 and 4.4, have not been considered for analysis either because the scattering rates were completely absent at the source and were present at the drain or because there was no variation in the scattering rates between the source and the drain, that was substantial.

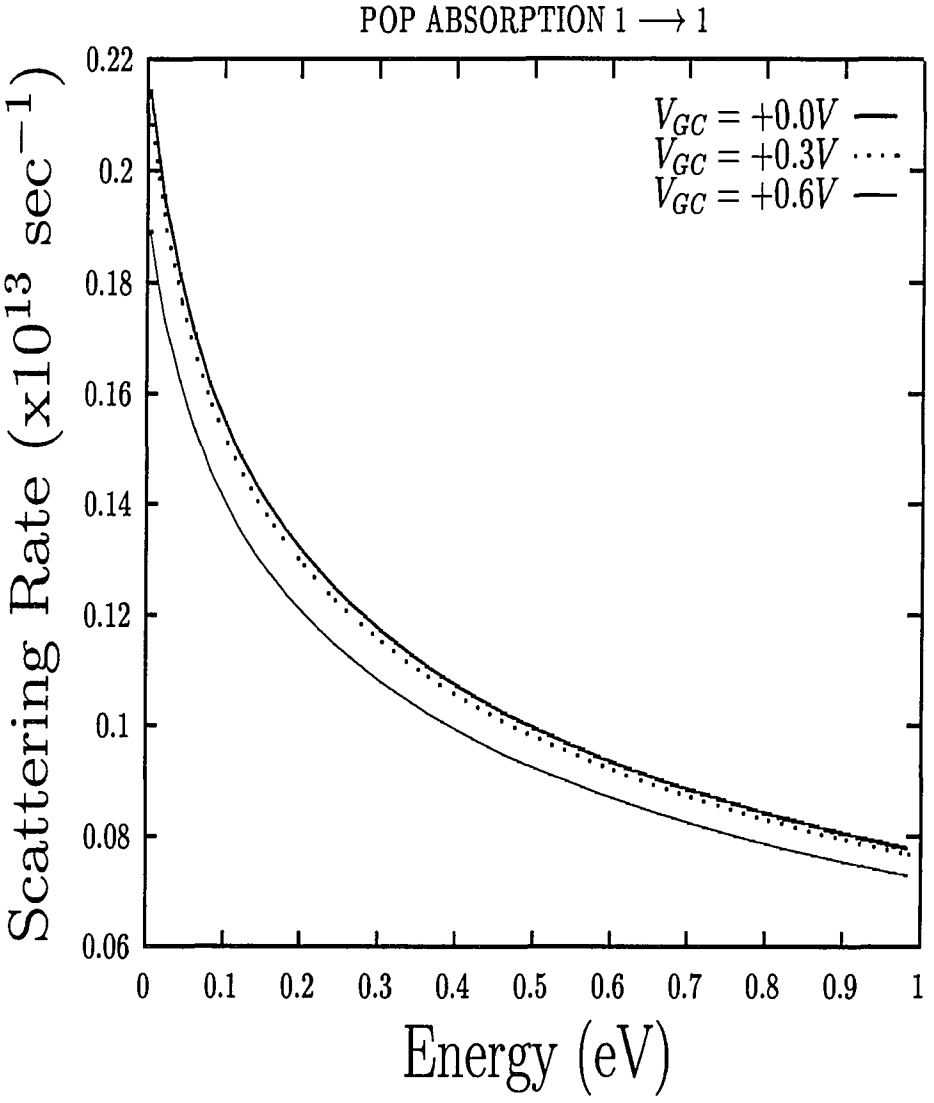

Figure 4.9: POP scattering rates as a function of energy for 1 to 1 absorption mechanism.

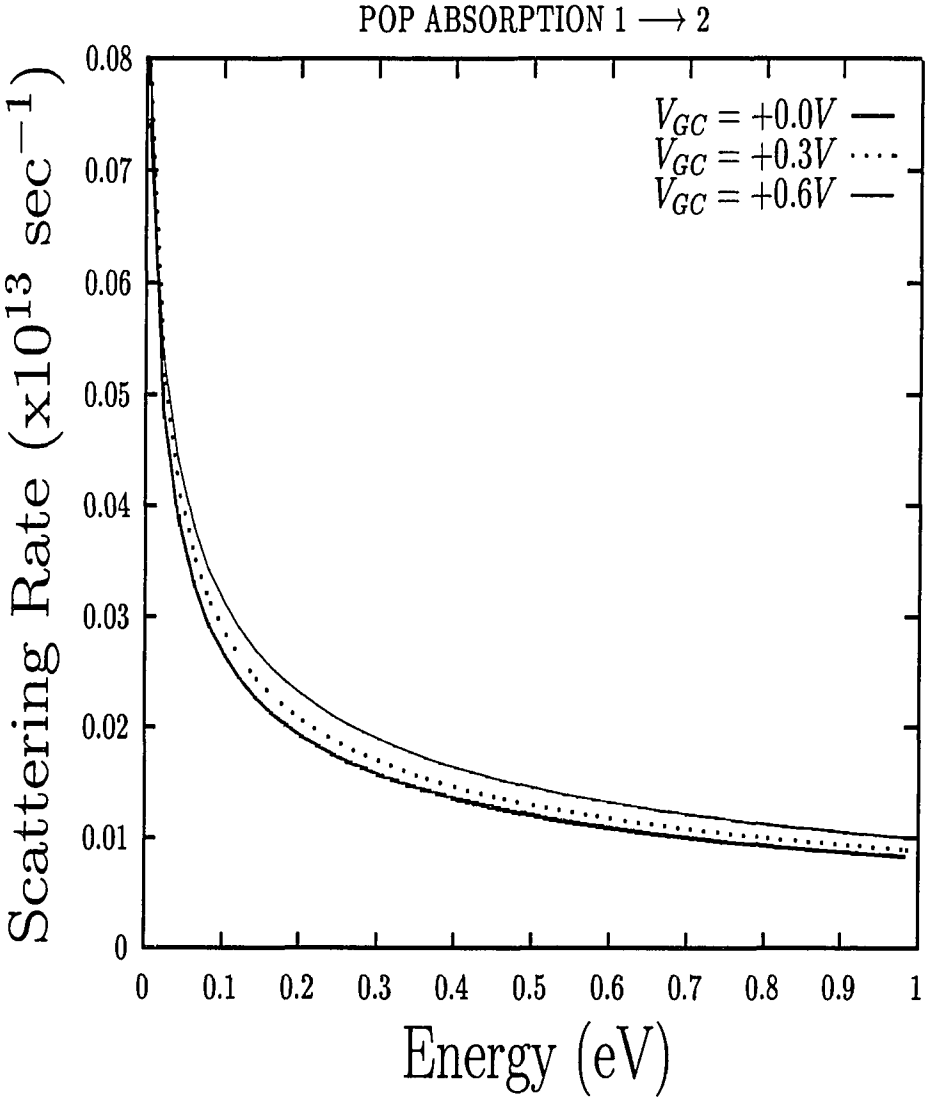

Figure 4.10: POP scattering rates as a function of energy for 1 to 2 absorption mechanism.

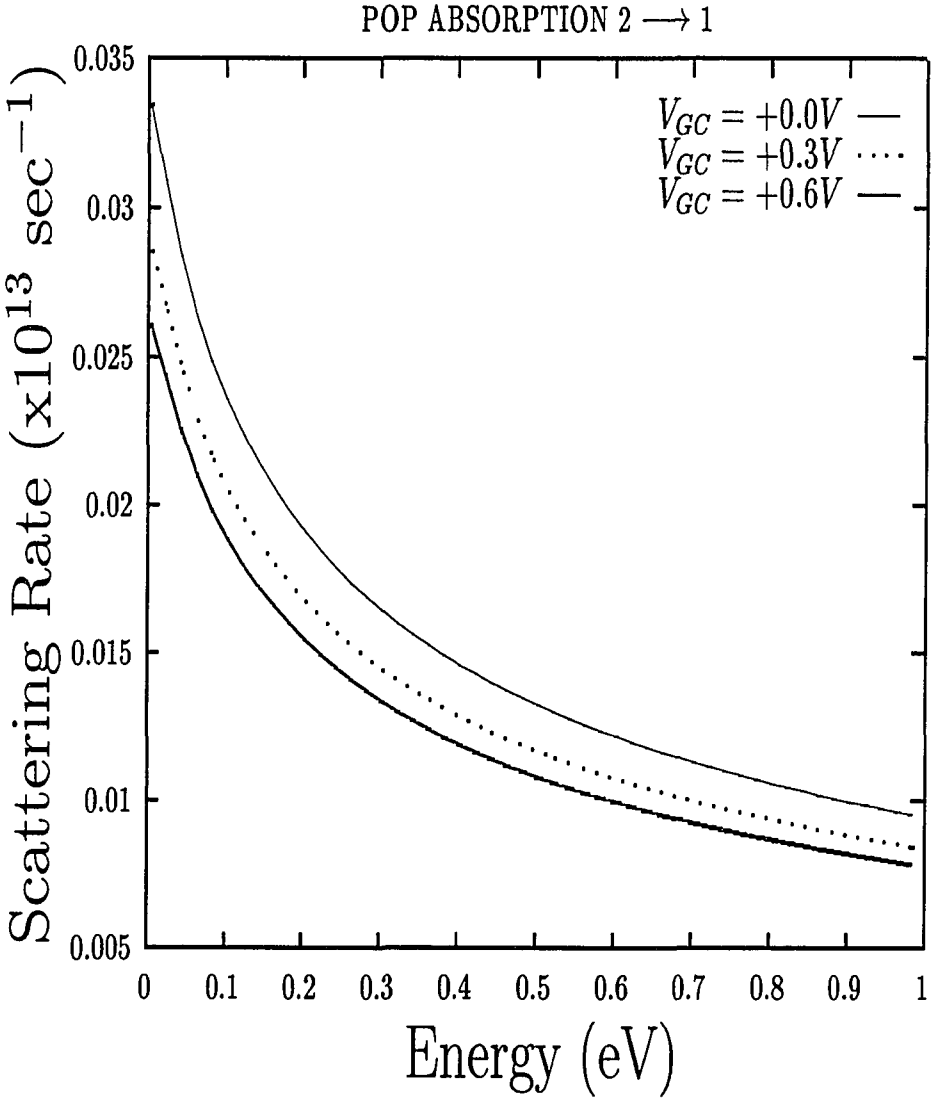

Figure 4.11: POP scattering rates as a function of energy for 2 to 1 absorption mechanism.

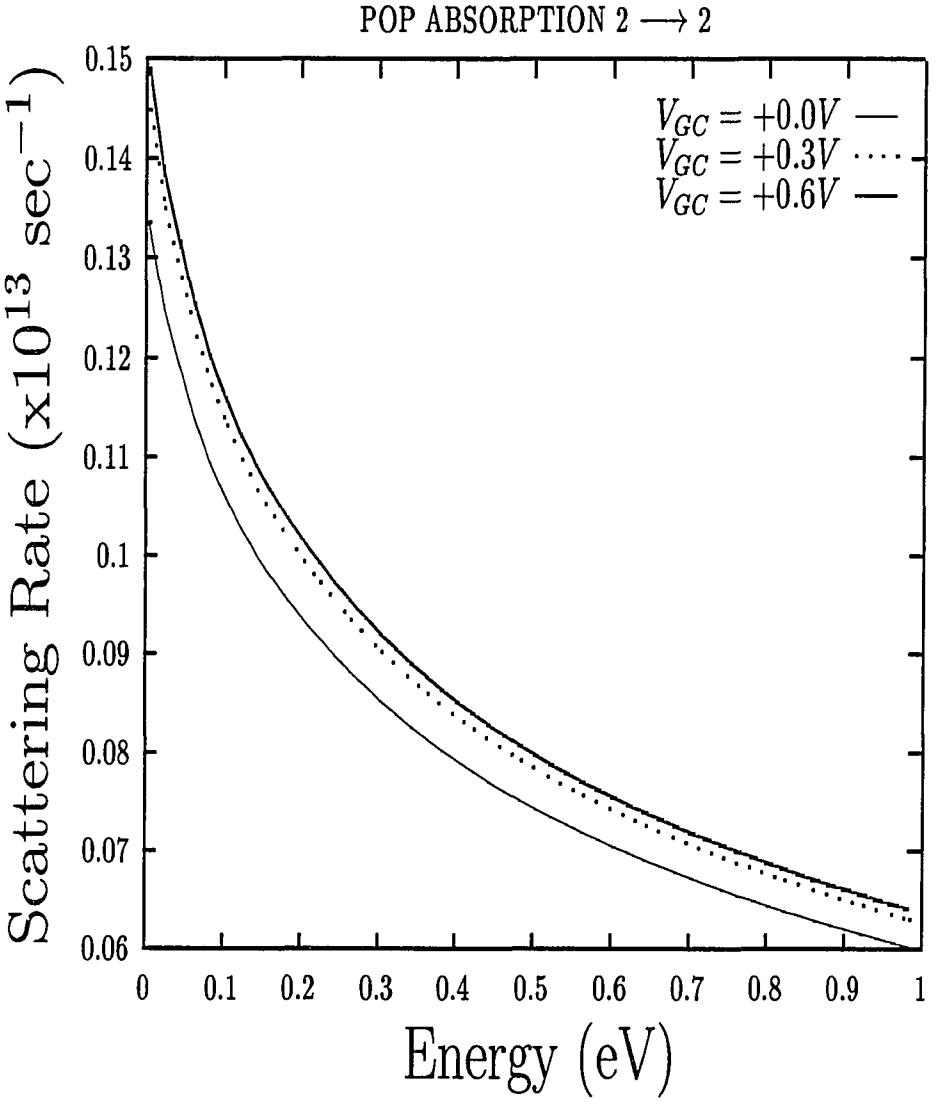

Figure 4.12: POP scattering rates as a function of energy for 2 to 2 absorption mechanism.

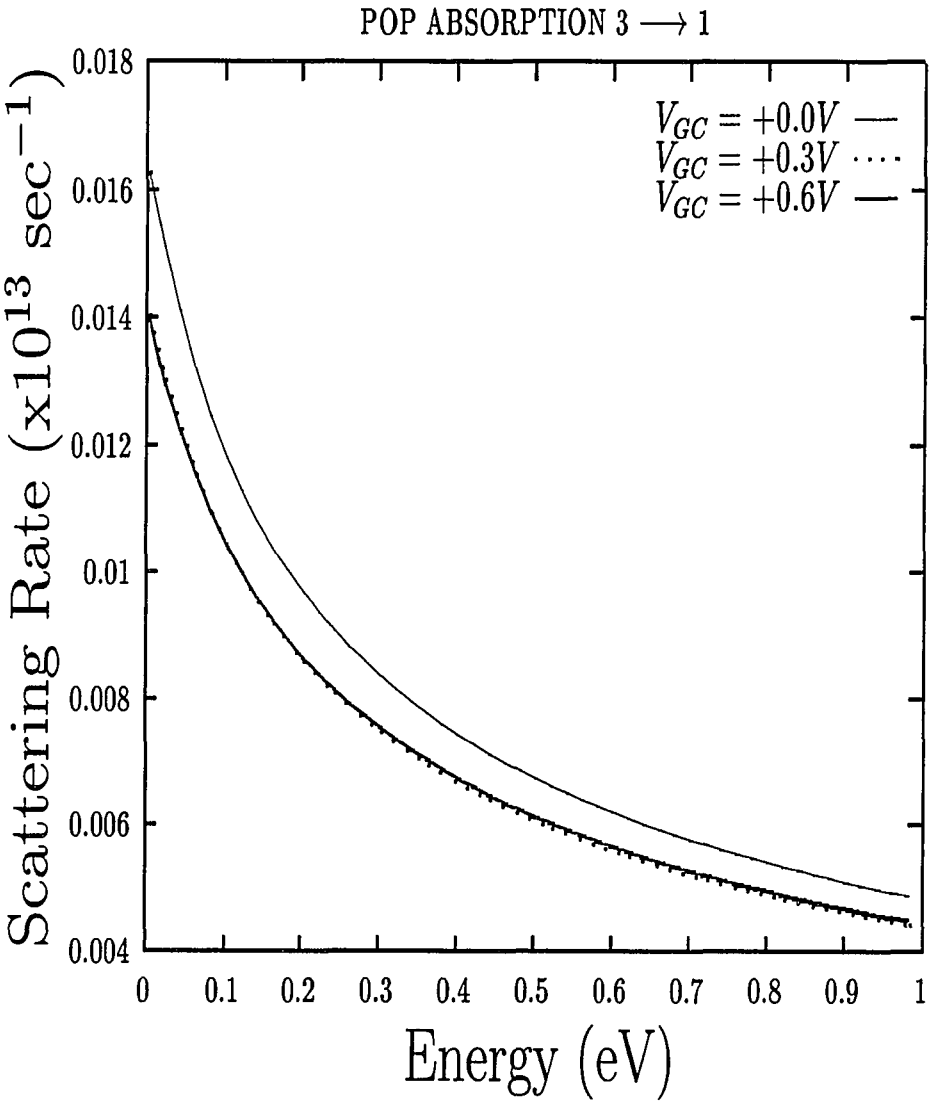

Figure 4.13: POP scattering rates as a function of energy for 3 to 1 absorption mechanism.

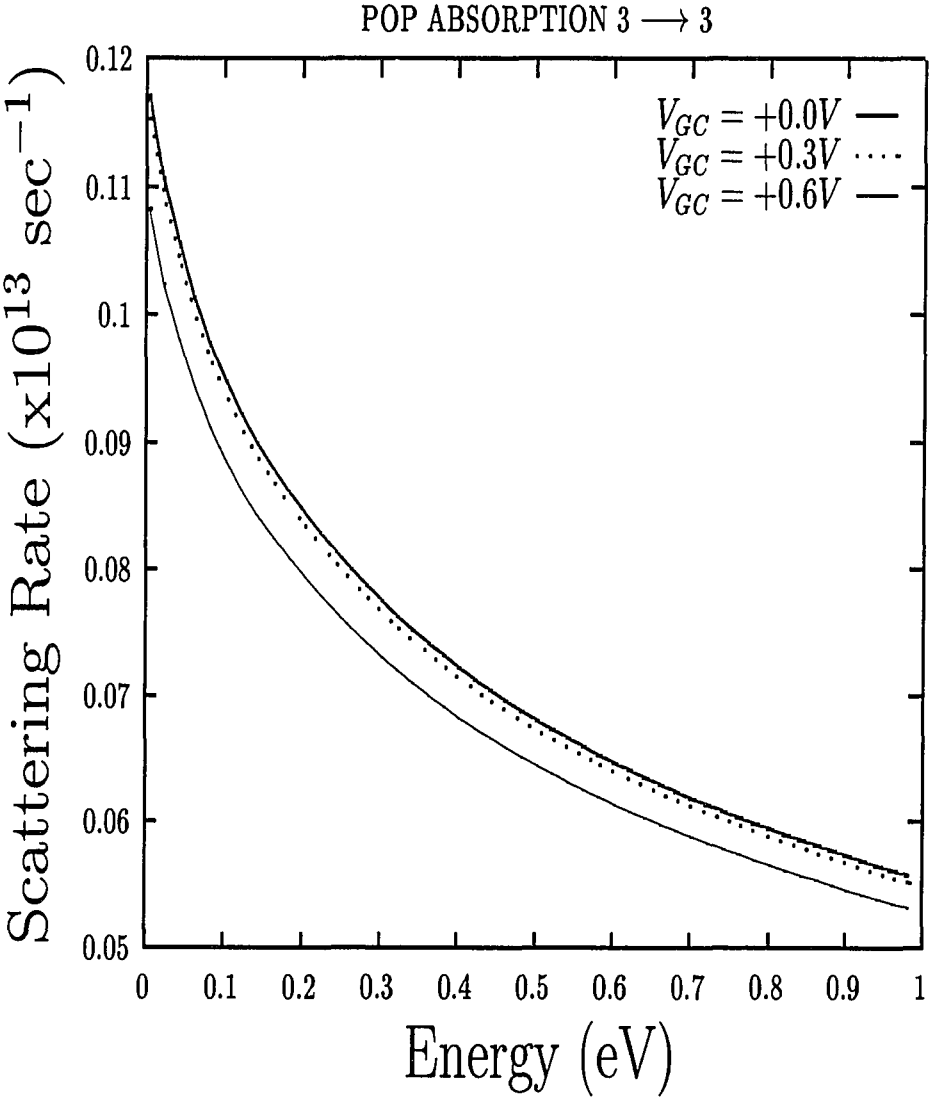

Figure 4.14: POP scattering rates as a function of energy for 3 to 3 absorption mechanism.

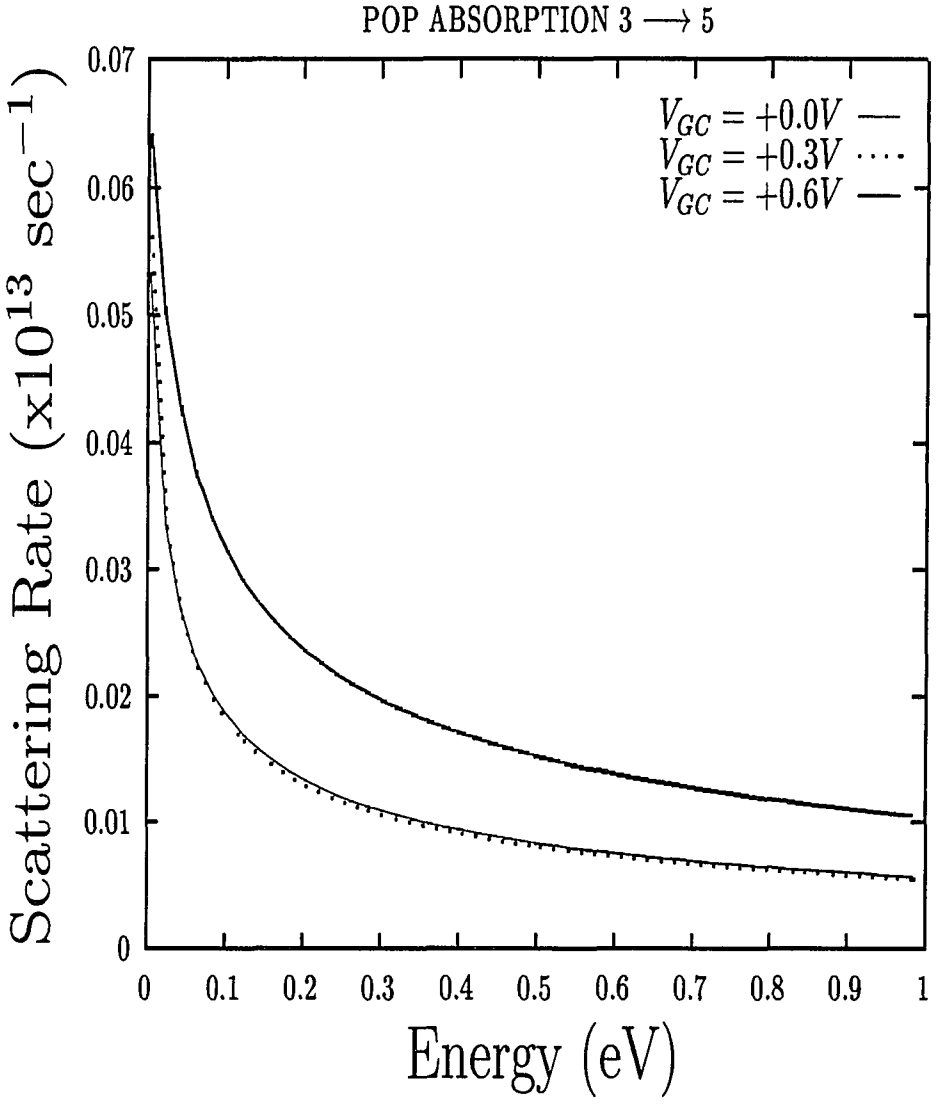

Figure 4.15: POP scattering rates as a function of energy for 3 to 5 absorption mechanism.

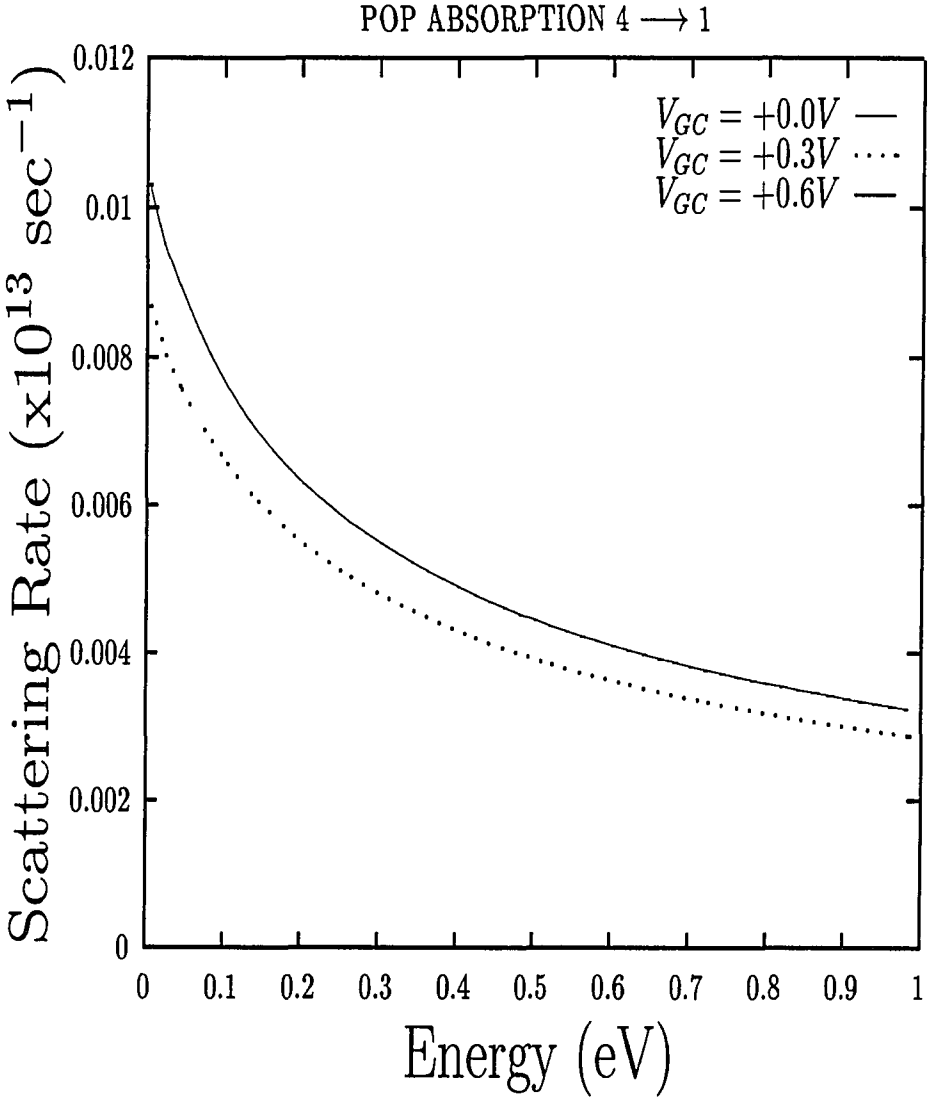

Figure 4.16: POP scattering rates as a function of energy for 4 to 1 absorption mechanism.

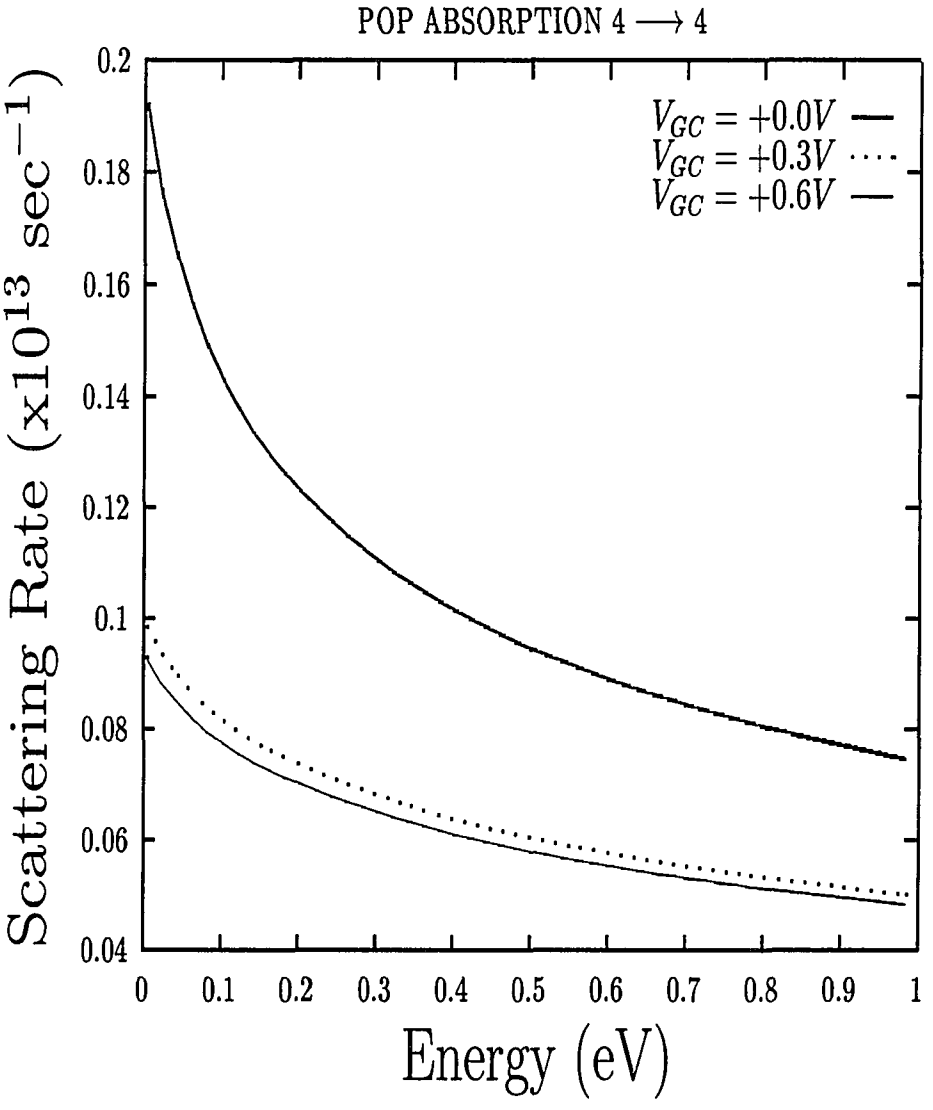

Figure 4.17: POP scattering rates as a function of energy for 4 to 4 absorption mechanism.

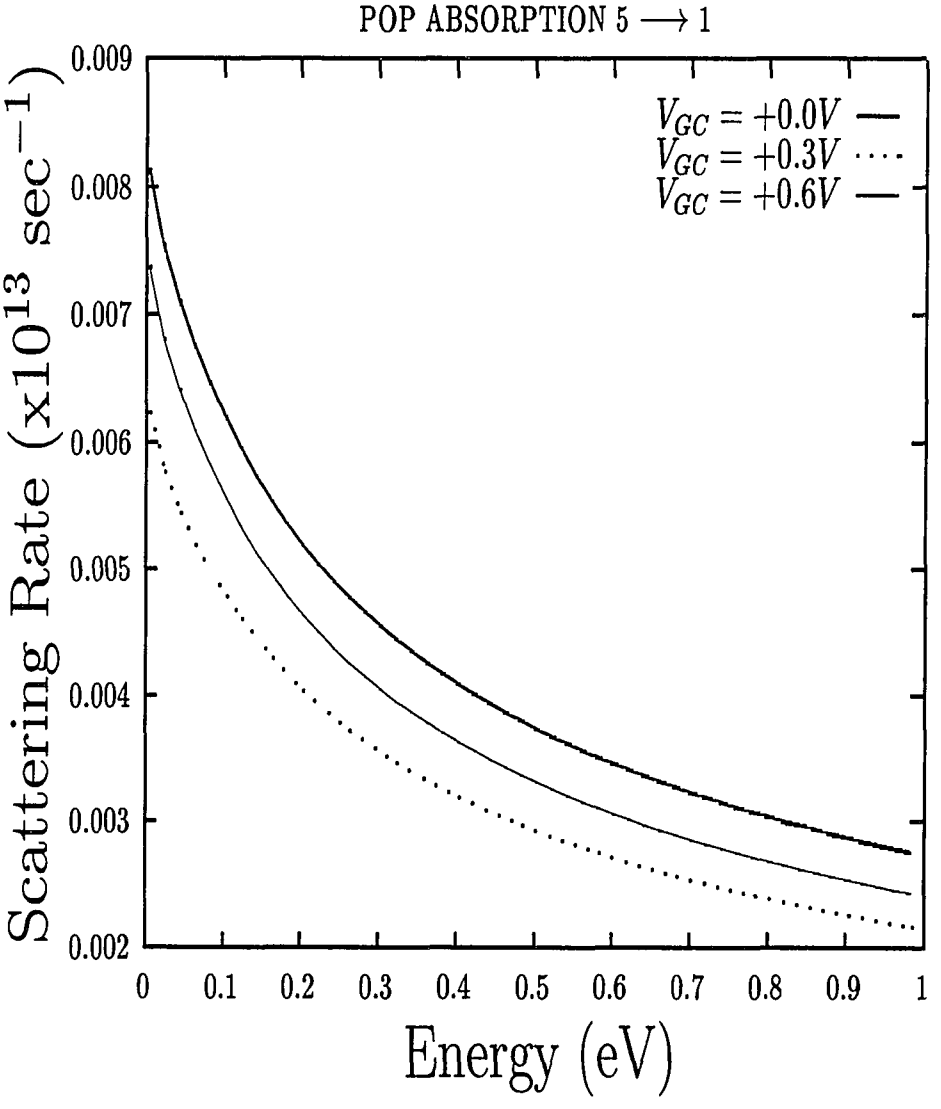

Figure 4.18: POP scattering rates as a function of energy for 5 to 1 absorption mechanism.

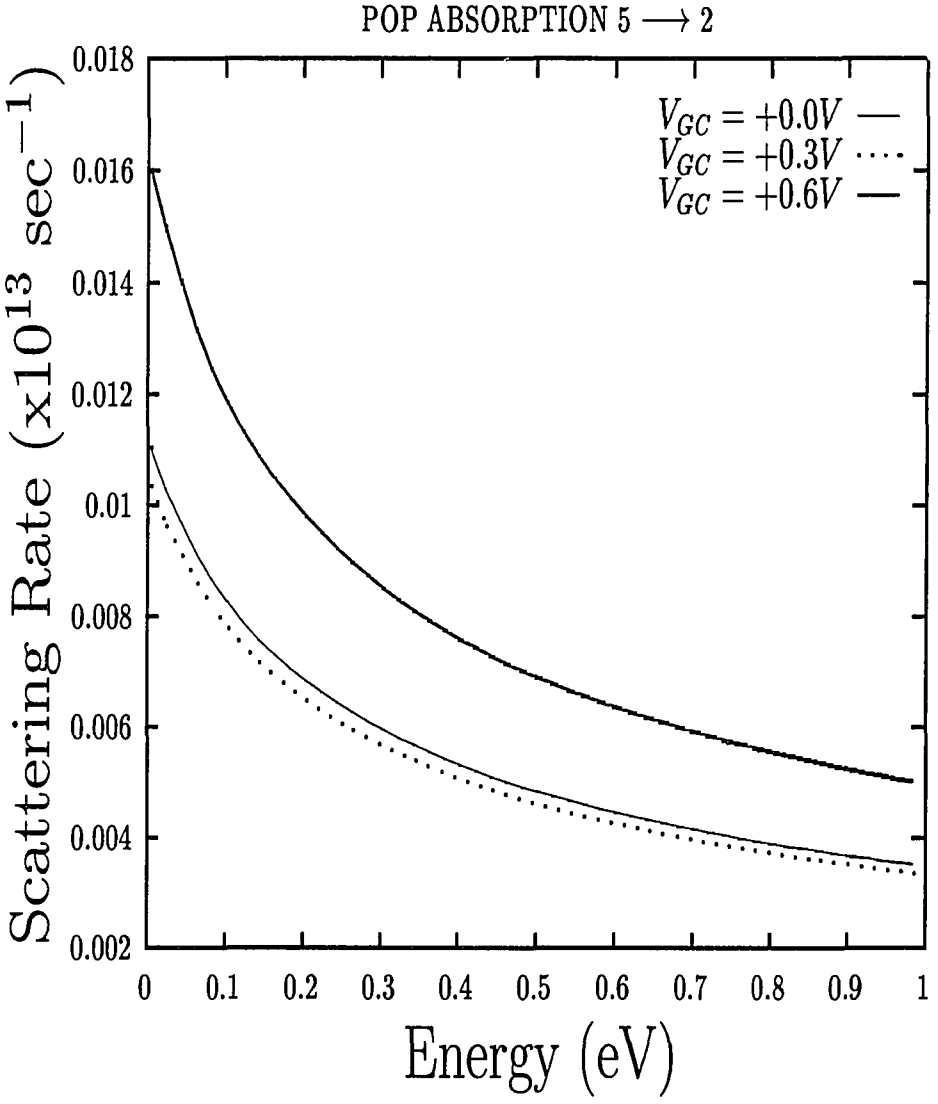

Figure 4.19: POP scattering rates as a function of energy for 5 to 2 absorption mechanism.

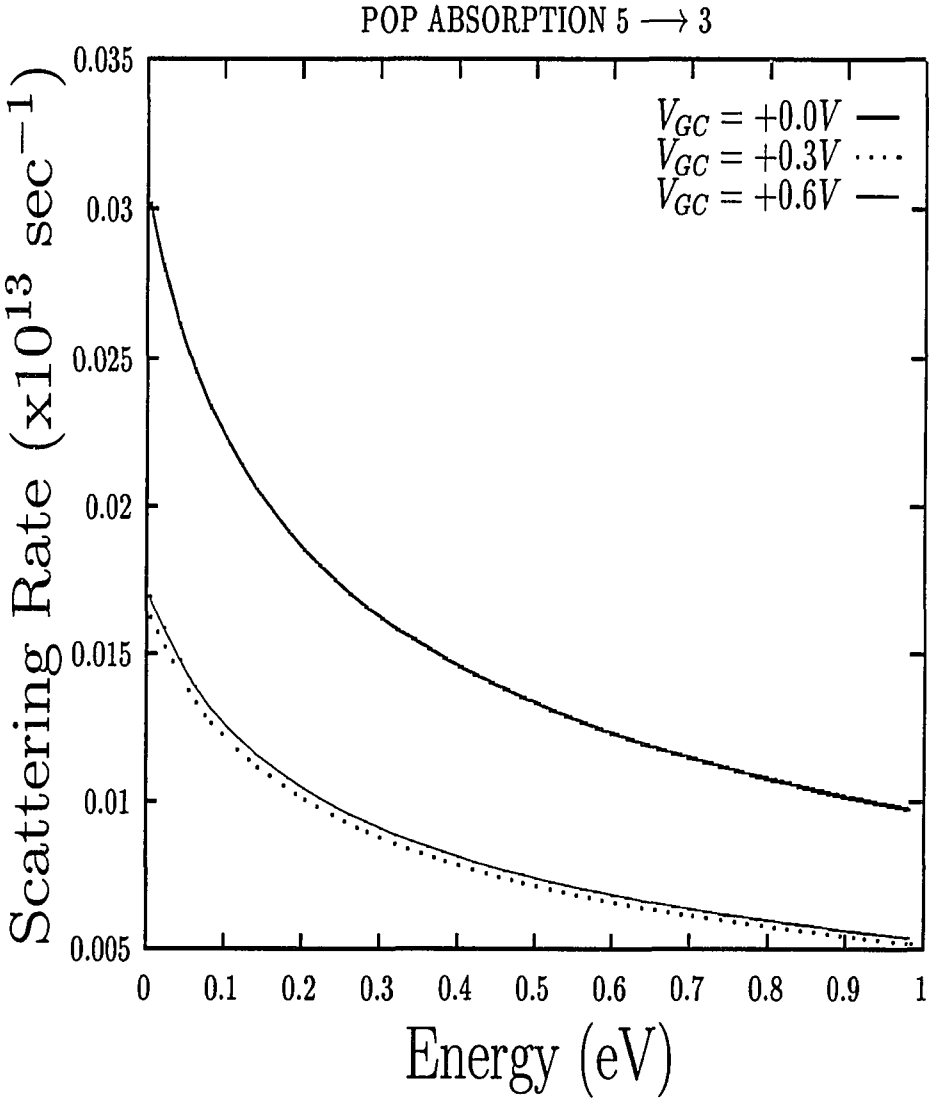

Figure 4.20: POP scattering rates as a function of energy for 5 to 3 absorption mechanism.

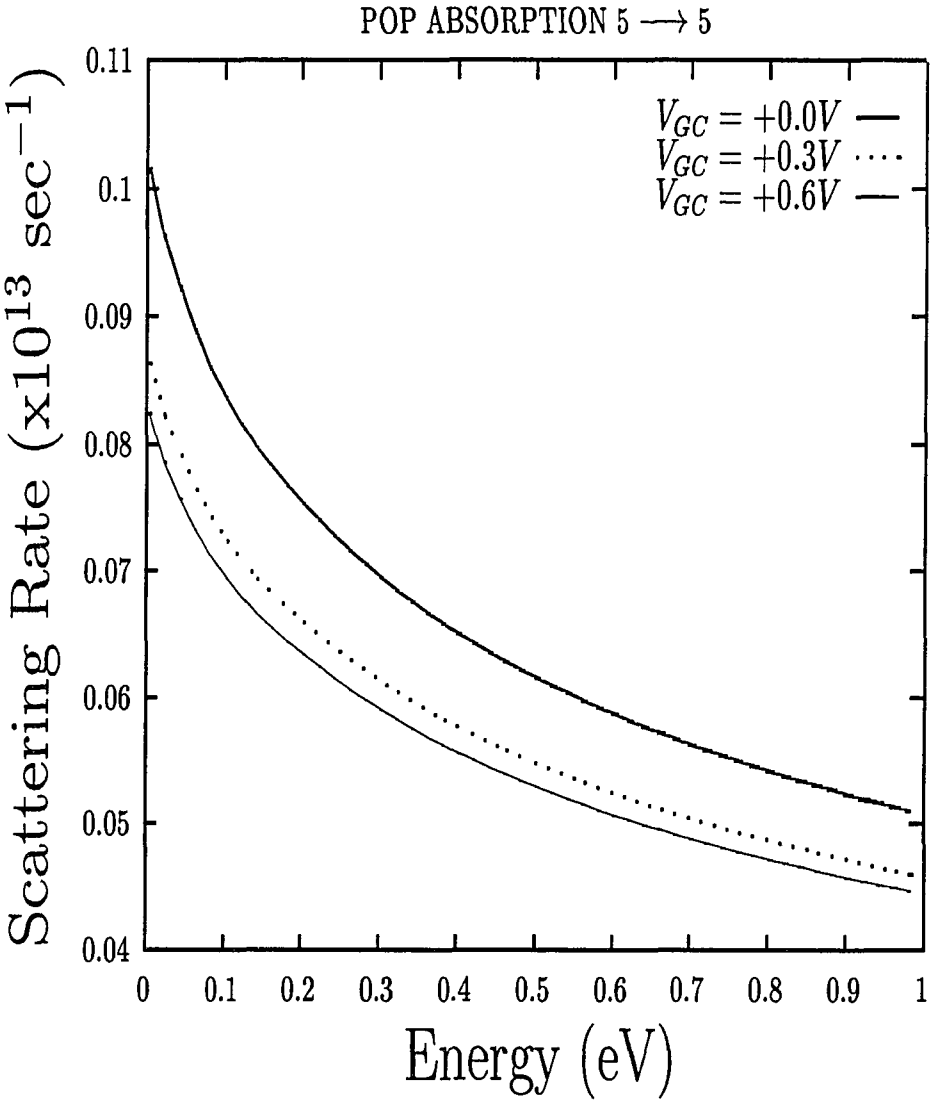

Figure 4.21: POP scattering rates as a function of energy for 5 to 5 absorption mechanism.

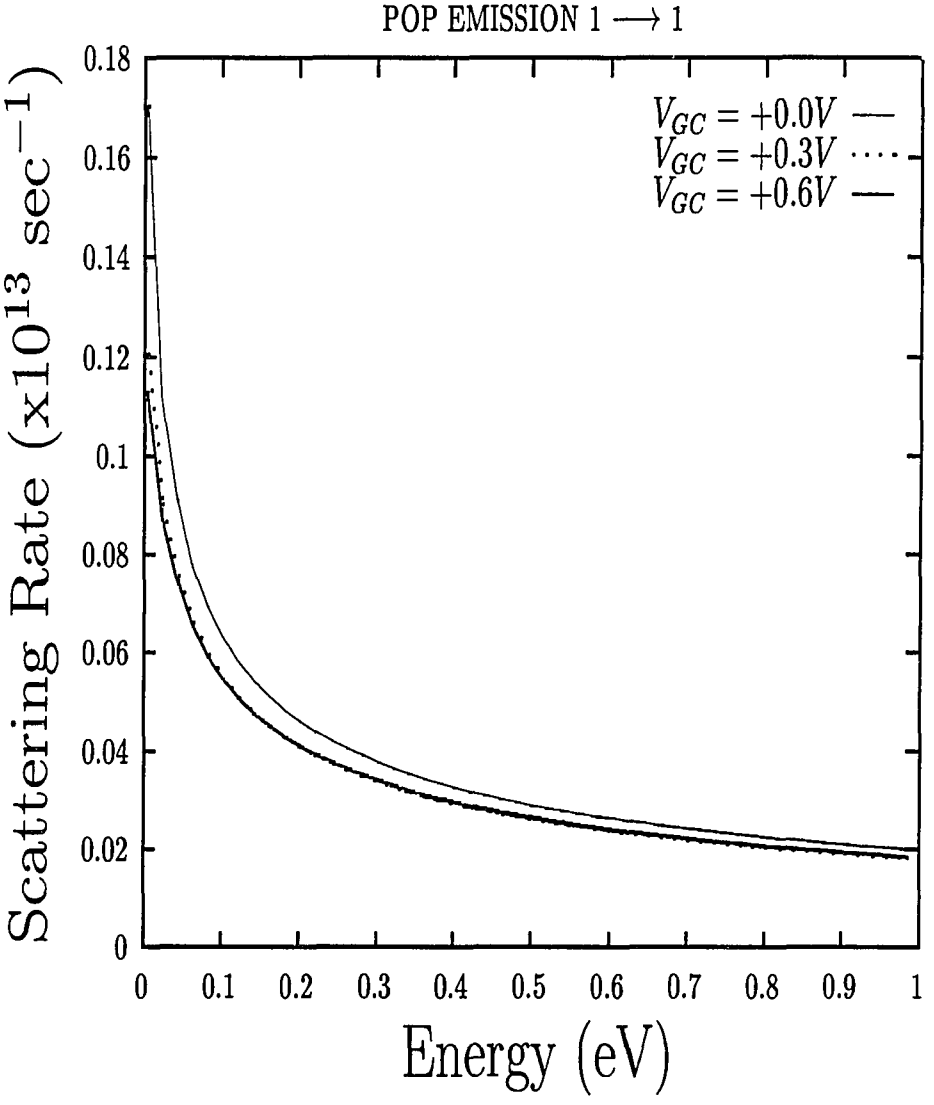

Figure 4.22: POP scattering rates as a function of energy for 1 to 1 emission mechanism.

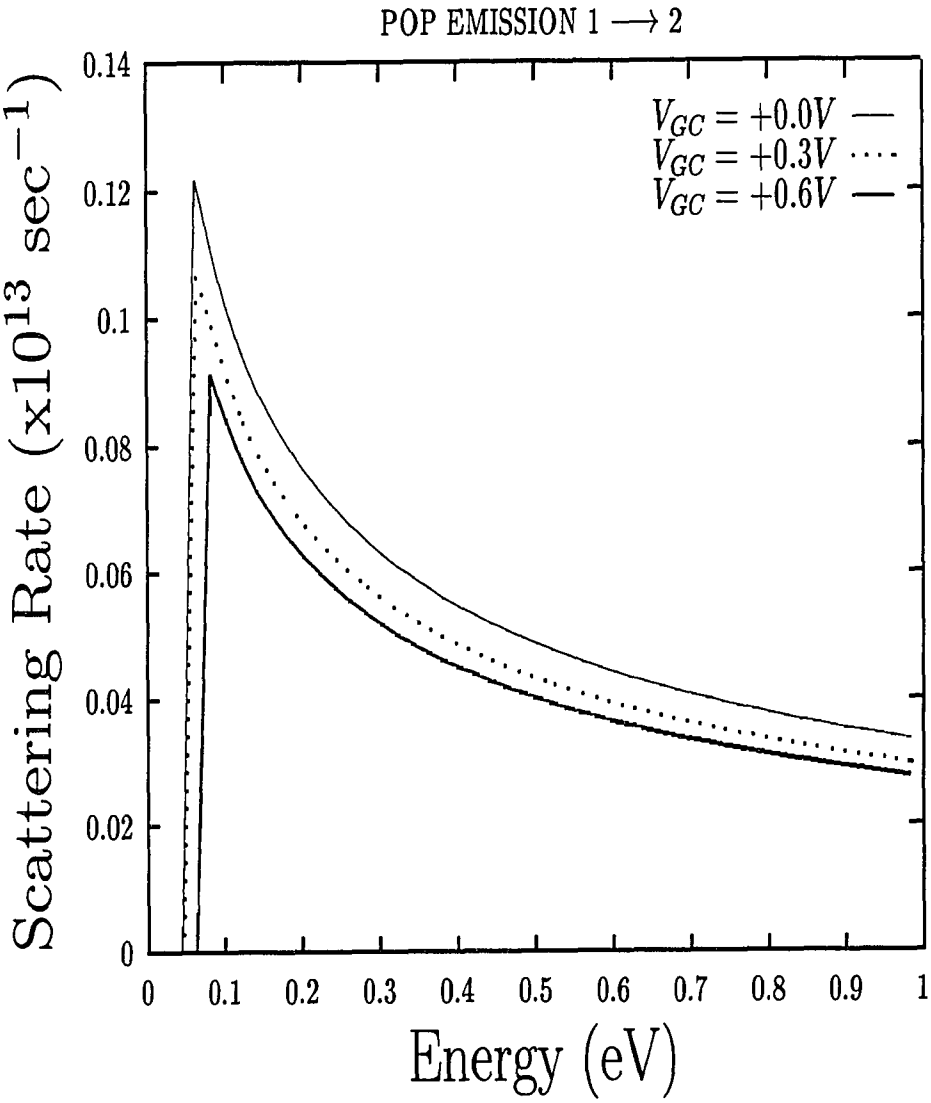

Figure 4.23: POP scattering rates as a function of energy for 1 to 2 emission mechanism.

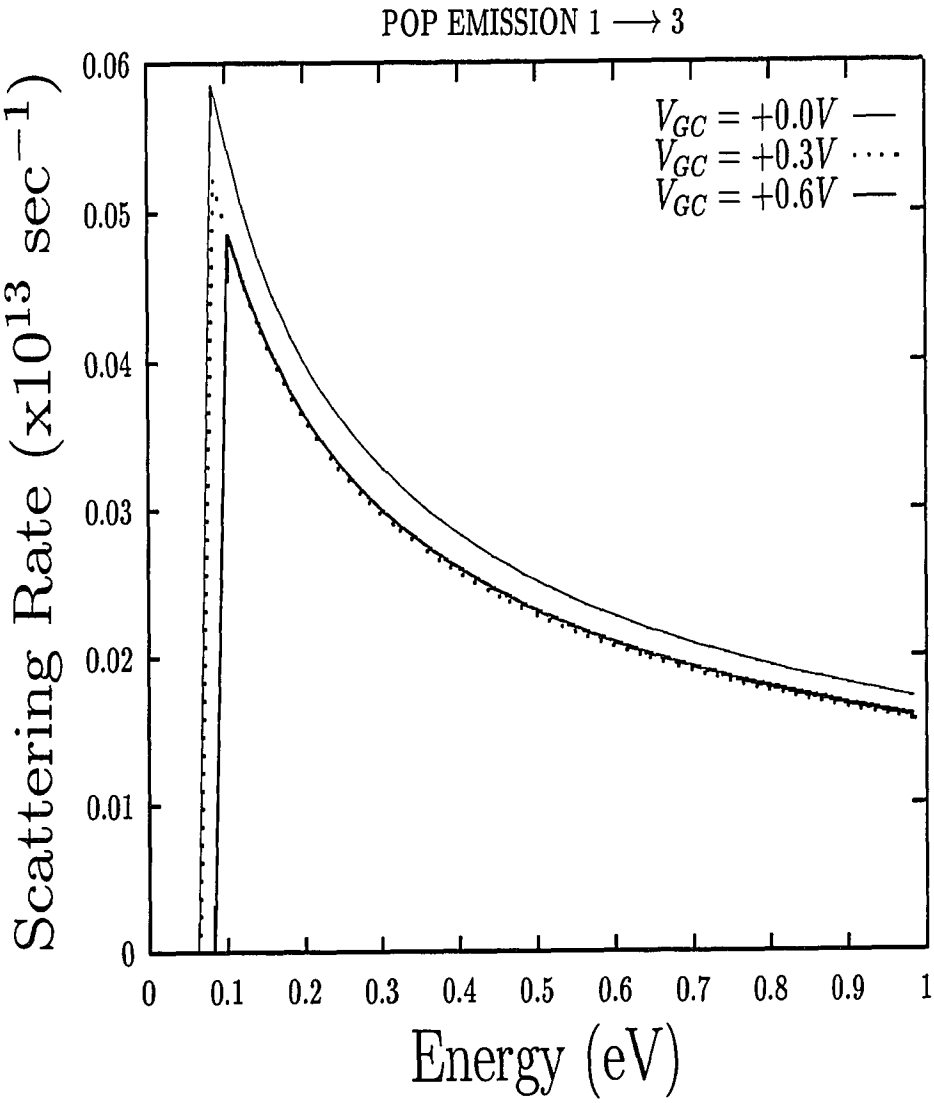

Figure 4.24: POP scattering rates as a function of energy for 1 to 3 emission mechanism.

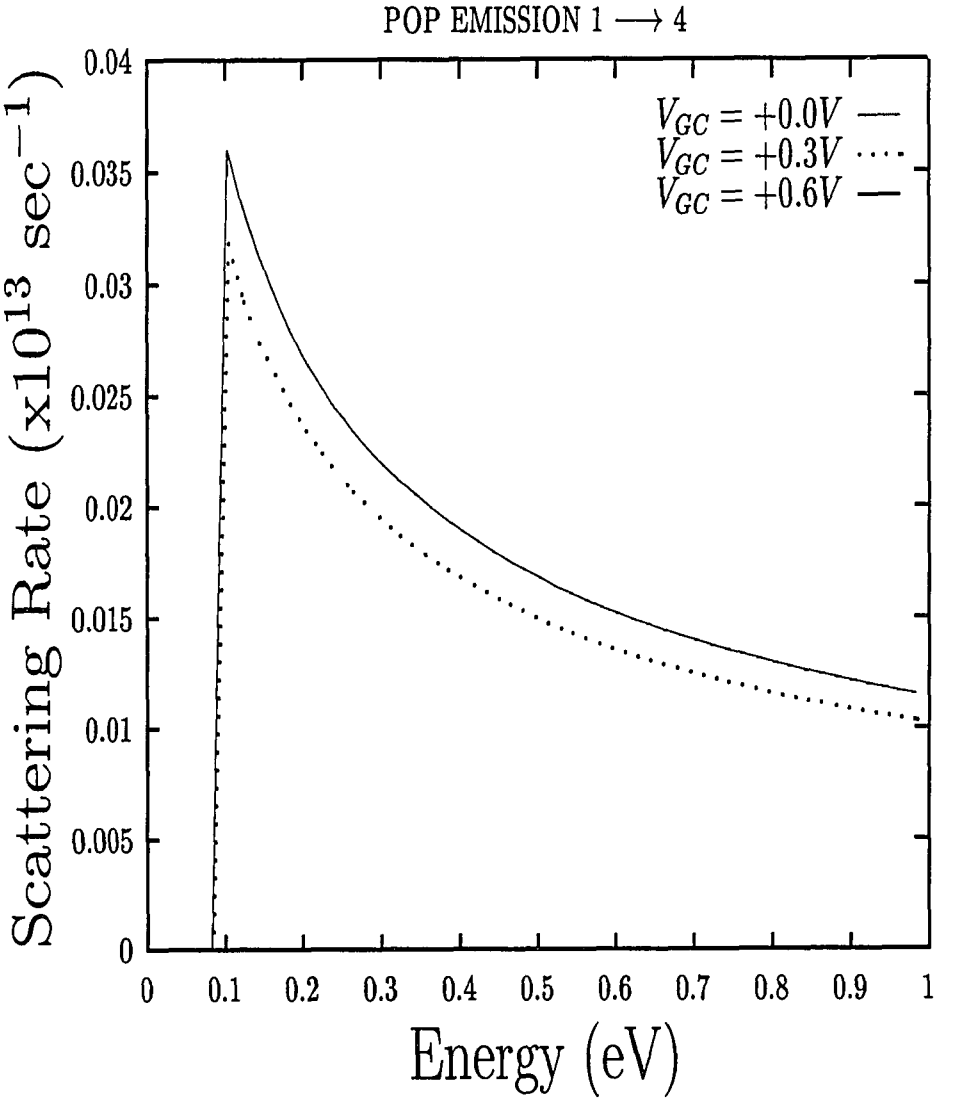

Figure 4.25: POP scattering rates as a function of energy for 1 to 4 emission mechanism.

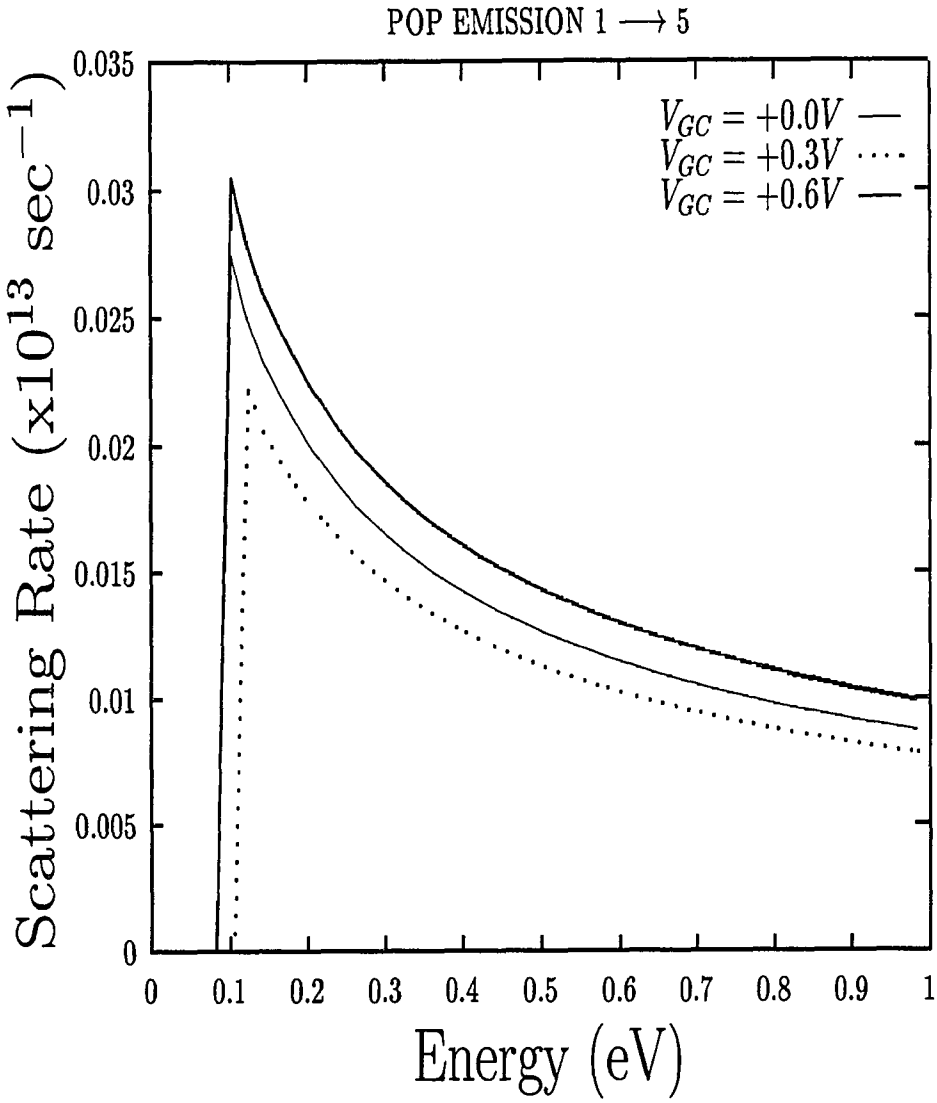

Figure 4.26: POP scattering rates as a function of energy for 1 to 5 emission mechanism.

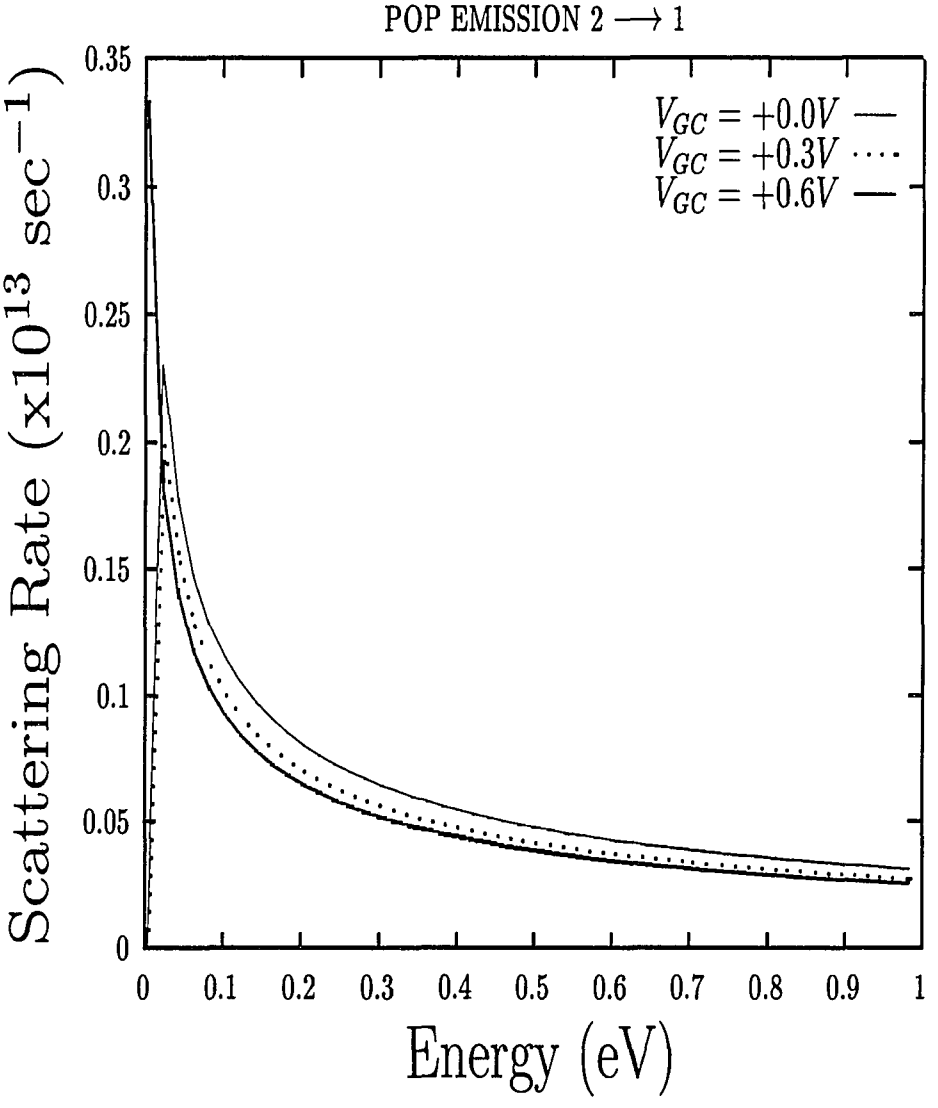

Figure 4.27: POP scattering rates as a function of energy for 2 to 1 emission mechanism.

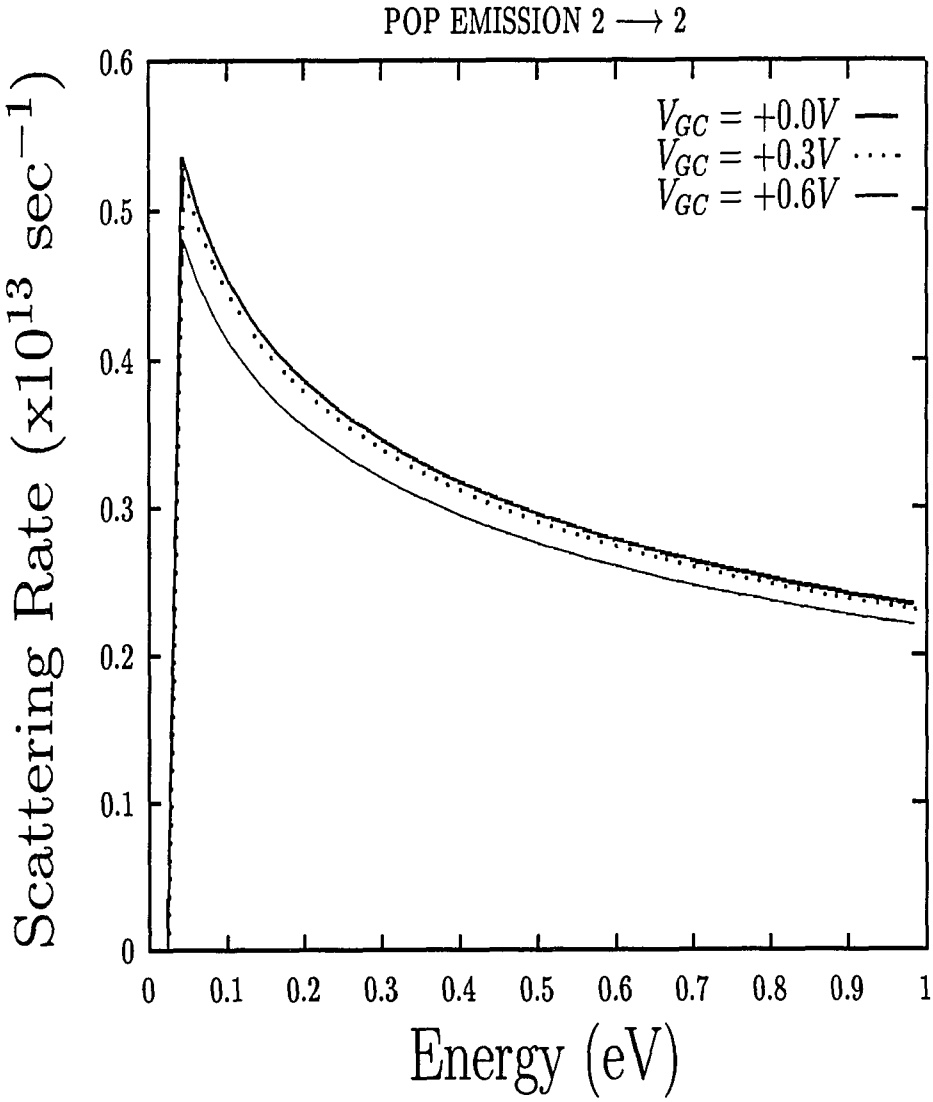

Figure 4.28: POP scattering rates as a function of energy for 2 to 2 emission mechanism.

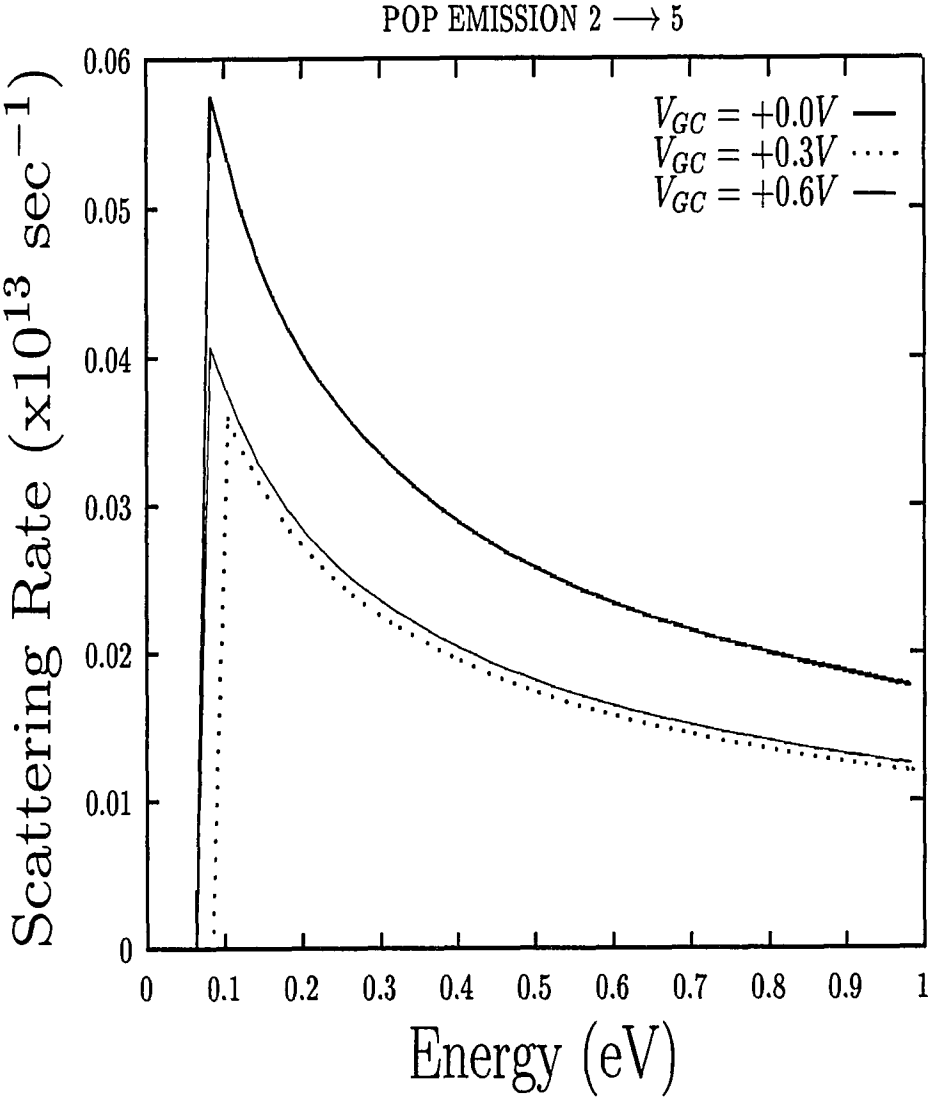

Figure 4.29: POP scattering rates as a function of energy for 2 to 5 emission mechanism.

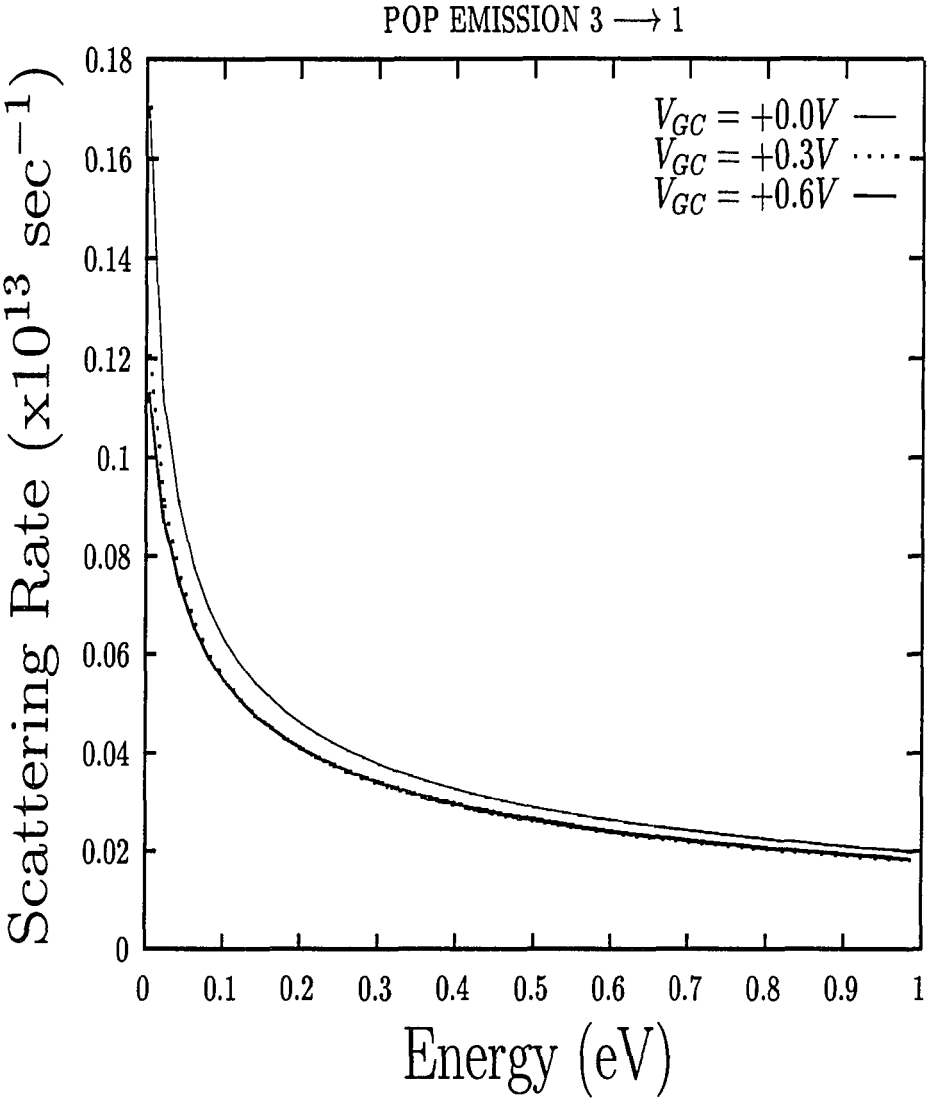

Figure 4.30: POP scattering rates as a function of energy for 3 to 1 emission mechanism.

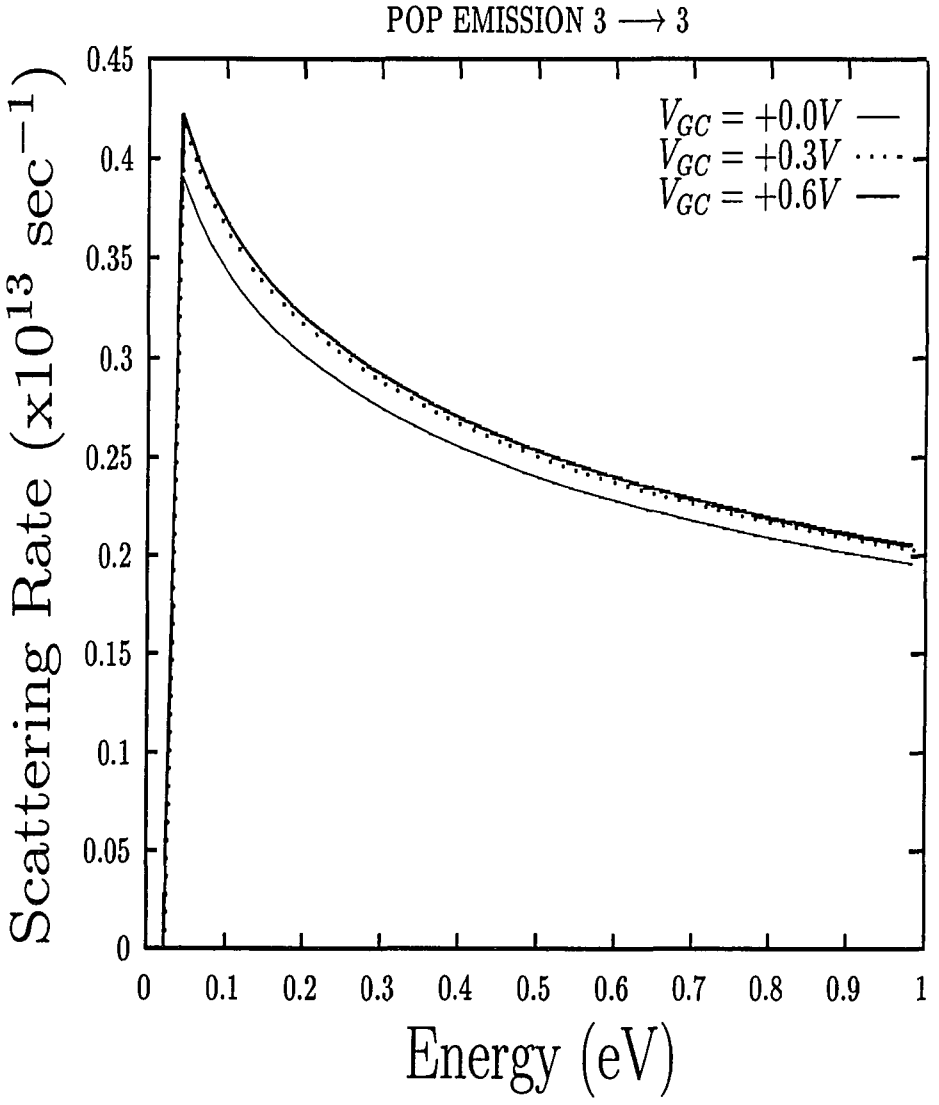

Figure 4.31: POP scattering rates as a function of energy for 3 to 3 emission mechanism.

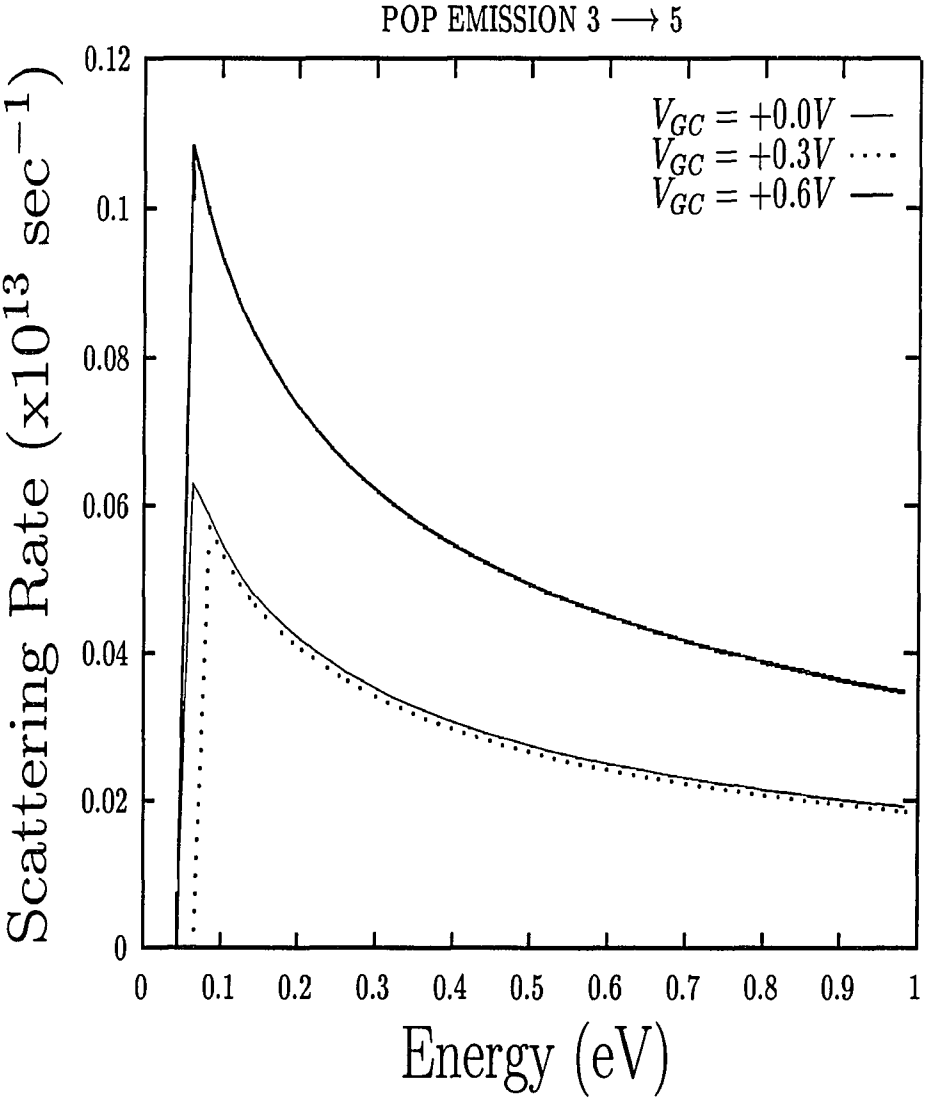

Figure 4.32: POP scattering rates as a function of energy for 3 to 5 emission mechanism.

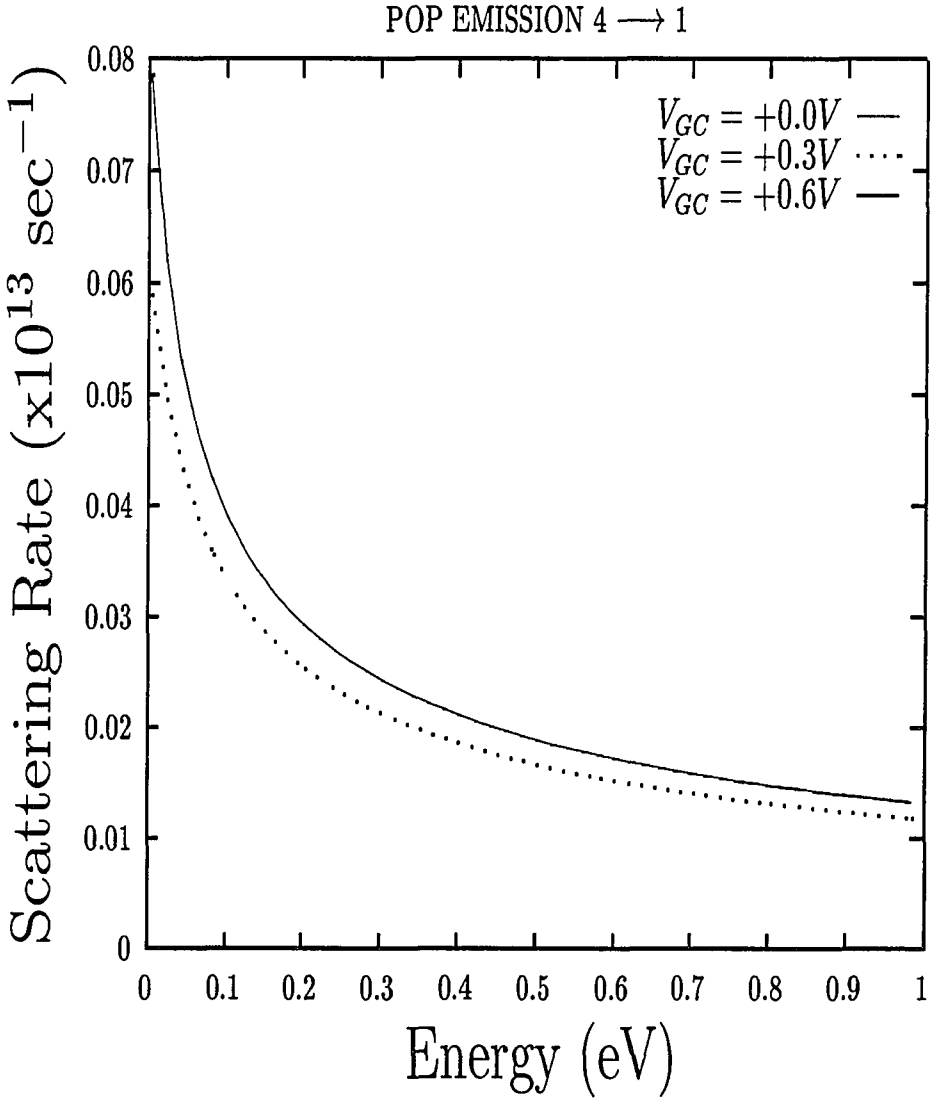

Figure 4.33: POP scattering rates as a function of energy for 4 to 1 emission mechanism.

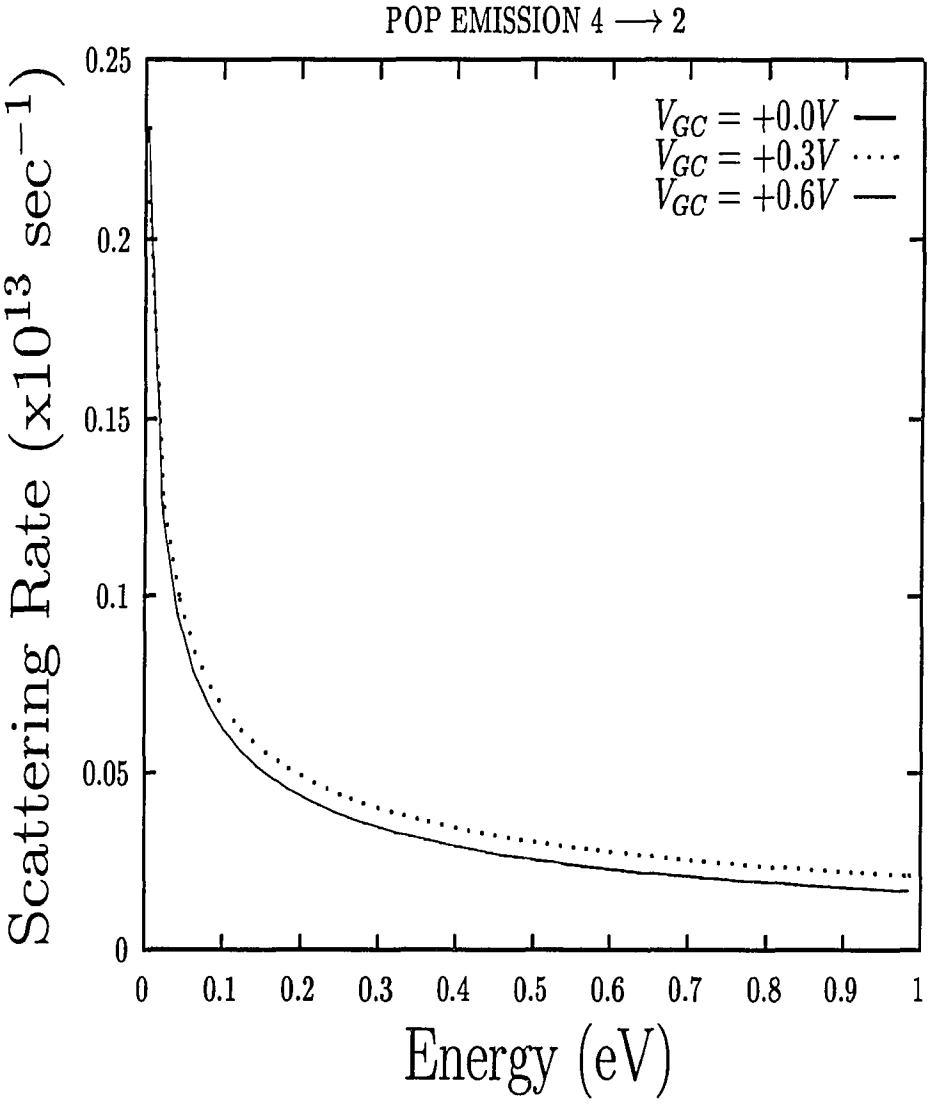

Figure 4.34: POP scattering rates as a function of energy for 4 to 2 emission mechanism.

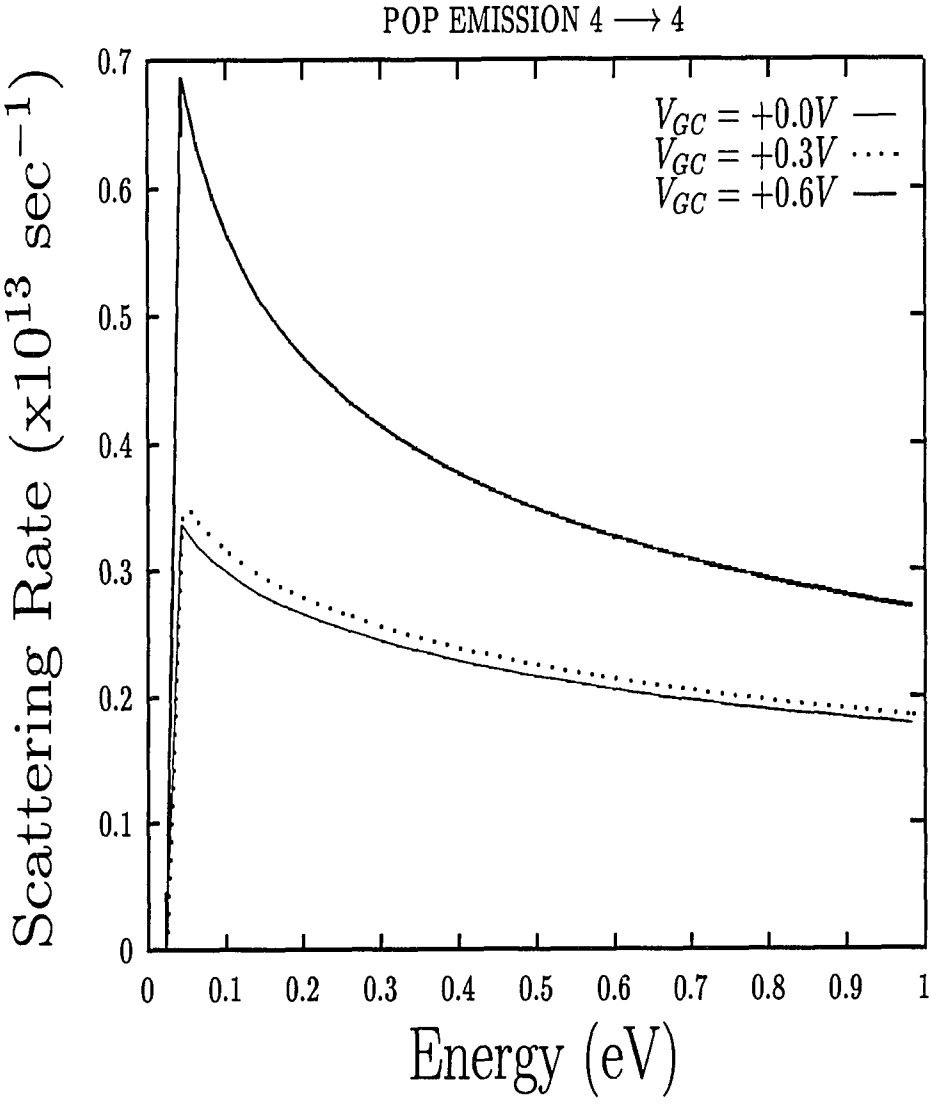

Figure 4.35: POP scattering rates as a function of energy for 4 to 4 emission mechanism.

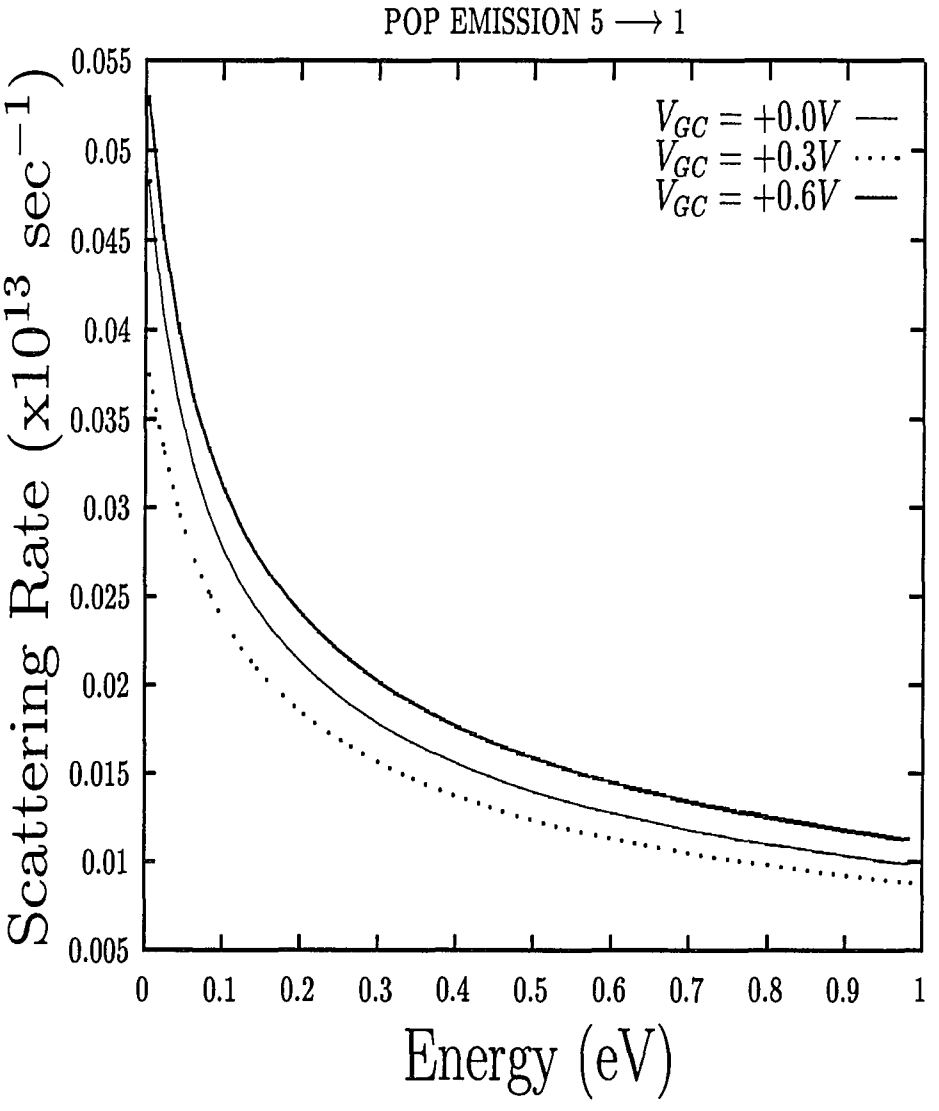

Figure 4.36: POP scattering rates as a function of energy for 5 to 1 emission mechanism.

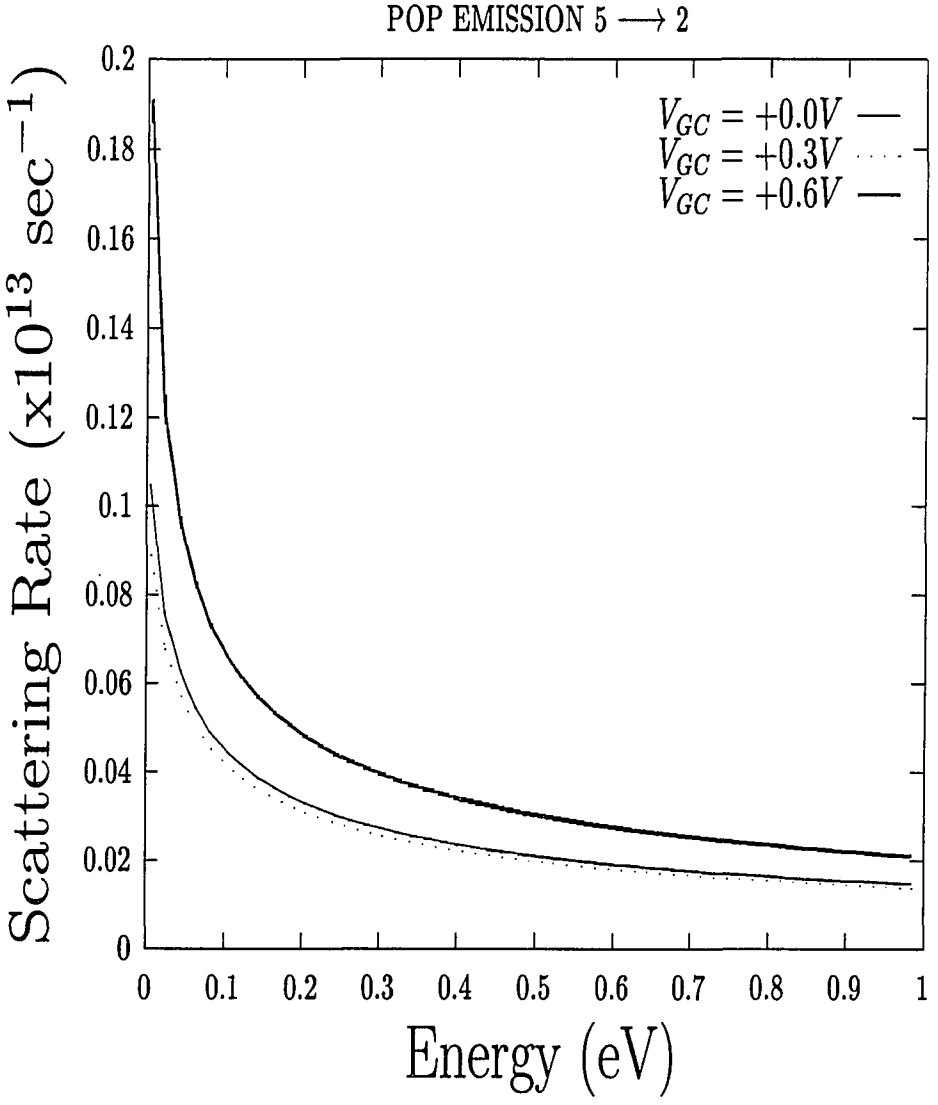

Figure 4.37: POP scattering rates as a function of energy for 5 to 2 emission mechanism.

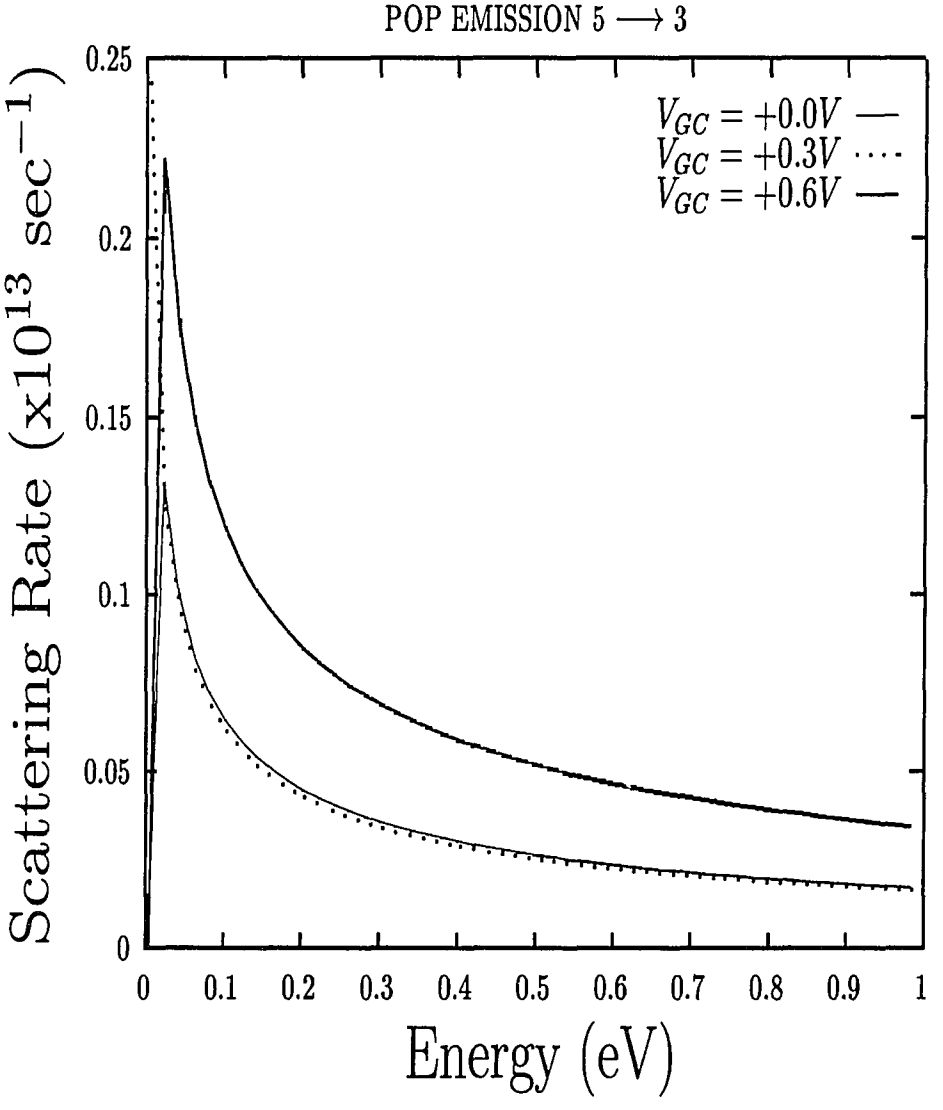

Figure 4.38: POP scattering rates as a function of energy for 5 to 3 emission mechanism.

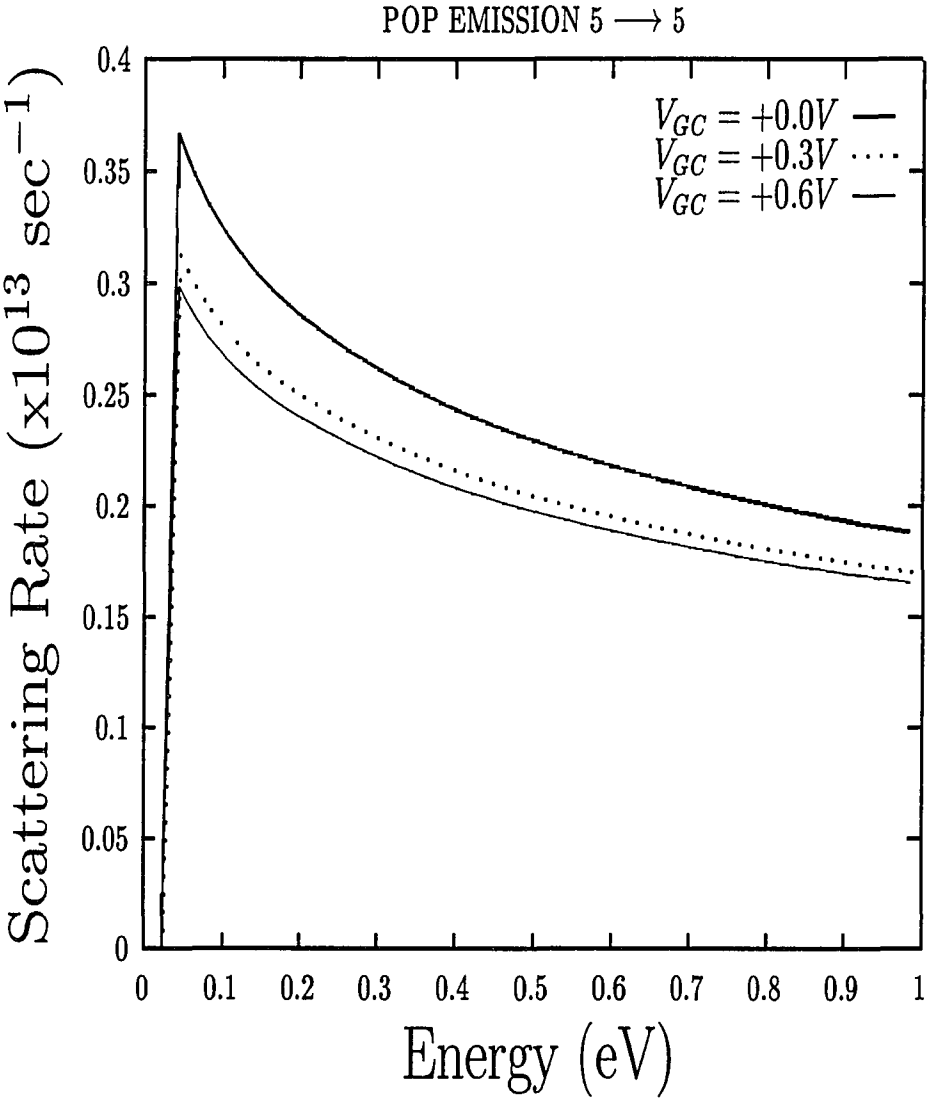

Figure 4.39: POP scattering rates as a function of energy for 5 to 5 emission mechanism.

Scattering from m^{th} subband to m^{th} subband	Maximum difference in % between the source and the drain at the same incident energy
1 $\longrightarrow$ 1	24
2 $\longrightarrow$ 2	13
3 $\longrightarrow$ 3	10
4 $\longrightarrow$ 4	109
5 $\longrightarrow$ 5	24

Table 4.5: Maximum difference between the source and the drain in the scattering rate for various AP intrasubband absorption and emission mechanisms.

4.3 AP scattering mechanism

The intrasubband scattering rate for AP (via deformation potential D) is determined for the m^{th} subband using equation (3.29), for an electron with initial wave vector, k_0. The scattering rate for various intrasubband AP absorption and emission mechanisms are shown in Figures 4.40 through 4.49, respectively, for the three channel locations corresponding to $V_{GC} = +0.0V, V_{GC} = +0.3V$ and $V_{GC} = +0.6V$. Table 4.5 shows the maximum difference in the rates for this scattering mechanism.

4.3.1 Qualitative observations

The scattering rates at 300°K are two orders of magnitude smaller than that of the corresponding POP scattering mechanisms. The variation of rate with the incident energy follows the behavior stated in [1].

As illustrated in Figures 4.40 through 4.49, the rates at the drain end are smaller than that at the source end for both the mechanisms. In these cases, the difference between the scattering rates between the source and the drain does not decrease with the incident energy unlike the POP mechanisms. It can also be observed that as the incident energy

increases, the scattering rates for the AP absorption mechanisms decrease whereas for AP emission, the scattering rates increase with increasing energy. Even though, the scattering rates in these cases show a wide variation along the channel, due to their very low rates they do not influence the transport properties significantly.

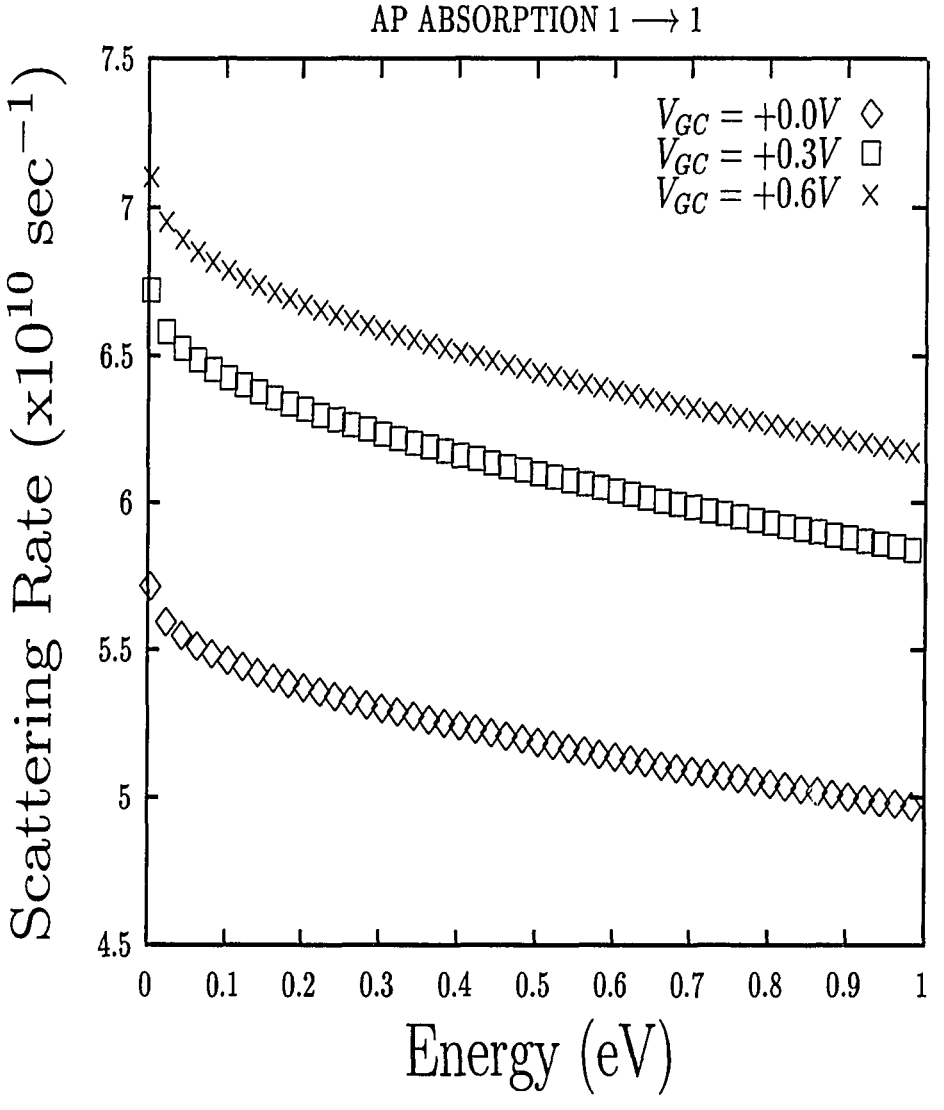

Figure 4.40: AP scattering rates as a function of energy for 1 to 1 absorption mechanism.

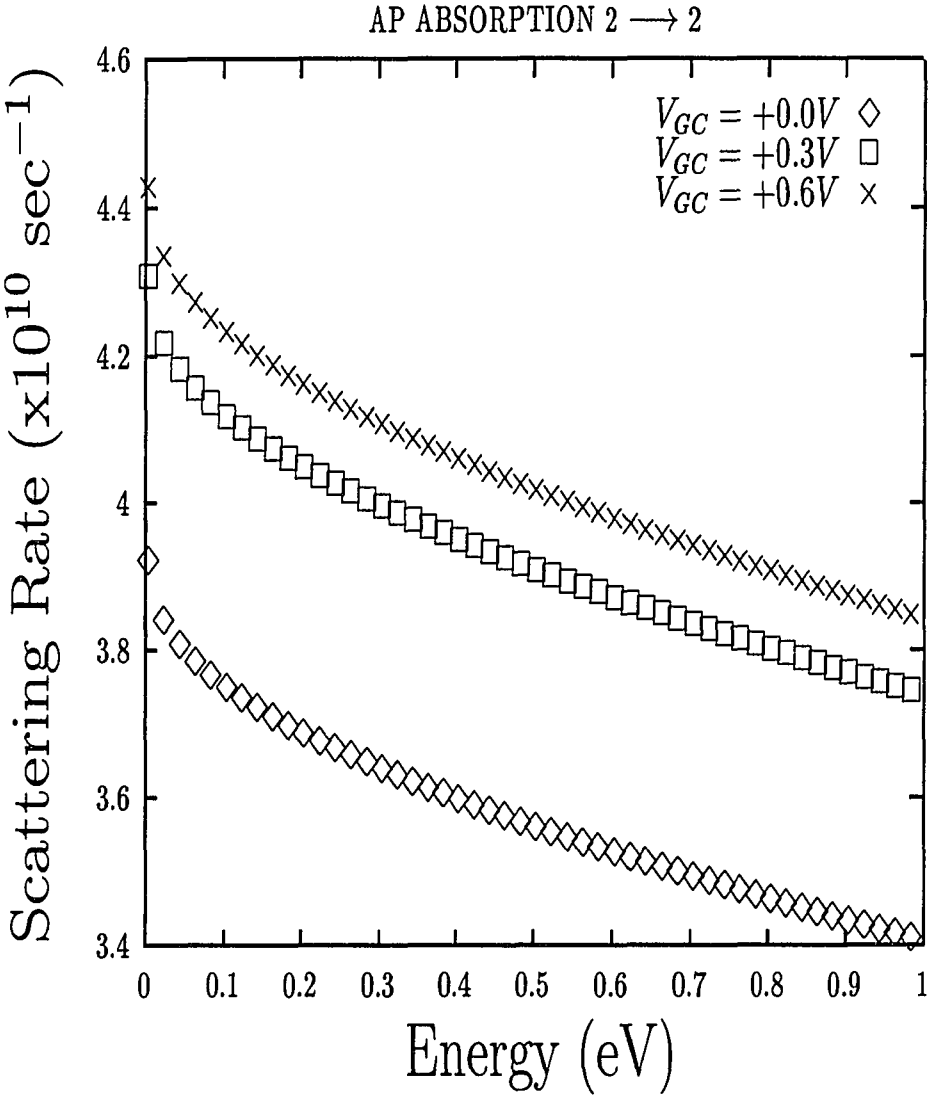

Figure 4.41: AP scattering rates as a function of energy for 2 to 2 absorption mechanism.

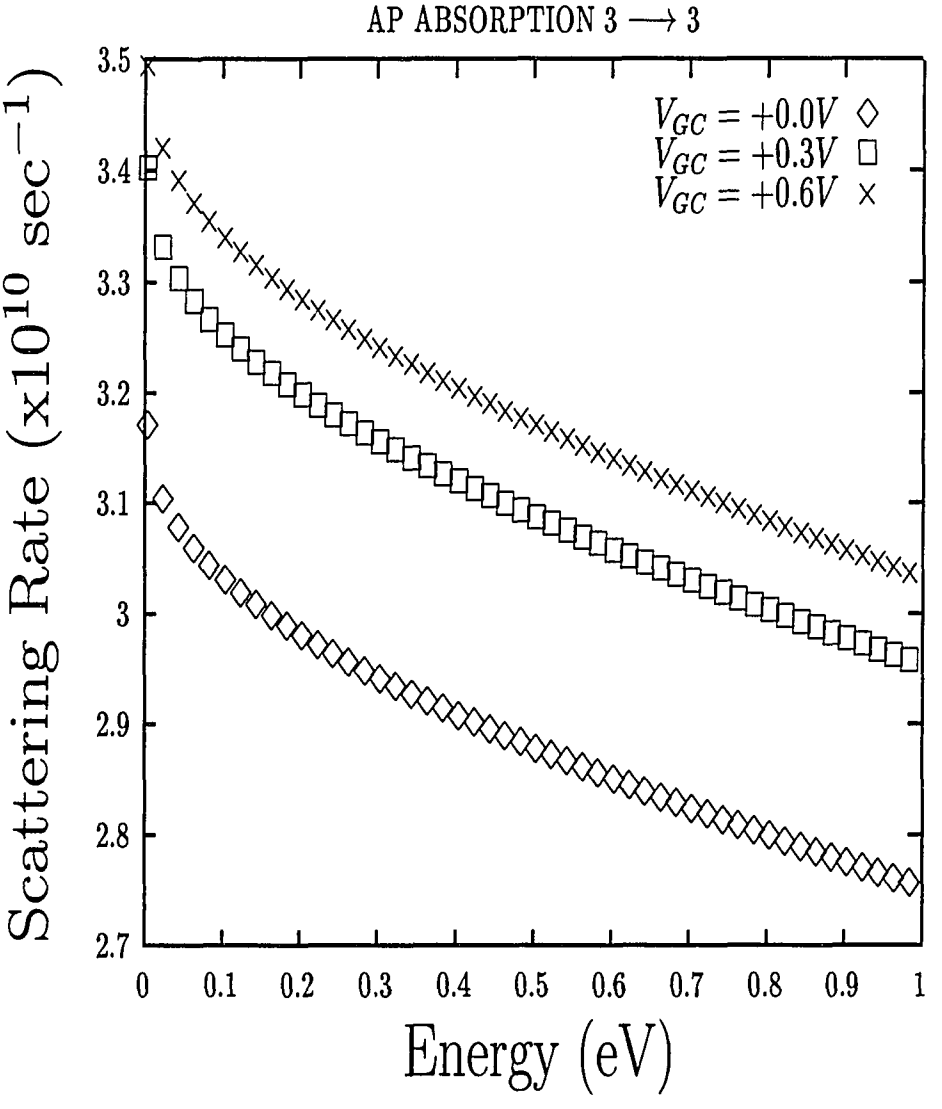

Figure 4.42: AP scattering rates as a function of energy for 3 to 3 absorption mechanism.

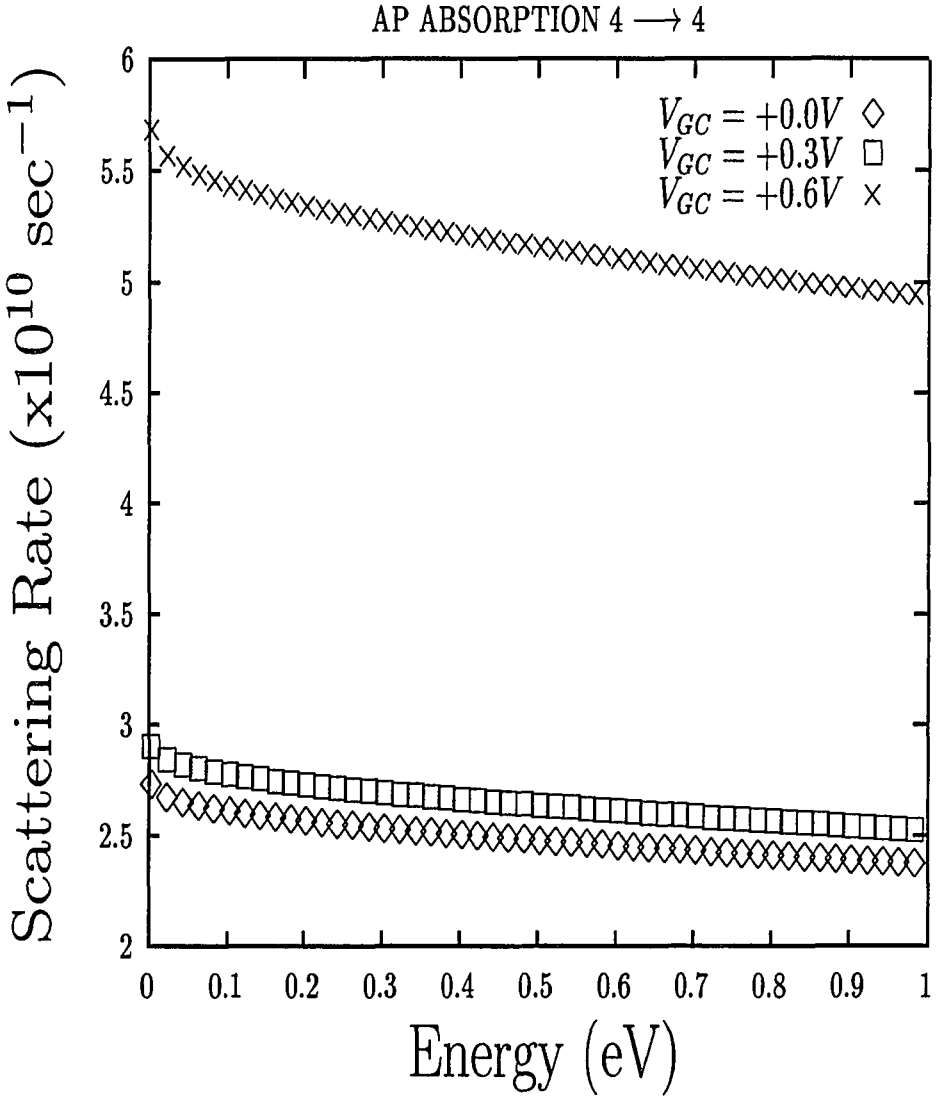

Figure 4.43: AP scattering rates as a function of energy for 4 to 4 absorption mechanism.

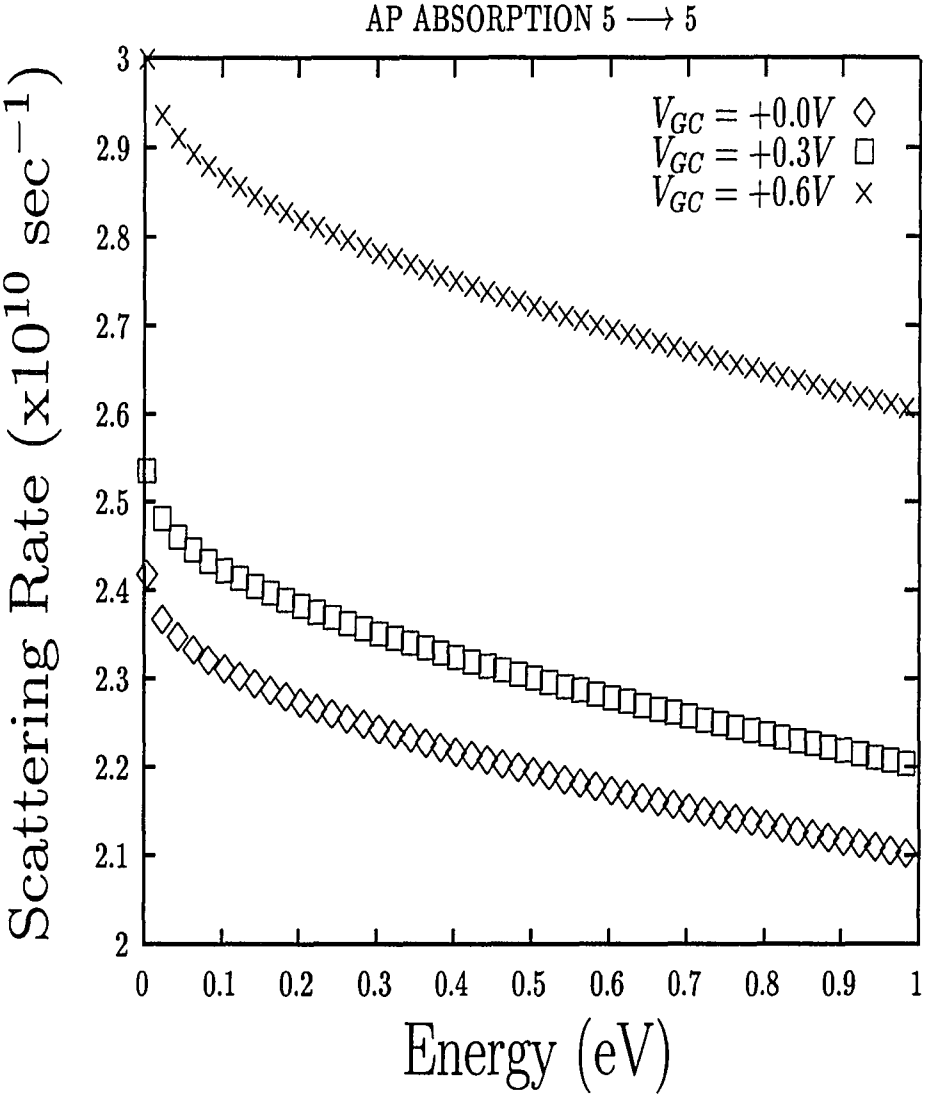

Figure 4.44: AP scattering rates as a function of energy for 5 to 5 absorption mechanism.

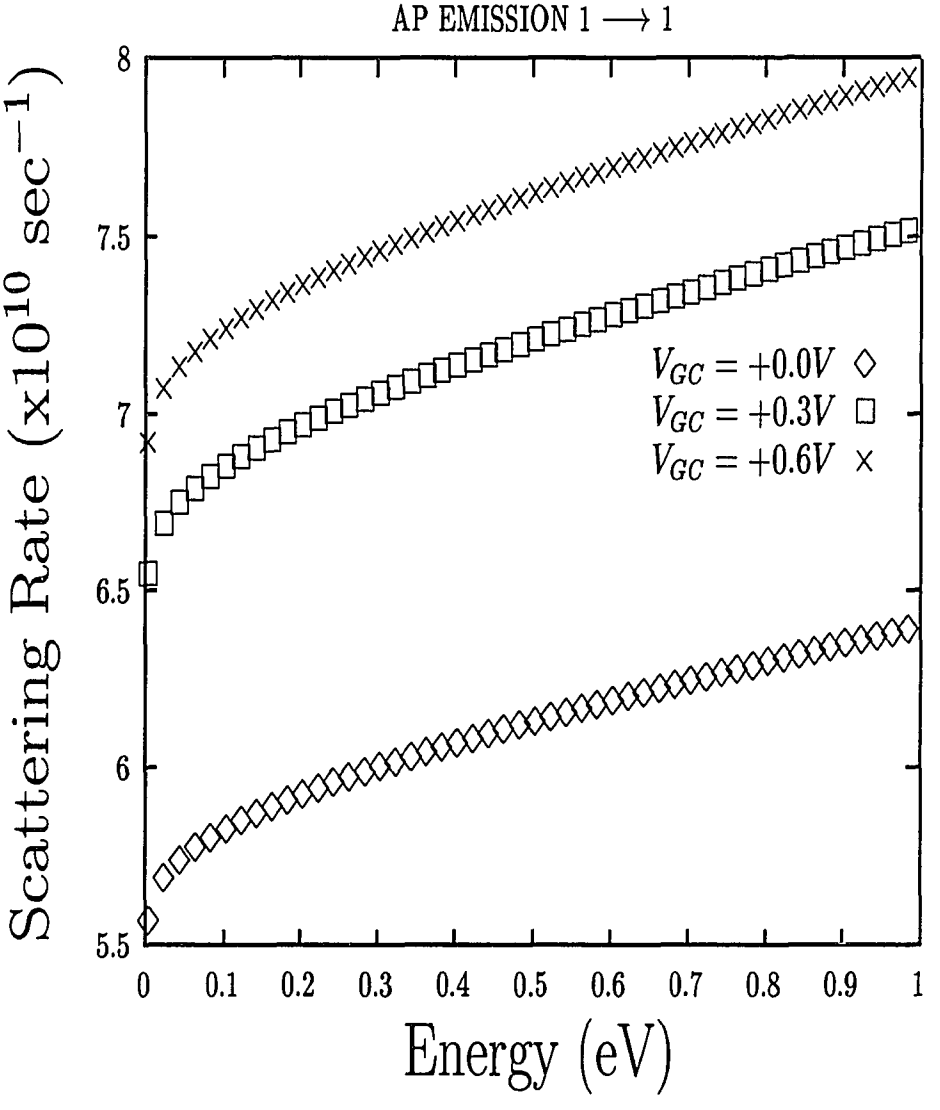

Figure 4.45: AP scattering rates as a function of energy for 1 to 1 emission mechanism.

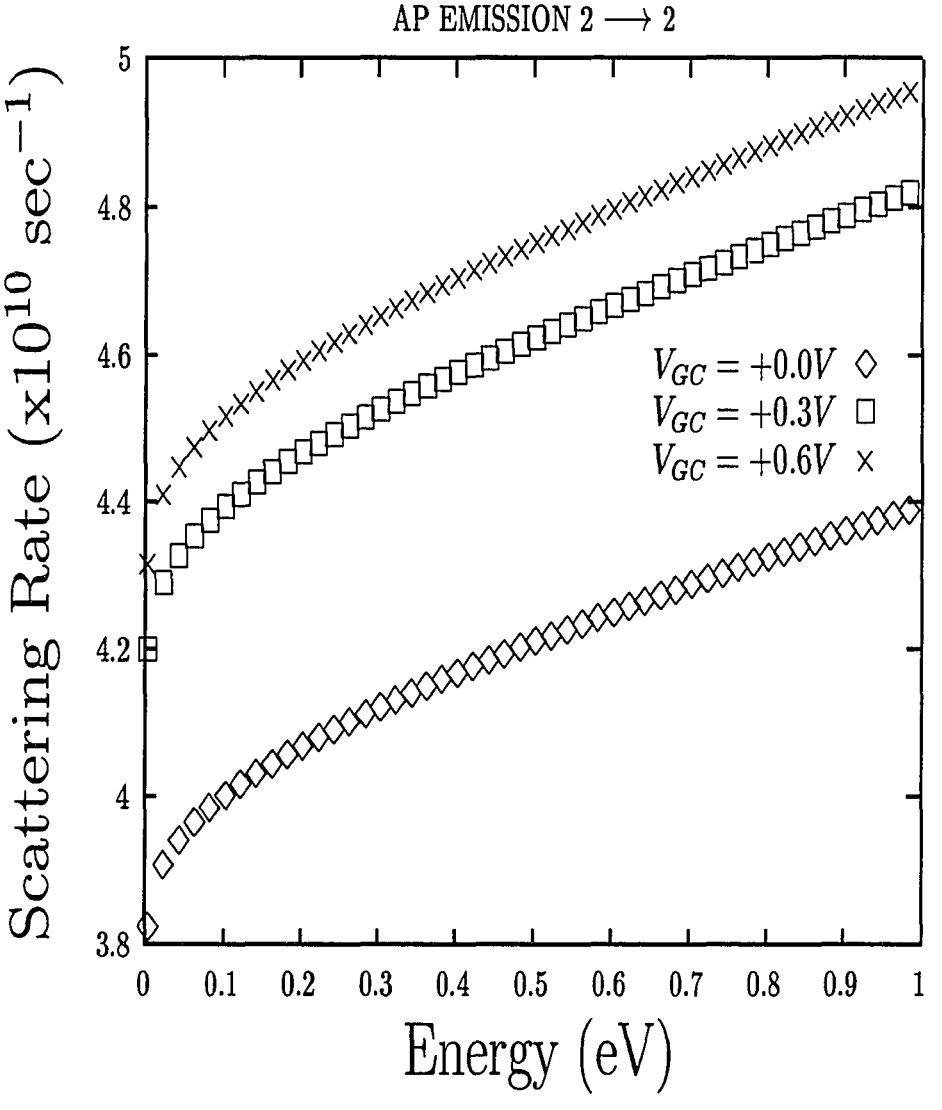

Figure 4.46: AP scattering rates as a function of energy for 2 to 2 emission mechanism.

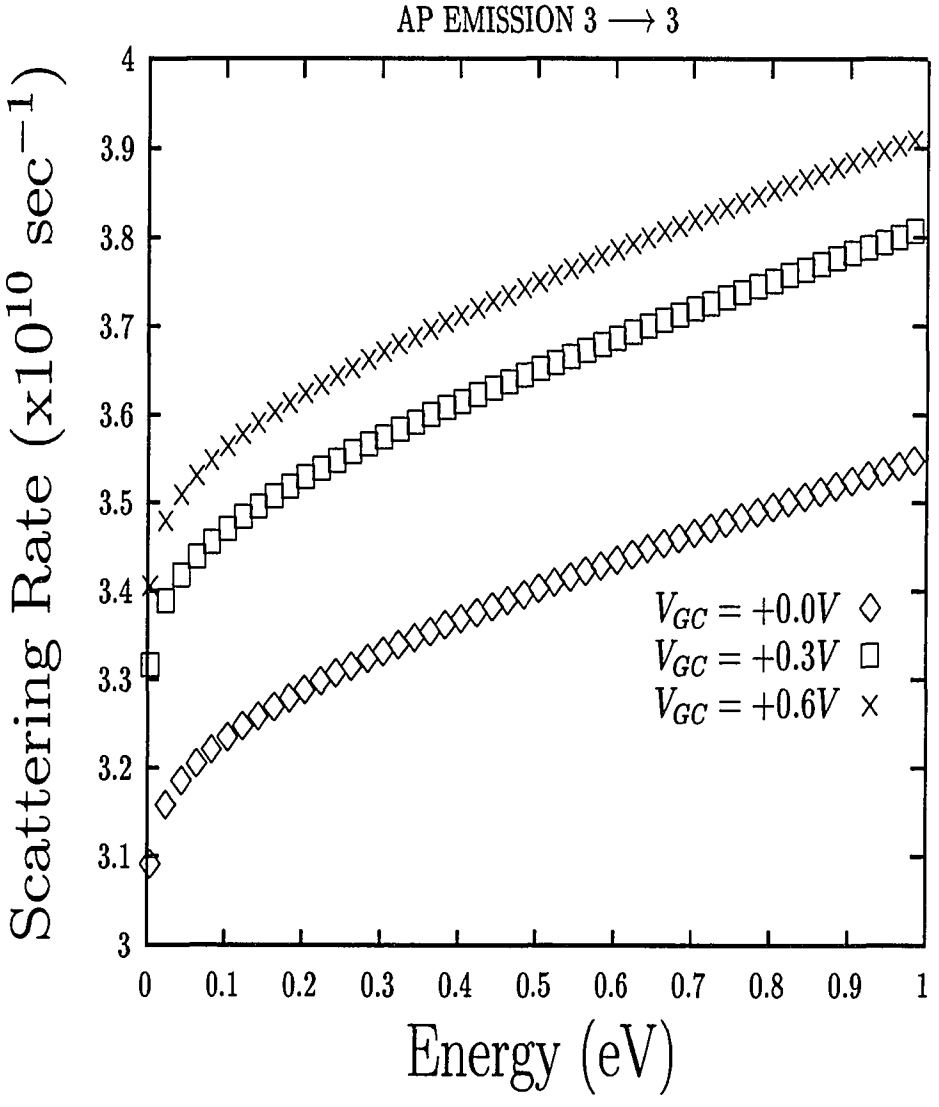

Figure 4.47: AP scattering rates as a function of energy for 3 to 3 emission mechanism.

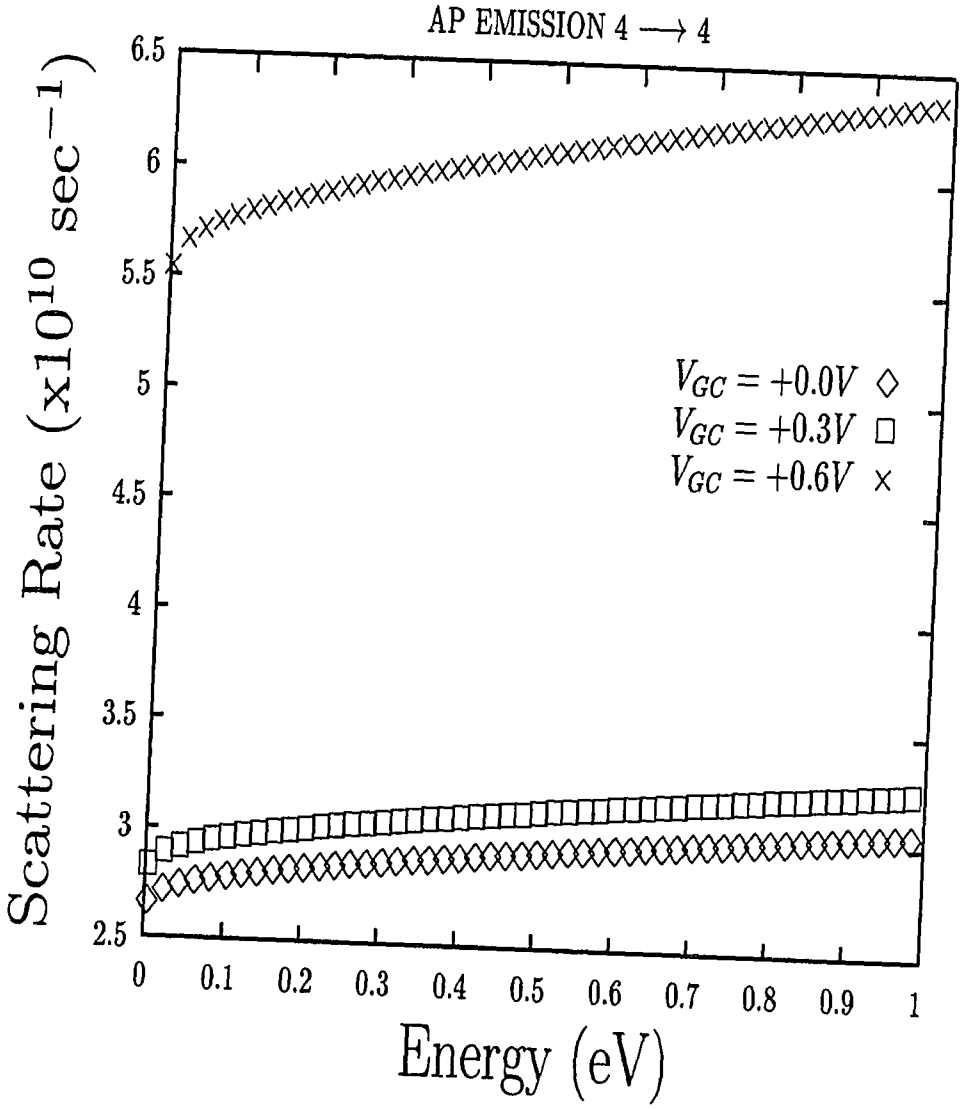

Figure 4.48: AP scattering rates as a function of energy for 4 to 4 emission mechanism.

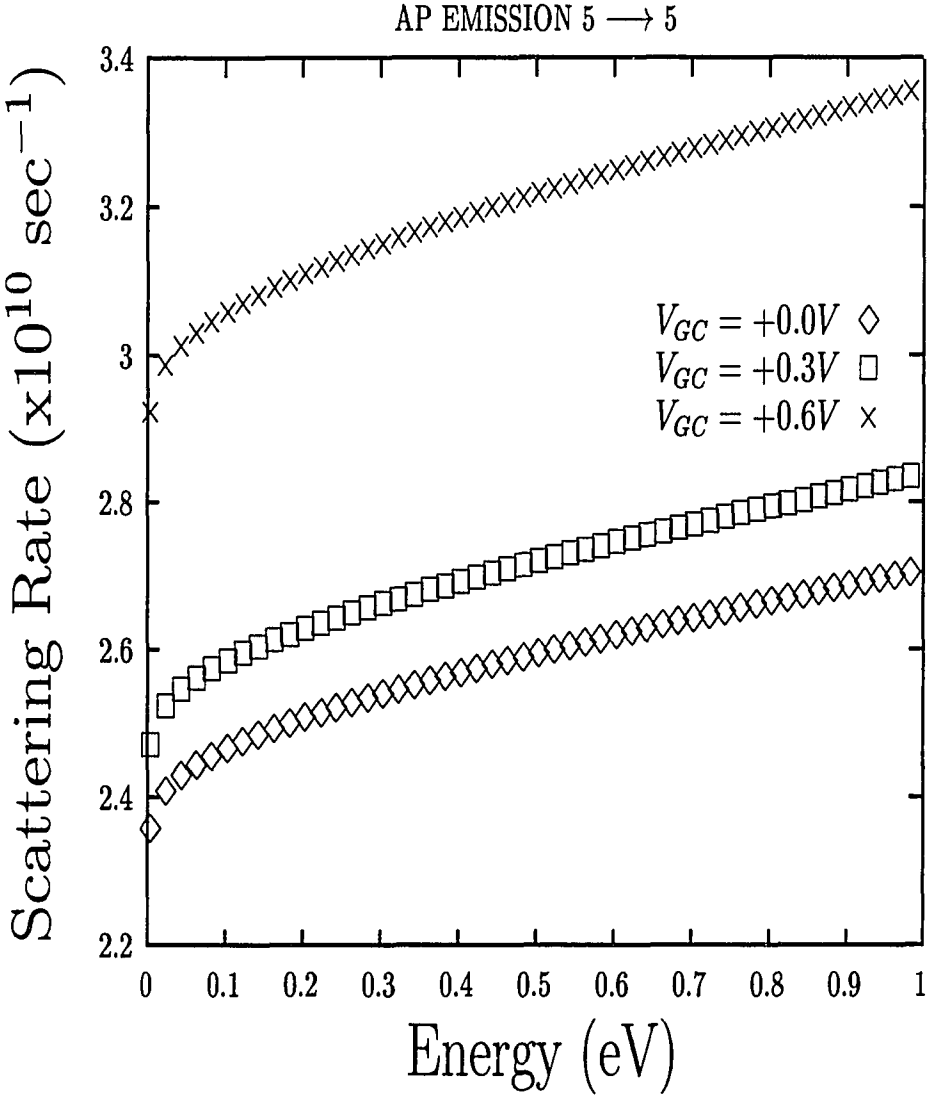

Figure 4.49: AP scattering rates as a function of energy for 5 to 5 emission mechanism.

Scattering from m^{th} subband to m^{th} subband	Maximum difference in % between the source and the drain at the same incident energy
1 $\longrightarrow$ 1	66
2 $\longrightarrow$ 2	98
3 $\longrightarrow$ 3	30
5 $\longrightarrow$ 5	133

Table 4.6: Maximum difference between the source and the drain in the scattering rate for various intrasubband impurity scattering mechanisms.

4.4 Impurity scattering mechanism

The intrasubband scattering rate for the impurity scattering mechanism is determined for the m^{th} subband using equation (3.36). Figures 4.50 through 4.54 show the difference in the scattering rate at three locations along the channel, for various subbands, due to ionized impurity scattering. Table 4.6 shows the maximum difference in the rates for various intrasubband transitions due to ionized impurity scattering.

4.4.1 Qualitative observations

It can be observed that for the 1 $\longrightarrow$ 1 impurity scattering mechanism, the scattering rates, at the channel location where $V_{GC} = +0.3V$, are higher than the scattering rates at the source or at the drain. In the case of 2 $\longrightarrow$ 2 impurity scattering mechanism, the scattering rates at the drain are higher than the scattering rates at the source and a maximum difference of 98% has been observed. For 3 $\longrightarrow$ 3, 4 $\longrightarrow$ 4 and 5 $\longrightarrow$ 5 impurity scattering mechanisms, the scattering rates at the source end were found to be greater than the rates at the drain end. It has also been found that a maximum difference of 133% was observed for scattering for the 5 $\longrightarrow$ 5 mechanism. This high difference is attributed

to scattering rates being very low or being almost absent for the channel locations where $V_{GC} = +0.0V$ and $V_{GC} = +0.3V$ and being of significant value for the other channel location, where $V_{GC} = +0.6V$.

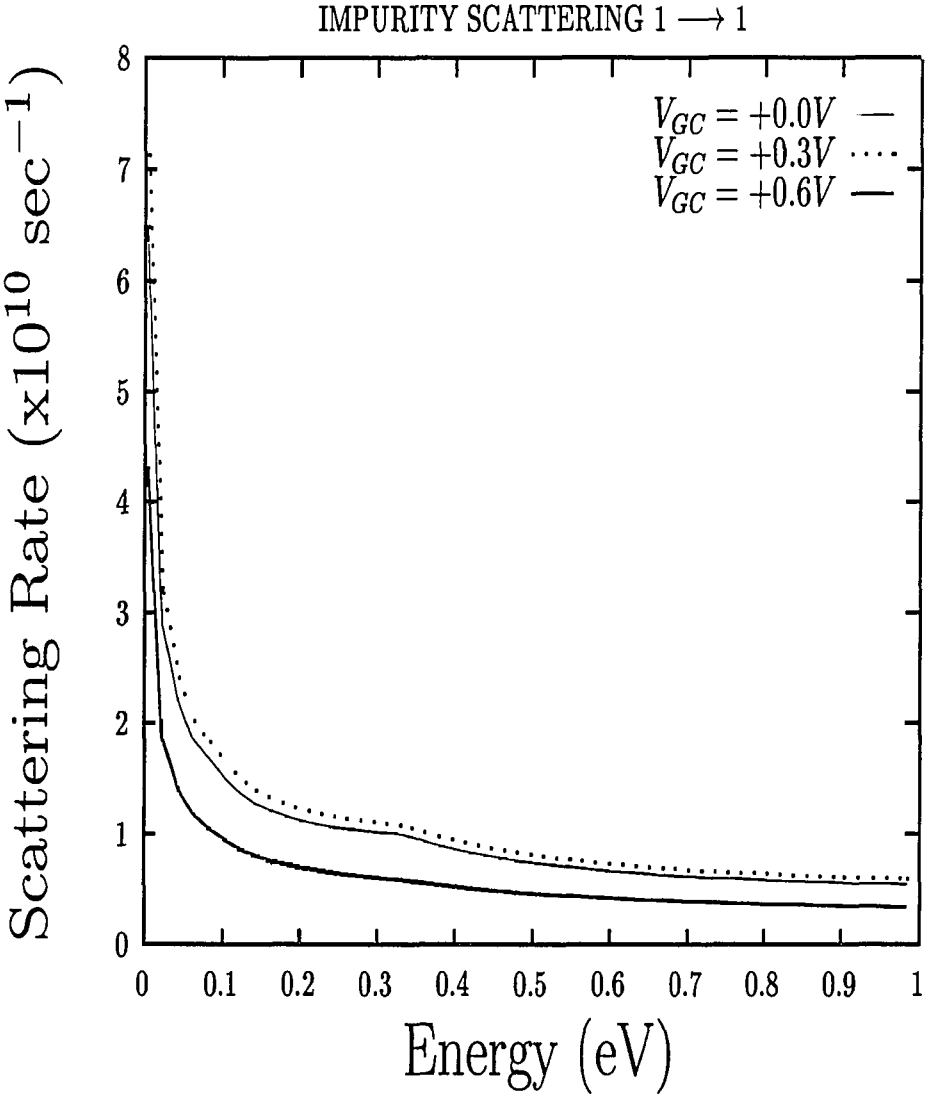

Figure 4.50: Impurity scattering rates as a function of energy for 1 to 1 emission mechanism.

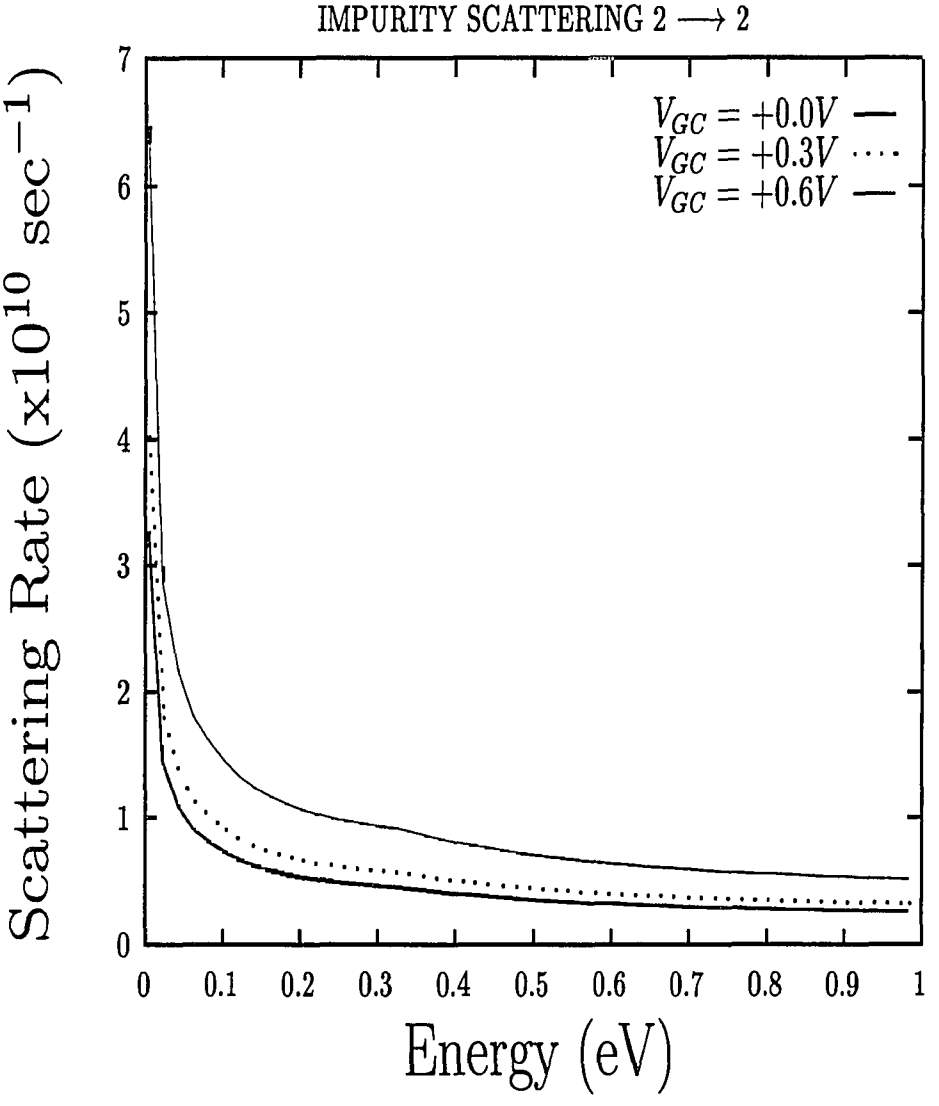

Figure 4.51: Impurity scattering rates as a function of energy for 2 to 2 emission mechanism.

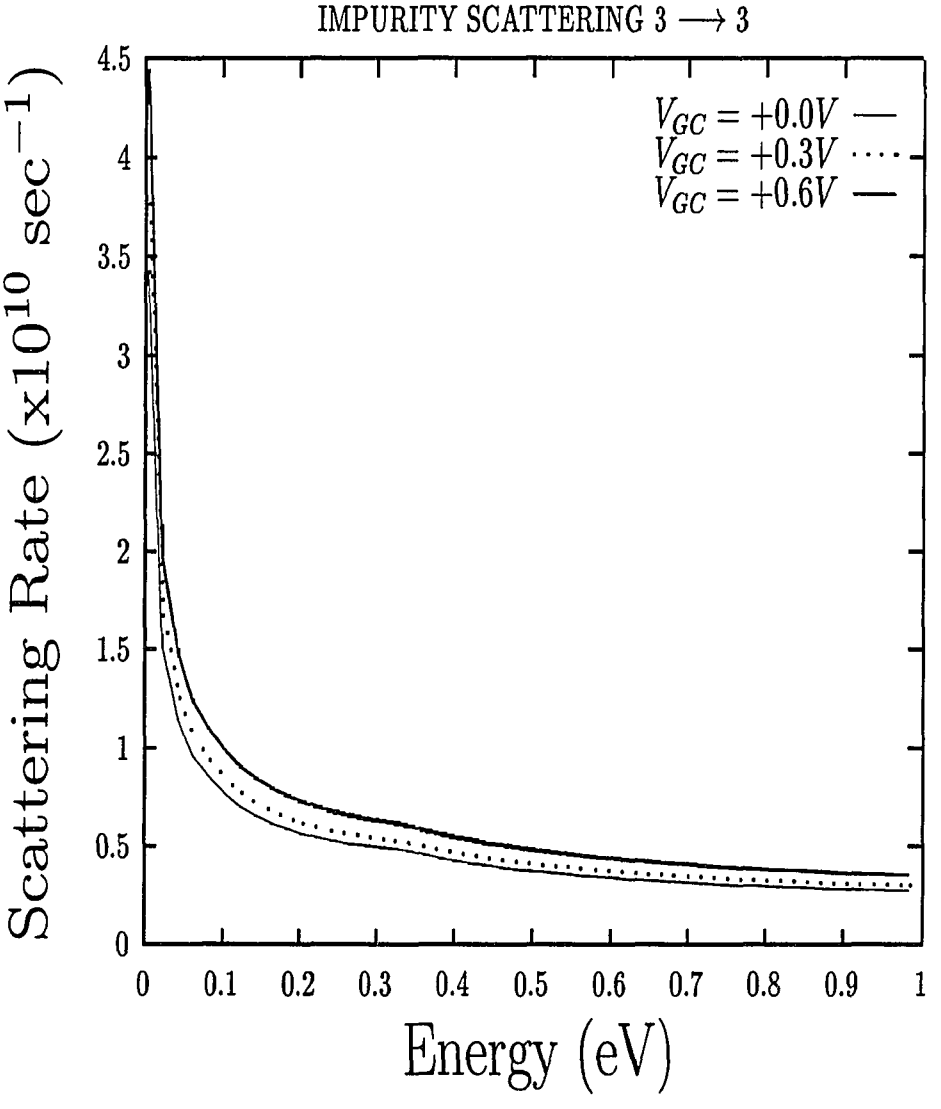

Figure 4.52: Impurity scattering rates as a function of energy for 3 to 3 emission mechanism.

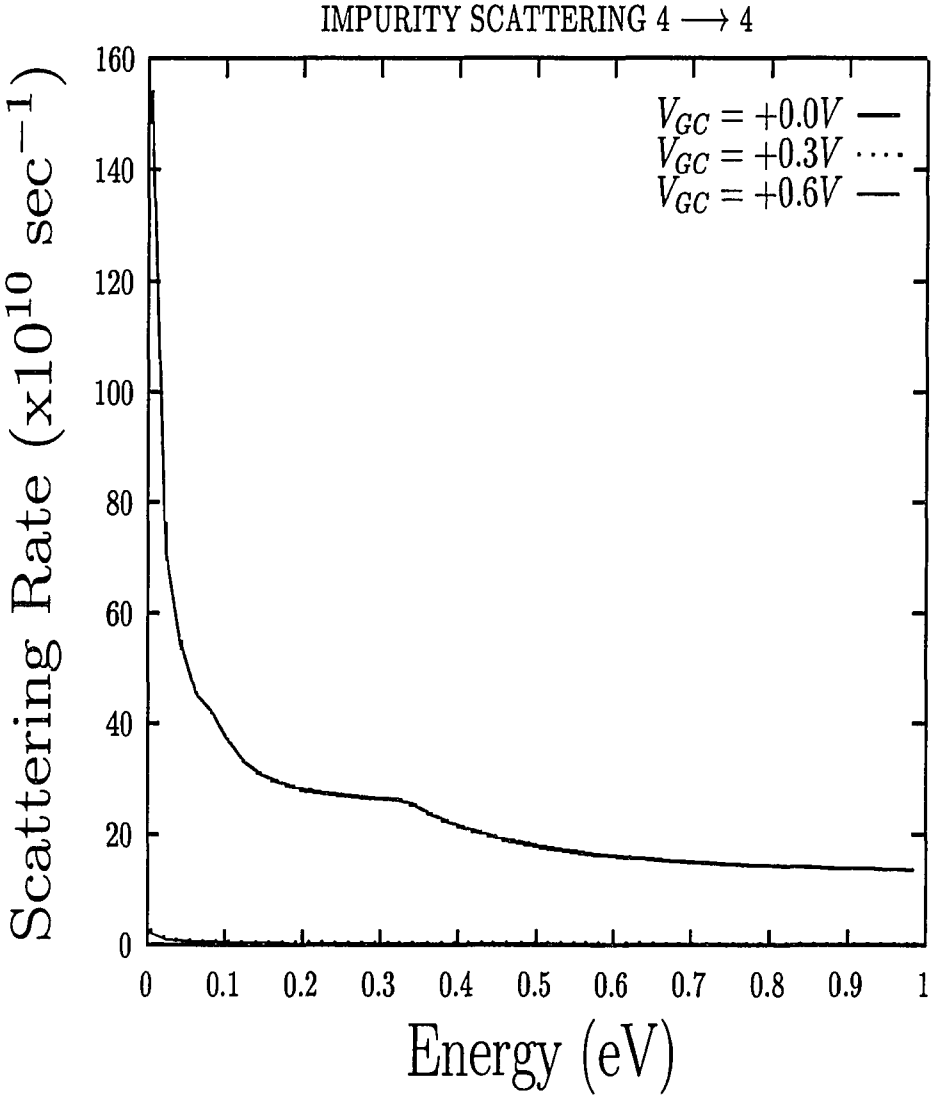

Figure 4.53: Impurity scattering rates as a function of energy for 4 to 4 emission mechanism.

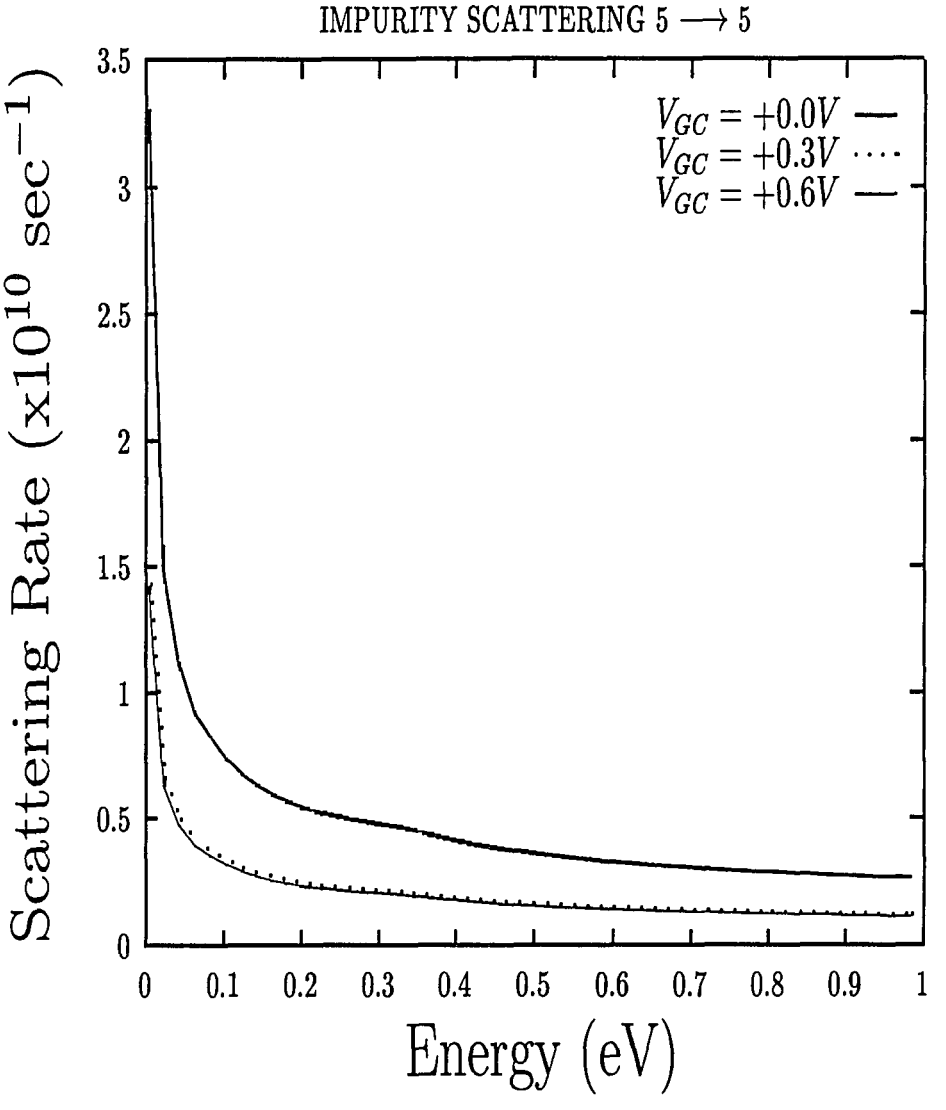

Figure 4.54: Impurity scattering rates as a function of energy for 5 to 5 emission mechanism.

4.5 Discussion

From the data presented in Sections 4.2 to 4.4, it is clear that the quantum confinement and hence the scattering rates for POP, AP and impurity scattering, significantly changes from the source to the drain with the scattering rate at the source usually being lower. The scattering rates for lower subbands (1 and 2) appears to exhibit variations of less than 98% for intrasubband and intersubband mechanisms (a 98% variation occurring for the impurity scattering mechanism from the second to the second subband). The influence of such a variation can introduce errors in the I-V characteristics. Also the scattering rate for $V_{GC} = +0.3V$ corresponding to a channel location in between the source and the drain, in most cases resembles the source end rates suggesting that if one wants to approximate and use a scattering rate value along the entire channel, it is better to choose the source value. Also in general, it is observed that POP rates are three orders of magnitude larger than the AP and impurity scattering rates. Thus, one should definitely consider the variation of rates for POP from the source to the drain, but the scattering rate variation along the channel for AP scattering does not influence the I-V characteristics significantly.

For higher operating temperatures and voltages, higher subbands may be occupied in which case the variation in scattering rate can be considerable, with some mechanisms being completely absent at the source, whereas they may be present at the drain. For lower temperatures and low operating voltages however, variations are introduced in the scattering rate from the source to the drain, by including the quantum confinement effect, as has been shown in the tables presented in Sections 4.2 to 4.4.

It is important to note a limitation of this study. To invoke gradual channel approximation, the operating point is confined to the ohmic region. 1-D Poisson is used to

obtain E_c profile and the Poisson-Schrödinger was not self-consistently solved. This will introduce errors into the results, which is believed to influence the results quantitatively, but not qualitatively. To address this problem, realistic E_c from Park et al [16], Ng et al [15] and Ferry et al [5] were obtained and analyzed. But the conduction band edge versus position profile was found to be unsuitable for the work.

As discussed in sections 4.2 and 4.4, the scattering rates exhibit a wide variation along the channel for both the POP, AP and impurity mechanisms at 300°K. For higher temperature operations, and other operating conditions especially in the saturation regime, the variation can be more pronounced. Unfortunately, a 1-D Poisson solver such as the FISH1D cannot be employed for such conditions due to inapplicability of gradual channel approximation.

The scattering rates directly determine the macroscopic transport properties such as the mobilities, the diffusion coefficients, the relaxation times and the energy dissipation parameters. A variation in the rates along the channel by a range, as has been shown in Tables 4.3 to 4.6, can result in errors in the transport parameters, which are employed in various models of a HEMT.

Chapter 5

CONCLUSION

Using the Poisson solver (FISH1D), the 1-D E_c profile obtained for various points along the channel of the HEMT operating in the linear region, clearly showed a variation in the quantum well width from the source to the drain. In this work, the scattering rates for polar optical phonons (POP), acoustic phonons (AP) via deformation potential and impurity scattering have been studied theoretically as a function of the incident energy of the electron and the position along the channel for a $Al_{0.37}Ga_{0.63}As/GaAs$ HEMT. A wide variation in scattering rates from the source to the drain for different scattering mechanisms was observed due to varying degrees of quantum confinement. Some intersubband mechanisms which are absent at the source, are present at the drain due to the variation in Eigen energy value separations. This results in huge differences in the scattering rates between the source and the drain. These wide variations in the scattering rates will introduce errors in the transport properties which, in turn, will influence the I-V characteristics significantly. These effects will become more pronounced in n-ON HEMTs with a large V_{GC} range with the device operating in the ohmic region or for devices operating in the saturation regime.

This study, thus shows that the variation of quantum confinement along the channel from the source to the drain cannot be assumed to be the same. It is observed that the transport properties of the HEMT structure under consideration, are dependent on the position and not just the electric field along the channel. It is also noted that the POP mechanism exhibits a maximum variation of 114% (the largest maximum variation occurring for the 5 $\longrightarrow$ 2 emission mechanism) in the rates for both intrasubband and intersubband scattering mechanisms from the source to the drain due to varying degrees of quantum confinement. The AP mechanism shows a maximum variation of 109% (for the 4 $\longrightarrow$ 4 mechanism) and the scattering rate due to impurity scattering presents a maximum variation of 133% (for the 5 $\longrightarrow$ 5 mechanism).

One of the shortcomings of this work is that our operating point was chosen in the linear region. Several other factors such as real space transfer at the drain end and hot electron effects have been neglected. In order to choose an operating point in the saturation region, one will need to start out with an accurate conduction band edge profile for the device under consideration . This can be accomplished by a self-consistent solution of Schrödinger's and Poisson's equations. But even if the operating point of the device were chosen to be in the saturation region, one would expect variations in the scattering rates from the source to the drain and the purpose of this work is to bring to light, this very fact.

Bibliography

[1] ARTAKI M. and HESS A., Transient and steady-state electron transport in $GaAs/Al_xGa_{1-x}As$ heterojunctions at low temperatures: the effects of electron-electron interactions, Phys. Rev. B., vol. 37, 2933, (1988).

[2] CHIU L.C. , MARGALIT S. and YARIV A., Jpn. J. Appl. Phys., vol. 22, L82, (1983).

[3] CHOW P.C., A computer solution to Schrodinger's equation, Amer. J. Phys., vol. 40, 730, 1972, (1986).

[4] DELAGEBEAUDEAUF D. and LINH N. T., Metal-(n) $AlGaAs - GaAs$ two-dimensional electron gas FET, IEEE Trans. Elec. Dev., vol. ED-29, (1982).

[5] FERRY, D. K., Scattering by polar-optical phonons in a quasi-two-dimensional semiconductor, Surf. Sci., vol. 75, 85, (1978).

[6] FERRY, D. K., Semiconductors.

[7] FISH1D User's Manual, Purdue University, Indiana, (1992).

[8] FRITZSCHE, D. Heterostructures in MODFETs, Solid State Electronics, vol. 30, No. 11, pp. 1183-1195, (1987)

[9] GOLIO, M., Microwave MESFETs and HEMTs, Artech House, (1991).

[10] HESS K., Impurity and phonon scattering in layered structures, Appl. Phys. Lett., vol. 35, 484. (1979).

[11] LADBROOKE, P., MMIC Design: $GaAs$ FETs and HEMTs.

[12] LEBURTON J. P., Size effects on polar optical phonon scattering of 1-D and 2-D electron synthetic semiconductors, J. Appl. Phys., vol. 56, 2850, (1984).

[13] LEE K., SHUR M., DRUMMOND T. J. and MORKOC' H., J. Appl. Phys., vol. 54, 6432, (1983).

[14] LUNDSTROM, M., Fundamentals of carrier transport, Addison-Wesley, (1990).

[15] NG. S., KHOIE R. and VENKAT R., A two-dimensional self-consistent numerical model for high electron mobility transistor, IEEE Trans. Elec. Dev., vol. 38, 852 (1991).

[16] PARK D. et al, Ensemble Monte Carlo simulation of a 0.35 μ m pseudomorphic HEMT, IEEE Electron Devices Lett., vol. EDL-6, (1985).

[17] PRICE P., Electron transport in polar heterolayers, Surf. Sci., vol. 113, (1982).

[18] PRICE P. J., Two-dimensional electron transport in semiconductor layers: I. Phonon Scattering, Ann. Phys., vol. 133, 617, (1981).

[19] RIDLEY, B K., The electron-phonon interaction in quasi-two-dimensional semiconductor quantum-well structures, Journal of Physics C, (1982).

[20] SHEY A. J. and KU W. H., On the charge control of the two-dimensional electron gas for analytic modeling of HEMTs, IEEE Elec. Dev. Lett., vol. 9, 624, (1988).

[21] STERN and DAS SHARMA, Elecron energy levels in $GaAs/Ga_{1-x}Al_xAs$ heterojunctions, Phys. Rev. B, vol. 30, (1987).

[22] STERN and HOWARD, Properties of semiconductor surface inversion layers in the electric quantum limit, Phys. Rev. 163, 816, (1967).

[23] TOMIZAWA M., and HASHIZUME, Ensemble Monte Carlo simulation of an $AlGaAs/GaAs$ heterostructure MIS-Like FET, IEEE Trans. Electron Dev., vol. 35, (1988).

[24] TOMIZAWA M., YOSHII A., YOKOYAMA K., Modeling for an $AlGaAs/GaAs$ heterostructure device using Monte Carlo simulation, IEEE Electron Devices Lett., vol. EDL-6, pp 332-334, 33, (1985).

[25] WANG and HESS, Calculations of the electron velocity distribution in HEMTs using an ensemble Monte Carlo method, J. Appl. Phys., vol. 57, (1985).

[26] WALUKIEWICZ et al, Electron mobility in modulation doped heterostructure, Phys. Rev. B, vol. 30, (1984).

[27] WIDIGER D. J. et al, Two-dimensional transient simulation of an idealized HEMT, IEEE Trans. Electron Dev., vol. ED-32, (1985).

[28] YOKOYAMA K. and HESS., Monte carlo study of electronic transport in single-well heterostructures, Physical Review B, vol. 33, 5595, (1986).